Transport properties of $YBa_2Cu_3O_7/PrBa_2Cu_3O_7$-superlattices

Dissertation
zur Erlangung des Grades
Doktor der Naturwissenschaften (Dr. rer. nat.)
am Fachbereich Physik
der Johannes Gutenberg-Universität Mainz

von
Ayman Mohamed Moussa El Tahan
geboren in Gharbia, Ägypten

Mainz, 2010

CONTENTS

LIST OF FIGURES

LIST OF TABLES

INTRODUCTION

The common structural feature in high Tc superconductors (HTCS) is the presence of Copper Oxide planes (separated by Yttrium atoms in the $YBa_2Cu_3O_7$ (YBCO) structure). These planes form the *ab*-planes of the orthorhombic crystal structure and are responsible for a highly anisotropic structure, which also shows up in the corresponding superconducting properties. So the crystalline anisotropy strongly influences the static and the dynamic behavior of the vortex system. With respect to the superconducting cooper pairs, the coherence length for YBCO in the *ab*-plane (ξ_{ab}) is about 1-2 nm, while in the *c*-axis direction (ξ_c) is significantly shorter (about 0.03 nm). This situation is useful for electronics applications of HTCS, but, on the other hand, raises significant challenges in the device fabrication and integration. One immediate idea for the device fabrication is to stack in the *c*-axis direction alternating layers of the superconductor and of an insulator to produce artificial tunneling SIS (superconductor-insulating-superconductor) Josephson junctions. Growth of top quality individual *c*-axis HTCS thin films was performed by many groups [1] and the next step of SIS *c*-axis heterostructures growth may look straightforward. Despite this positive fact, success rate of demonstrating Josephson junctions on SIS *c*-axis heterostructures is rather low [2]. Among the reasons is that the very short ξ_c imposes serious requirements on the flatness of the surfaces, on inter diffusion problems and, not least, on the thickness of the insulating layer that should be of the same order of magnitude as the short ξ_c. One sound solution is to build devices using a-axis HTCS thin films and heterostructures taking advantage of the longer ξ_{ab}.
Therefore one part of the work presented here dealt with the investigation of *c*-axis vs. *a*-axis growth (the epitaxial growth parallel to the Copper Oxide planes)

in $YBa_2Cu_3O_7$ thin films on (001) $SrTiO_3$ substrates. A wide range of growth temperature was investigated starting from 825^0C to 610^0C, and one can see this evolution from c-axis to a-axis in chapter six. There unique orientations for c-axis or a-axis grown films are demonstrated with a high crystalline quality showing up in very sharp rocking curves of FWHM $< 0.11^0$ at (005) and (200) reflections, respectively.

Additional flexibility in tuning the anisotropy can be gained using superlattice structures. Superlattices are a coherent structure of alternating layers of two or more materials. It is possible to produce high-quality superlattices of HTC superconductors using high pressure sputter deposition in pure oxygen atmosphere (3mbar). In this work, I used (001) $SrTiO_3$ (which has a cubic structure with lattice parameters ≈ 3.905 Å) as a substrate, and the superlattices were made from two different materials $YBa_2Cu_3O_7$ (where $a \approx 3.887$ Å , $b \approx 3.823$ Å and $c \approx 11.682$ Å) and $PrBa_2Cu_3O_7$ with similar lattice structure and matching lattice parameters.

For these superlattices there are two possibilities of epitaxial growth as shown in figure 1.

- Epitaxial growth in the direction of the c-axis such that one unit cell of $SrTiO_3$ fits with ab plane of $YBa_2Cu_3O_7$ or $PrBa_2Cu_3O_7$.
- Epitaxial growth in the direction of a-axis where three unit cell lengths of $SrTiO_3$ fit with the c-axis of $YBa_2Cu_3O_7$ or $PrBa_2Cu_3O_7$ in the substrate plane.

The tuning of the anisotropy with the superlattice structure was investigated by measurement of transport properties. A magnetic field penetrates these type II superconductors in form of magnetic vortices. At high temperatures and/or at high currents the vortices can move leading to dissipation. The activation energies of the vortex system in a series of c-axis oriented $(YBCO)_{nY}/(PBCO)_{nP}$ (Y_{nY}/P_{nP}) superlattices will be investigated in chapter three, where nY and nP denote the thickness of the respective layers measured in unit cells. For one series we kept the PBCO thickness to four unit cells nP = 4 which corresponds to a thickness of $4 \times 1.17 = 4.7$ nm, while we varied the thickness of the YBCO layers (Y_{nY}/P_4, with nY = 1, 2, 4, 6, 8, 11, 20, 40, and 80). For the other series we used a fixed YBCO thickness of four unit cells and varied the non superconducting layers (Y_4/P_{nP} with nP = 1, 2, 4, 6, 8, and 11). The number of repetitions of the

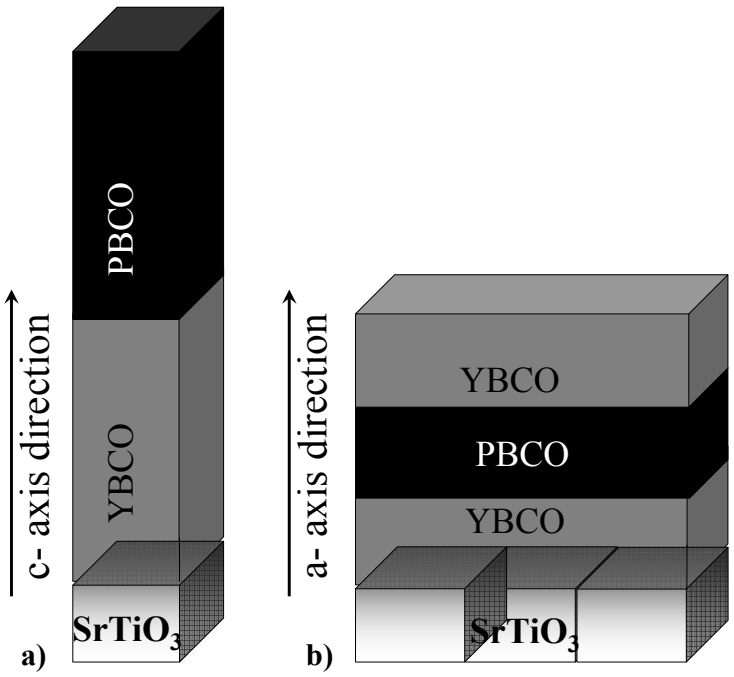

Figure 1: Epitaxial growth of $YBa_2Cu_3O_7/PrBa_2Cu_3O_7$-superlattices on $SrTiO_3$ in c-axis or a-axis orientation as shown in part a) and b), respectively.

Y/P bilayers was chosen such that the total film thickness was constant (around 200 nm).
The vortex-creep activation energy U_0 was determined by analyzing the in-plane resistive transition of 200 μm wide bridges with the external magnetic field B oriented along the c-axis. It was found that U_0 is proportional to the thickness of the YBCO layers, and does only weakly depend on the PBCO layer thickness, when the latter exceeds two unit cells. We observed a change in the variation of U_0 with the current I in the specimen: U_0 exhibits a plateau in the low-I region, then decreases significantly with increasing I. This behaviour is explained in terms of a crossover plastic vortex creep - elastic (collective) creep induced by the transport current.

In chapter four the relaxation of the irreversible magnetization in a series of 200 nm thick $(YBCO)_{nY}/(PBCO)_{nP}$ (Y_{nY}/P_{np}) superlattices is discussed, where the thickness nP of the nonsuperconducting PrBCO layer (measured in unit cells) was kept to nP $= 4$ (sufficient to decouple the superconducting YBCO

layers), whereas the thickness nY of the YBCO layer was varied between 2 and 20 unit cells. The analysis of standard zero-field-cooling (zfc) dc magnetization relaxation data obtained in the low temperature T region with the applied magnetic field H oriented along the c-axis reveals the occurrence of a crossover elastic (collective) vortex creep at low T and plastic vortex creep at high T, generated by the T dependent macroscopic currents induced in the sample during measurements, similar to that reported for YBCO films. For thin superlattices (nY < 20) the creep crossover temperature $T_{cr} \propto$ n, and T_{cr} decreases linearly with increasing $ln(H)$ for a fixed nY. This crossover represents an alternative to the elastic vortex glass behaviour reported for superlattices, as well as to "quantum vortex creep" at unexpectedly high T inferred for thin films. We also discuss the absence of an increase of the magnetically determined critical current density with decreasing YBCO thickness in thin superlattices, which apparently contradicts the collective pinning theories.

Tunneling characteristics into High T_c Superconductors (HTCS) are strongly affected by the anisotropy and hence should differ significantly when measured along the directions of poor conductivity (the c-axis) or of good conductivity (the ab planes) [3]. One aim of this work was to show how a change in superlattice modulation effects the transport properties in the c-axis direction, and to show whether a coherent Josephson coupling between $YBa_2Cu_3O_7$ layers separated by $PrBa_2Cu_3O_7$ sheets appears. Sputtering is a suitable technique for the preparation of HTS films and heterostructures, because of its simplicity, scalability and the possibility to grow high quality films with this method. However, the main problem of the sputtered c-axis oriented YBCO films is usually roughness. These rough surfaces mainly originate from a mixed growth of a-axis crystallites in the c-axis matrix and compositional deviations due to re-evaporations of ad-atoms [4]. Nevertheless in chapter five the investigation of c-axis transport on superlattices prepared by two different methods will be discussed. In the first one normal thickness superlattices (200 nm) with four different mesa structures (50×50), (40×40), (30×30), and(16×16) μm^2 that have been patterned photolithographically will be investigated. The second method utilizes a thick superlattice ($1\mu m$) and a different patterning strategy. After a photolithography step a focused ion beam (FIB) is used to achieve dimensions down to (1×1) μm^2. In search for an indication of Josephson coupling the resistivity perpendicular to the patterned heterostructures is analysed.

Before I discuss in my Ph.D. thesis the above experiments I will introduce

first in chapter one shortly some theoretical background and models for flux-movement in superconductors, which forms the basis for the discussion of the results achieved in later chapters.

In more detail, I introduce in chapter two the preparation and characterization of high temperature superconducting $YBa_2Cu_3O_7/PrBa_2Cu_3O_7$ superlattices and $YBa_2Cu_3O_7$ films. Though, all thin film samples are prepared by high pressure dc-sputtering in an UHV chamber, depending on the different transport measurements planned for the respective samples, the detailed assembly of the thin film structures and sputtering conditions varied.

CHAPTER 1

THEORETICAL BACKGROUND

Until now, no consistent theory can explain the behavior and all the properties that are possessed by high-Tc superconductors. However, this chapter aims to give some insight about theories and models that can illustrate essential features of these materials, which are important for the evaluation of the work presented in this thesis.

1.1 Ginzburg Landau (GL) theory

The theory of Ginzburg and Landau [5] is the first theory of superconductivity taking local variations of the order parameter into account, while London theory assumes the order parameter to be constant in the superconductor. GL theory is a phenomenological theory of superconductivity though it can be derived as a limiting case of the BCS theory. The GL model and the London model are independent of the underlying mechanism for superconductivity. However, it must be stated that GL theory is strictly valid only near the normal-to-superconducting phase boundary, and that it is not generally applicable at low temperatures. GL introduced a complex pseudo wave function ψ as an order parameter within Landau's general theory of second-order phase transitions[1]. This ψ describes the superconducting electrons, and the local density of superconducting electrons was given as $n_s = |\psi(x)|^2$. They were able to treat two features, which were beyond

[1]Second order phase transition is a transition at which the state of the system is changing continuously, but its symmetry changes suddenly.

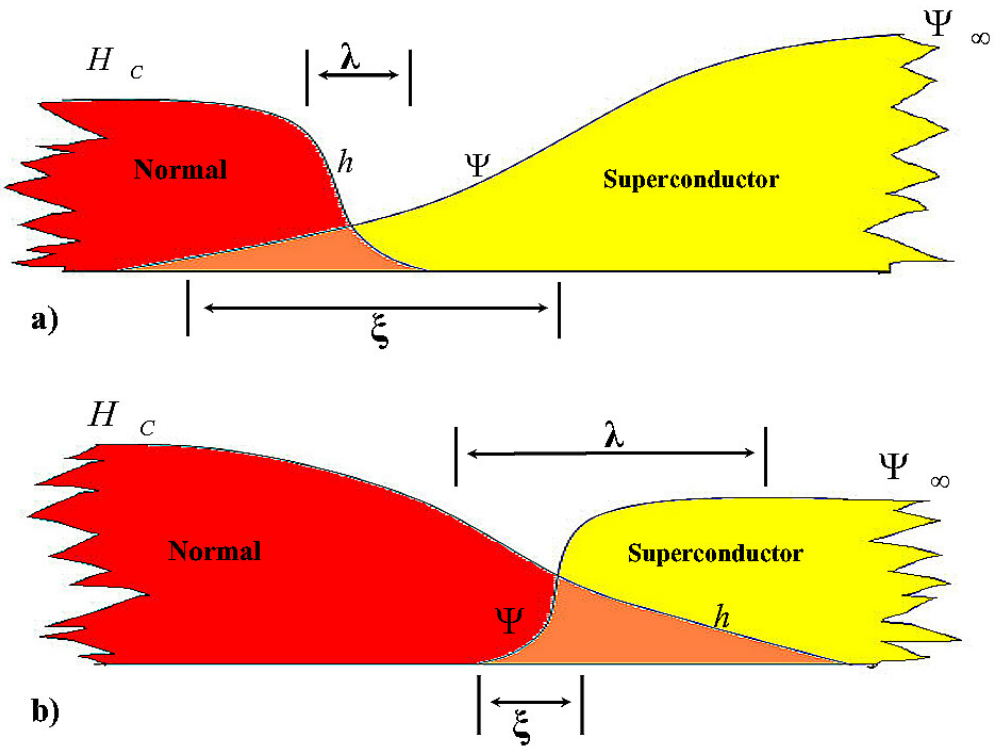

Figure 1.1: Schematic diagram showing the variance of h and ψ(x) with the distance from a normal-superconductor interface. (a) Type I superconductor. (b) Type II superconductor.

the scope of London theory, namely: (i) non-linear effects of fields strong enough to change n_s (or $|\psi|^2$) and (ii) the spatial variation of n_s. Besides a temperature-dependent penetration depth (λ), they also obtained a temperature-dependent coherence length (ξ). The latter characterizes the distance over which ψ(x) can vary without a substantial energy increase. The ratio of the two characteristic lengths, ξ and λ, defines the GL parameter, $\kappa = \lambda/\xi$. Abrikosov showed that the exact breakpoint between Type I and Type II superconductors (see figure 1.1) was at $\kappa = 1/\sqrt{2}$ [6].

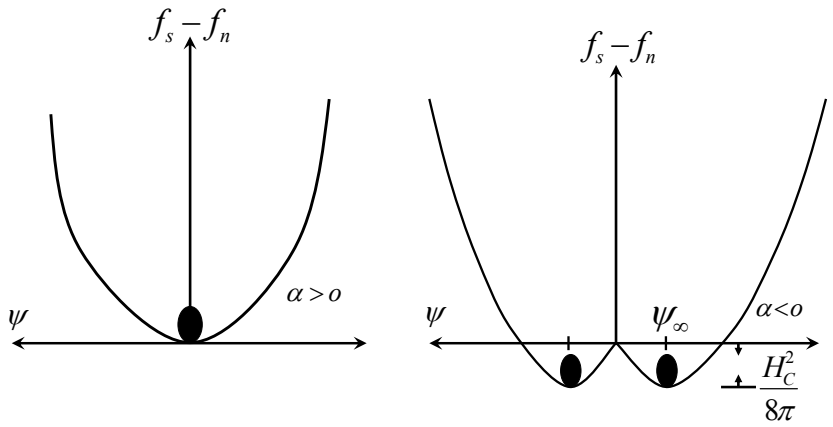

Figure 1.2: $|\psi|$ dependence of the GL free energy without gradients or fields when a) $T > T_c$ (left) and b) $T < T_c$ (right).

1.1.1 GL free energy

GL theory without applied magnetic field

Ginzburg and Landau assumed that the free energy difference per unit volume between the superconduting and the normal state at zero magnetic field is taken as a function of ψ near T_c, where ψ is small.

$$f_s(0) = f_n(0) + \alpha \left|\psi\right|^2 + \frac{\beta}{2} \left|\psi\right|^4 \tag{1.1}$$

α and β are temperature-dependent coefficients, such that near T_C, α is positive for $T > T_C$ as shown in Fig. 1.2a, and negative for $T < T_C$ (Fig. 1.2b). Since $n_s = |\psi|^2$ the equilibrium of the order parameter is obtained at $\frac{\partial(\Delta f)}{\partial n_s} = 0$, then the solution of Eq. 1.1 is

$$|\psi|^2 = -\frac{\alpha}{\beta} = |\psi_\infty|^2 \tag{1.2}$$

substituting this result in Eq. 1.1 we find that

$$f_s(0) - f_n(0) = -\frac{H_c^2}{8\pi} = -\frac{\alpha^2}{2\beta} \tag{1.3}$$

In Eq. 1.2, ψ_∞ is defined as the ψ value in the interior of the sample, where no gradients of the order parameter exist. Now the relation between the free energy in Fig. 1.2 and Eq. 1.1 becomes more evident. The sign of α must change at T_c for the second order phase transition and the parameter β must be constant $>$ 0 in this case.

The ratio T/T_c defines the reduced temperature (t). The temperature dependencies for α and β are consistent with $H_c(T) \propto (1-t)$ close to T_c. Note that just below T_c, these temperature dependencies also yield

$$|\psi|^2 \propto n_s \propto (1-t)$$

Over the entire temperature range from zero to T_c one can approximate $H_c(T) \propto (1-t^2)$ and $n_s \propto (1-t^4)$. Close to T_c we find that $H_c(T) \propto (1-t)$ and $n_s \propto (1-t)$ is a good approximation.

GL theory with aplied magnetic field

In the presence of magnetic fields and spatial gradients, the free energy in the superconducting state is increased. In general the work done by the magnetic field on the sample is

$$-\int_0^V dV \int_0^H \vec{M} \cdot d\vec{H} \tag{1.4}$$

Where, M and V are Magnetization and volume of the sample respectively. If the sample state has a homogenous superconductor (Meissner phase), the magnetization will have a negative sign ($M = -H/4\pi$), while M in the normal state is basically zero. This means that in the presence of a magnetic field, the Gibbs free energy per unit volume will increase in the superconducting state, and this increasing value is related to the magnetic field H.

$$G_s(H) = G_s(O) + \frac{H^2}{8\pi} \tag{1.5}$$

In the critical state $G_s(H_c) = G_n(H_c)$, and in the normal state it is approximately field independent $G_n(H) = G_n(0)$.

By using a Legendre transformation, one can write the Gibbs free energy per unit volume in terms of the Helmholtz free energy per unit volume. Therefore the free energy density may be taken as

$$f_s(0) = f_n(0) + \alpha |\psi|^2 + \frac{\beta}{2} |\psi|^4 + \frac{1}{2m^*} \left| \left(\frac{\hbar}{i} \nabla - \frac{e^*}{c} A \right) \psi \right|^2 + \frac{H^2}{8\pi} \tag{1.6}$$

The gradient term

$$\frac{1}{2m^*} \left| \left(\frac{\hbar}{i} \nabla - \frac{e^*}{c} A \right) \psi \right|^2 \tag{1.7}$$

is additionally introduced by Ginzburg and Landau. They assume that the order parameter ψ in the presence of a magnetic field is not completely rigid and there is an additional kinetic energy term associated with variations in ψ. This kinetic energy term is written using the fact $E = \frac{P^2}{2m^*}$ and with $P = \left(\frac{\hbar}{i}\nabla - \frac{e^*}{c}A\right)$, the momentum in the presence of magnetic field. Here m* = 2m, e* = 2e and $n_s^* = \frac{1}{2} n_s$ is the superconducting electron mass, charge, and density, respectively, and A is the vector potential.

In equation 1.6 the order parameter ψ is small, if the free energy density is taken for temperatures near T_c. This order parameter can be defined in terms of phase factor also as follows:

$$\psi = |\psi| \, e^{i\phi}$$

Further consider the terms in the GL free energy involving gradients and fields, therefore the kinetic energy term Eq. 1.7 can be written as following

$$\frac{1}{2m^*} \left[\left(\hbar^2 \nabla |\psi| \right)^2 + \left(\hbar \nabla \phi - \frac{e^*}{c} A \right)^2 |\psi|^2 \right] \tag{1.8}$$

In this equation the first term implies that gradients of the magnitude of the order parameter exist, which are e.g. not equal to zero at a domain wall. The second term is the kinetic energy like term, which is related to the supercurrent. If we apply the London gauge for ϕ, which is constant ($\nabla\phi = 0$) then the second term in Eq. 1.8 will be $\left(\frac{e^{*2}A^2}{2m^*c^2}\right) |\psi|^2$. If one applies London approach with the vector potential A, one can determine the general penetration depth λ_{eff}^2

$$\lambda_{eff}^2 = \frac{m^* c^2}{\left(4\pi e^{*2} |\psi|^2\right)} \tag{1.9}$$

The usual London penetration depth could be obtained by using $n_s = |\psi|^2$, where n_s is the ordinary (nonpaired) electron density. If the starred quantities (m^*, e^* and n_s^*) are replaced by the normal quantities (m, e and n_s), the value of λ_{eff}^2 would not change, $\lambda_{eff}(nonpaired) = \lambda_{eff}(paired)$. By substitution the starred quantities and Eq. 1.9 in Eq. 1.2

$$|\psi_\infty|^2 = \frac{n_s}{2} = n_s^* = \frac{m^* c^2}{4\pi e^{*2} \lambda_{eff}^2} = \frac{mc^2}{8\pi e^2 \lambda_{eff}^2} \tag{1.10}$$

$$\alpha(T) = -\frac{e^{*2}}{m^* c^2} H_c^2(T) \lambda_{eff}^2(T) = -\frac{2e^2}{mc^2} H_c^2(T) \lambda_{eff}^2(T) \tag{1.11}$$

$$\beta(T) = \frac{4\pi e^{*4}}{m^{*2} c^2} H_c^2(T) \lambda_{eff}^4(T) = \frac{16\pi e^4}{m^2 c^2} H_c^2(T) \lambda_{eff}^4(T) \tag{1.12}$$

By using the reduced temperature $t \equiv T/T_c$, one can deduce the temperature dependencies $\alpha \propto (t-1)$ and $\beta \approx const.$

1.1.2 GL differential equations

When n_s varies slowly in space, one can calculate the variation of the energy with the respect to the order parameter. Taking into account that $|\psi|^2 = \psi\psi^*$, one has three different variables ($\psi, \psi^*$and A).

When the total free energy per unit volume of the superconducting state in the presence of a magnetic field is minimized with respect to ψ^* and the others are constant, this leads to the *first Ginzburg-Landau equation.*

$$\alpha\psi + \beta\psi |\psi|^2 + \frac{1}{4m^*} \left(-i\hbar\nabla - \frac{e^*}{c} A \right) \psi = 0 \tag{1.13}$$

Minimizing with respect to A leads to the *second Ginzburg-Landau equation.*

$$j_s = -\frac{i\hbar e^*}{2m^*} (\psi^* \nabla\psi - \psi \nabla\psi^*) - \frac{e^{*2}}{m^* c} \psi^* \psi A \tag{1.14}$$

Which is considered as the standard expression for the quantum-mechanical current.

1.1.3 GL coherence length

In the absence of fields in the GL differential equation, one can set ($A = 0$). If the coefficients are real, ψ may be taken to be real. Let us introduce the normalized wave function and in one dimension, where $G \equiv \frac{\psi}{\psi_\infty}$, with $\psi_\infty^2 = -\frac{\alpha}{\beta} = \frac{1}{2}n_s$, then the Eq. 1.13 will become

$$\frac{\hbar^2}{2m^*\left|\alpha\right|}\frac{d^2G}{dx^2} + G - G^3 = 0. \quad \text{or} \quad \xi^2\left(\frac{d^2G}{dx^2}\right) + G - G^3 = 0. \tag{1.15}$$

Dimensionally ξ is a characteristic length and is defined below T_c as

$$\xi^2(T) \equiv \frac{\hbar^2}{2m^*\left|\alpha\right|} \tag{1.16}$$

This length describes the variation of ψ due to a small disturbance. To understand this, let $G = g + 1$ and $g << 1$ then Eq. 1.15 becomes

$$\xi^2\left(\frac{d^2g}{dx^2}\right) + (1+g) - (1 + 3g + ...) = 0. \quad \text{or} \quad \left(\frac{d^2g}{dx^2}\right) = \left(\frac{2}{\xi^2}\right)g$$

then

$$g(x) \approx e^{\pm\sqrt{2}x/\xi(T)} \tag{1.17}$$

Therefore a small disturbance of ψ will decay to ψ_∞ with a characteristic length $\xi(T)$. By substitution of Eq. 1.11 in Eq. 1.16 one can get $\xi(T)$, where the fluxoid or flux quantum ϕ_0 equals $\frac{\hbar c}{2e}$.

$$\xi(T) = \frac{\phi_0}{(8)^{1/2}\pi H_c(T)\lambda_{eff}(T)} \tag{1.18}$$

BCS [7] theory implis that, the fluxoid ϕ_0 can be related to ξ_0, the zero temperature London penetration depth $\lambda_L(0)$, and the thermodynamic critical field $H_c(0)$, as $\phi_0 = (2/3)^{1/2}\pi^2\xi_0\lambda_L(0)H_c(0)$. Thus, very near T_c, in the pure limit, where the intrinsic coherence length $\xi_0 > l$ (the mean free path) or $\xi_0/\lambda_L >> 1$,

$$\xi(T)_{pure} = 0.74\xi_0/\left(1-t\right)^{1/2}. \tag{1.19}$$

Increasing alloying causes increased electron-impurity scattering, leading to the dirty limit $l << \xi_0$,

$$\xi(T)_{dirty} = 0.86\left(\xi_0 l\right)^{1/2}\left(1-t\right)^{1/2}. \tag{1.20}$$

where l is the mean free path, and GL parameter is given

$$\kappa = \frac{\lambda_{eff(T)}}{\xi(T)} = 8^{1/2}\pi H_c(T)\lambda_{eff}^2(T)/\phi_0. \tag{1.21}$$

1.2 Relation between B_{c1} and B_{c2}

The relation between the critical fields, B_{c1} and B_{c2}, and length scales in Type II superconductors can be estimated. When the applied field is just above B_{c1}, the field at the vortex core will be $\approx B_{c1}$, radially decreasing to zero over a length λ. Thus, the flux will $\pi\lambda^2 B_{c1}$ and equal to ϕ_0, or

$$B_{c1} = \phi_0/\pi\lambda^2 \tag{1.22}$$

However, if the applied field is just below B_{c2}, the vortices are packed as closely as possible and each has an effective area $2\pi\xi^2$ or

$$B_{c2} = \phi_0/2\pi\xi^2 \tag{1.23}$$

Such that B_{c1} and B_{c2} are related to the thermodynamic field B_c as

$$B_{c2} = \sqrt{2}\kappa B_c$$
$$B_{c1} = (B_c/\sqrt{2}\kappa)\ln\kappa$$

$$B_{c1}B_{c2} = B_c^2 \ln\kappa \tag{1.24}$$

where B_c is the geometric mean of B_{c1} and B_{c2}.

1.3 Flux lines

When an external magnetic field larger than B_{c1} is applied to a type II superconductor, it will penetrate in the form of quantized bundles of flux, known as flux or vortex lines. Every flux line (FL) has a constant value (quantum) of magnetic flux $\phi_0 = h/2e$. By an increase of the magnetic field the number of flux lines will increase.
The order parameter goes to zero in the centre of the flux line. Therefore the region around the central line looks like normal conducting cylinder with radius (ξ). This circular cross-section will change to an ellipsoidal one in case of anisotropic superconductors. Both circular or elliptic flux lines are characterized by two important facts;

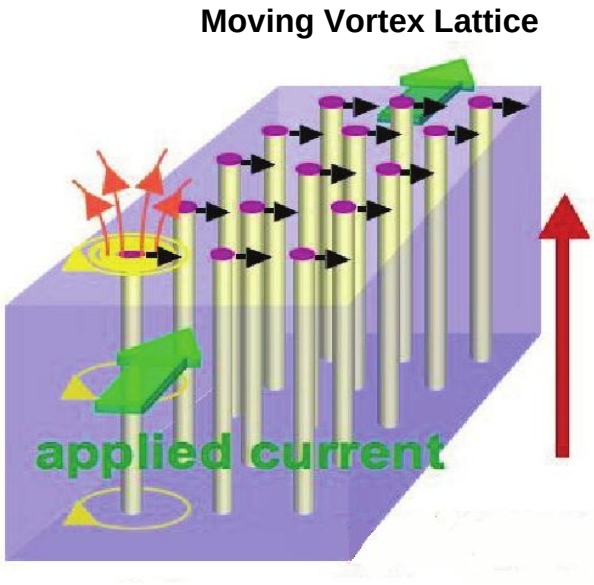

Figure 1.3: Origin of Lorentz force.

- Reduction of superconducting condensation energy due to reduction of order parameter.

- Increase of kinetic energy of the current carriers and local magnetic field energy due to shielding currents.

These two effects will appear as an energy per unit length associated with a flux line. Finally, this will lead to an increase in the energy of the system.

These vortices tend to arrange themselves in a triangular flux-line lattice (FLL), which is more or less distracted by inhomogeneities of the materials that pin the flux lines. In case of YBCO (high-Tc superconductors), the thermal fluctuations play an important role also for this arrangement.

1.3.1 Pinning mechanism

The importance of type-II superconductors with strong pinning comes from their ability to carry large transport currents in the presence of a magnetic field. Without pinning an applied current would lead to Lorentz forces on the flux lines and induce flux movement accompanied by energy dissipation.

1.3.2 Collective pinning theory

Natural pinning sites are usually not periodically distributed. If the flux line lattice (FLL) would be perfectly periodic and rigid, it could not be effectively pinned by any random collection of pinning sites [7]. Then an applied current would lead to Lorentz forces on the flux lines and induce flux movement accompanied by energy dissipation. However, the FLL is not a rigid system but the inter-vortex interaction allows elastic deformations of the FLL. Thus the vortex system can adapt to the spatial distribution of the pinning sites to minimize the sum of both pinning and elastic energies. Therefore, the equilibrium vortex configuration will be changed to a disordered arrangement. The main idea of Larkin and Ovchinnikov (LO) theory (1979) of collective pinning a description of the distorted FLL in terms of a correlation volumes that resembles the ordinary Abrikosov lattice, whereas with respect to the neighboring volumes pinning-motivated shear and tilt distortions will appear. Fig. 1.4 illustrates two important facts;

- The balance between pinning force F_P and Lorentz force F_L in the presence of magnetic field $\vec{B}$ and current density $\vec{J}$.

- The correlation volume $V_c = L_c R_c^2$ is indicated by its longitudinal and transverse dimensions L_c (along the direction of the magnetic field) and R_c , respectively.

Deformation of the FLL will lead to an increase of the elastic free energy per unit volume related to shear and tilt elastic modulus of the flux line lattice, C_{66} and C_{44}, respectively. On the other hand this energy also depends upon the strength of the distortion $S_s \backsim \xi/R_c$ and $S_t \backsim \xi/L_c$ and finally it is given by

$$\tfrac{1}{2}\left(C_{66}S_s^2 + C_{44}S_t^2\right).$$

In case of dominating elastic forces, bundles of rigid flux lines will form. The pinning motivated shear and tilt distortion will appear between neighbouring pinning volumes of lateral extension R_C and longitudinal extension L_C. From the net free-energy per unit volume (Eq. 1.25) induced by the distortion and pinning of this bundle, one can obtain the pinning energy.

$$\delta F = \frac{1}{2}C_{66}\left(\frac{\xi}{R_c}\right)^2 + \frac{1}{2}C_{44}\left(\frac{\xi}{L_c}\right)^2 - f_p\xi\frac{N^{1/2}}{V_c} \tag{1.25}$$

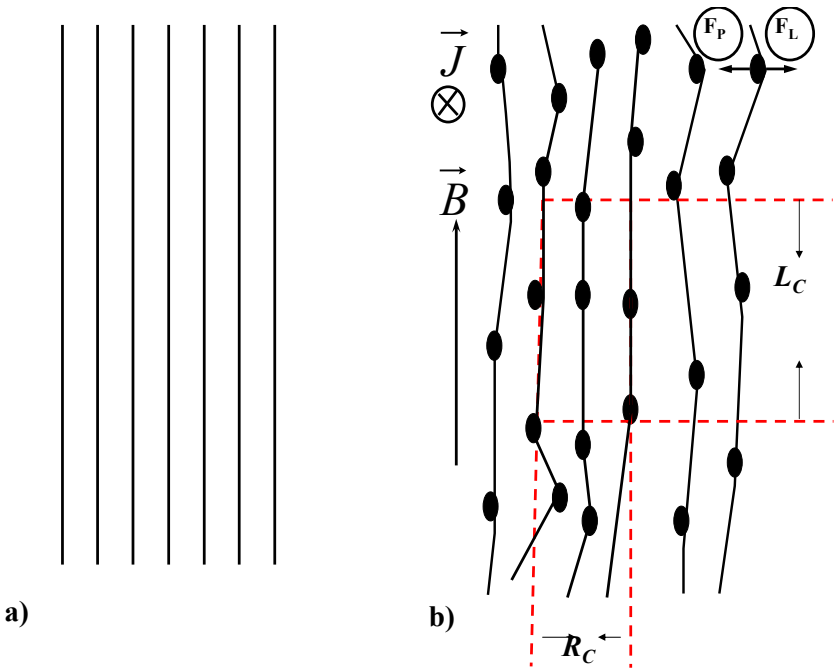

Figure 1.4: Coherence volume of the Larkin and Ovchinnikov theory of collective pinning. (a) the FLL is parallel to the magnetic field without pinning. (b) the FLL is distorted in presence of pinning centers. [7].

where the third term refers to the energy reduction in the potential energy gained by accommodating the pinning inside the correlation volume. So, it has a negative sign. Here ξ is the relavant interaction length, the elementary pinning force is f_p and finally N is the number of pinning sites in the the collective pinning volume, where $N = nV$ and n is the pinning center density. N enters the formula above only as $\sqrt{N}$ due to the fact that the elementary pinning forces can add up only in a random walk like manner. By minimizing Eq. 1.25 one can get the optimal correlation volume V_C.

$$L_c = \frac{2C_{44}C_{66}\xi^2}{nf_p^2}, \qquad R_c = \frac{(2C_{44}C_{66}^3)^{1/2}\xi^2}{nf_p^2}$$

$$V_c = \frac{4C_{44}^2\, C_{66}^4 \xi^6}{n^3 f_p^6} \tag{1.26}$$

To understand the last equation, in case of strong pinning sites and lower elastic moduli, one can confirm the expected decrease of V_c and then the FLL

will become more distorted. In this case a smaller correlation volume becomes energetically more favorable because this volume can better adjust to the distribution of pinning sites. It is clear now that a soft FLL leads to an increase of the depinning current density.
The interesting results is that by substituting Eq. 1.26 in Eq. 1.25 one can get the magnitude of the net pinning energy per unit collective pinning volume and the pinning force density which now is same magnitude as the Lorentz force ($F_P = F_L$)

$$J_C B = F_P = \frac{n^2 f_P^4}{2C_{44}C_{66}^2\xi^3} = F_L$$

$$J_C B = \left(\frac{n f_P^2}{V_C}\right)^{1/2} \tag{1.27}$$

Thus the collective pinning theory explains why pinning forces become more stronger when the FLL becomes very soft (like when it is close to B_{C2} in LTS or close to the irreversibility line in HTS).

Depending on the current the following cases exist

- In the case of small currents the pinning force opposes the Lorentz force and dissipation free current transport is possible.
- In the intermediate current range the behaviour is complex especially if pinning energies, elastic energies and thermal energy are comparable.
- For very strong currents the flux lines are depinned and the flux motion is damped by viscous forces predominantly, which is called the Stephen Bardeen flux-flow regime.
- In the flux creep regime the thermal activation induces flux movement. This can be in form of movement of individual flux-lines or in case of interacting vortices flux line bundles move.

As flux lines are line objects their longitudinal correlation along the magnetic field direction is generally much stronger than the transverse correlation, leading to different elastic moduli of the flux-line lattice for tilt and shear deformations.

In anisotropic systems like the layered high temperature superconductors (HTS) the crystalline anisotropy also strongly influences the vortex system. In YBCO the effective mass of charge carriers moving along c direction is approximately 50-100 times larger than that for the movement in the ab-plane

leading to an anisotropic FLL. In $Bi_2Sr_2CaCu_2O_{8+\delta}$ (Bi2212) the anisotropy is much stronger leading to an effectively two dimensional flux lattice consisting of 'pancake vortices' instead of flux lines [8]. For investigation of intermediate anisotropic cases YBCO/PBCO (Y/P) superlattices are a model system [9, 10, 11, 12, 13]. The thickness of the superconducting YBCO layers and non superconducting PBCO layers can be controlled on the unit cell scale. For thick decoupling PBCO layers and thin YBCO layers the correlation length of the flux line was shown to be constrained by the thickness of the superconducting layers [14, 13].

1.3.3 Collective pinning in two dimensions

When the film thickness becomes very thin or in case when the crystal contains decoupled layers and the magnetic field is applied perpendicular to the film, the longitudinal correlation length L_c refers to the film or layer thickness d. Therefore, the tilt elastic modulus of the flux line lattice C_{44} in Eq. 1.25 will be omitted and the correlation volume becomes $V_c = R_c^2 d$. In this case the critical current density and the pinning force are represented by

$$J_C B = F_P = \frac{n f_p^2}{C_{66} \xi d} = F_L \tag{1.28}$$

1.4 Models for flux-movement in superconductors

1.4.1 Flux-creep model

It is now well established that vortices (magnetic flux lines) are pinned by material inhomogeneities and will not move under the action of Lorentz force if the current density is less than the critical value J_c. At $T > 0$, some of the vortices are unpinned by thermal activation and an electric field is developed [15, 16], given by:

$$E(J) = 2\rho_c J_c \exp(-U/k_B T) \sinh(J U_c / J_c k_B T) \tag{1.29}$$

Where ρ_c is the resisitivity at $J = J_c$, U is the activation energy and U_c is the critical activation energy at J_c. This effect is observed very close to T_c in the form of flux-creep. In HTSC and in the presence of any kind of disorder which can be achieved by field cooled condition, vortices are prevented from reaching an equilibrium configuration. Consequently at finite temperature, any

finite current causes a thermal fluctuation which in turn leads to vortex motion. This results in relaxation of the disordered flux distribution and a giant flux creep is observed [17, 18]. One has for the flux creep case

$$\rho \propto \exp\left[\frac{(J/J_c - 1)}{k_B T} U\right] \tag{1.30}$$

At current densities J close to the critical value J_c; i.e. in the flux-creep regime, the activation energy $U(J)$ for activation of vortex bundles is small. $U(J)$ may be linearly expanded in $(J_c - J)$,

$$U(J) = \frac{U_c(J_c - J)}{J_c} \tag{1.31}$$

Where, the linear term J may be interpreted as the energy gain due to Lorentz force. In the presence of a Lorentz force $\vec{F}_L = \vec{J} \times \vec{B}$, the vortices move with an average velocity v_ϕ , which gives rise to an electric field [15]

$$\vec{E} = -\vec{v}_\phi \times \vec{B} \tag{1.32}$$

And hence to a finite resistivity $\rho_\perp = E/J$, where the subscript denotes the resistivity due to the vortex motion perpendicular to J [19]. For the unpinned vortex lattice $\rho_\perp$ is equal to the flux flow resistivity ρ_f which is given by [20]

$$\rho_f = \frac{\rho_n B}{B_{c2}}$$

Where ρ_n is the normal state resistivity and B_{c2} is the upper critical field. When pinning is important, the vortex velocity v_ϕ is proportional to the nucleation rate of vortex-bundles. This will lead to a thermally activated jumps in the direction of Lorentz force [20, 21] and has the form:

$$v_\phi = l(J)\nu_0 \exp(-U(J)/k_B T) \tag{1.33}$$

Where $l(J)$ is the typical jump length and ν_0 is the "attempt" frequency [22, 23]. The attempt frequency is the frequency at which vortex bundles try to escape from the pinning wells or centers. Small perturbations on distances smaller than $l(J)$ do not lead to a jump between metastable states. If such perturbations can be treated as elastic up to displacements smaller than some fraction A of the jump length $l(J)$, then ν_0 becomes [24]

$$\nu_0 = \frac{\rho_f J}{2\pi A B l(J)} \tag{1.34}$$

When a is the hopping distance and d is the average grain diameter for powdered samples. Then

$$E(J) = \frac{B\nu_0 a}{2\pi d} \exp\left(-\frac{U(J)}{k_B T}\right) \tag{1.35}$$

Substituting Eq. 1.31 into Eq. 1.35 gives a linear dependence of the logarithms of the induced electric field on the applied current J [25, 26].

1.4.2 Thermally Assisted Flux Flow (TAFF) model

The *TAFF* model first proposed by *Kes et al.* [27] is mainly concerned with the current regions at which $J < J_c$. It essentially deals with independent "particles", which jump between potential wells under the influence of thermal activation and small driving force. A current through the sample or magnetic flux gradient in the sample can generate this driving force. The main problems of the *TAFF* model are the definitions of the independent "particles", the potential well, the jump distance and the attempt frequency with which particles try to escape from their potential well [28]. For the "particle", *Kes et al.* [27] took the volume of the flux-line lattice (*FLL*) [29]. It plays the same role as flux bundles in the theory of Anderson [30]. Other parameters used in the model are defined in Fig. 1.5, where U_0 is the height of the potential well in the absence of a driving force, w is the jump distance and ΔW is the work done by external force when a flux bundle jumps from one minimum to another. The pinning energy and the maximum pinning force, F_P are related to V_{rP} [29], where, r_P is the range of the potential well and V is the vortex volume. Considering $r_P = w$, which is not a general result, without a driving force, the jump rate (frequency of vortices) between potential wells is isotropic.

$$| \vec{\nu} | = | \overleftarrow{\nu} | = \nu_0 \exp(-U/k_B T) \tag{1.36}$$

where $\overleftarrow{\nu}$ and $\vec{\nu}$ are the jump rates from right to left and from left to right, respectively. Applying the driving force results in a net movement of flux bundles in the direction of the applied force with a jump frequency [27]:

$$\nu = \vec{\nu} - \overleftarrow{\nu} = \nu_0 \exp(-U/k_B T) 2 \sinh(\Delta W/k_B T) \tag{1.37}$$

The general Eq. 1.29 introduced in section 1.4.1, can be applied for different models after introducing the proper modification. This equation can be based on the assumption of thermally activated jumps of vortex bundles. For ceramic

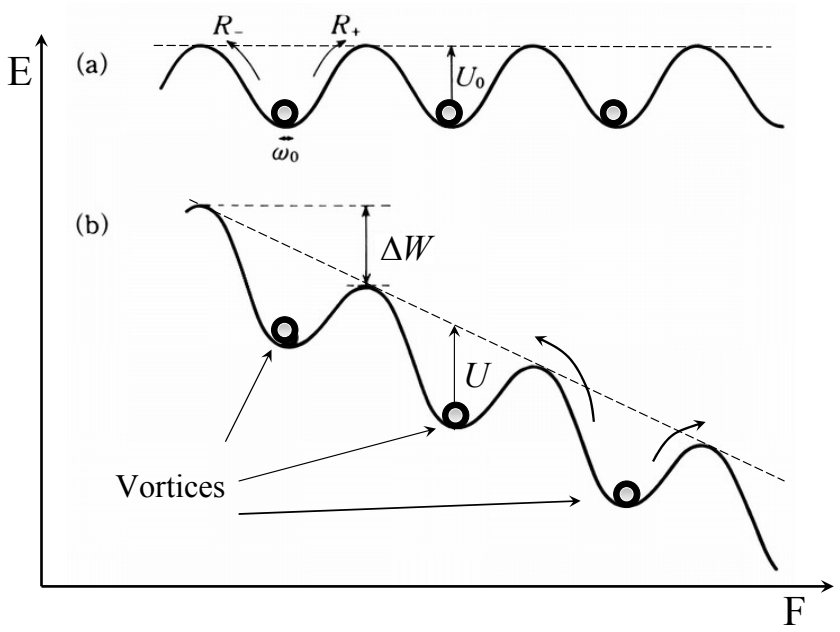

Figure 1.5: Schematic free energy as a function of force with a) no driving force and b) linear decrease of barrier by driving force [15].

materials, the current voltage dependence $(I - V)$ shows linear behavior over several orders of magnitude of J for the case of $J << J_c$ (flux flow region). Thus Eq. 1.29 may be considered as a phenomenological description of the *TAFF* model.

In the limiting case when $J << J_c$, the argument of $\sinh(JU/J_c k_B T)$ in Eq. 1.29 is very small such that $\sinh(JU/J_c k_B T)$ tends to $(JU/J_c k_B T)$. Hence Eq. 1.35 yields

$$E_{TAFF} = \frac{2\rho_c JU}{k_B T} \exp(-U/k_B T) \tag{1.38}$$

1.4.3 Bean model

Irreversibility line

In the cuprates in particular the critical current J_c is found to vanish at fields far below B_{c2}. The zero resistance state with finite J_c is found only below a new critical field B_{irr}. In the Fig. 1.6 the line $B_{irr}(T)$, below which the resistivity

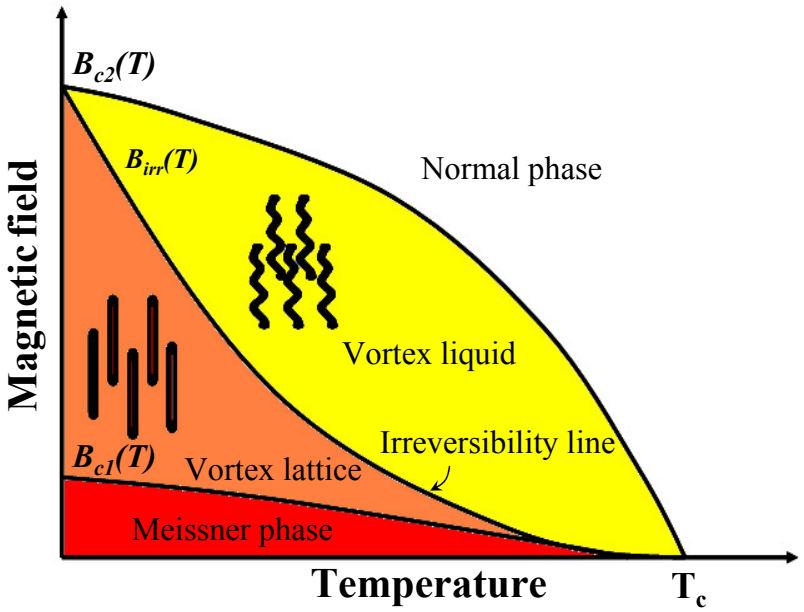

Figure 1.6: Magnetic field−temperature phase diagram of cuprate superconductors.

vanishes, is known as the irreversibility line. It is particularly noticeable in the cuprates because of the high transition temperature, low superconducting coherence length and high anisotropy.

The region below B_{c2} and above B_{irr} may be thought of as a vortex liquid. A description of this state requires a consideration of the effects of fluctuations in the GL model.

Bean model

The Bean Model offers a crude description of the hysteresis loop of a cylindrical type-II superconductor. The model assumes:

- $|\partial B/\partial x| = \mu_0|J_s|$ is equal to the critical value $\mu_0 J_c$ (taken to be a constant) and $B = B_E$ at the surface.

- When ramping up B_E the flux enters at the surface and when ramping down the flux leaves near the surface.

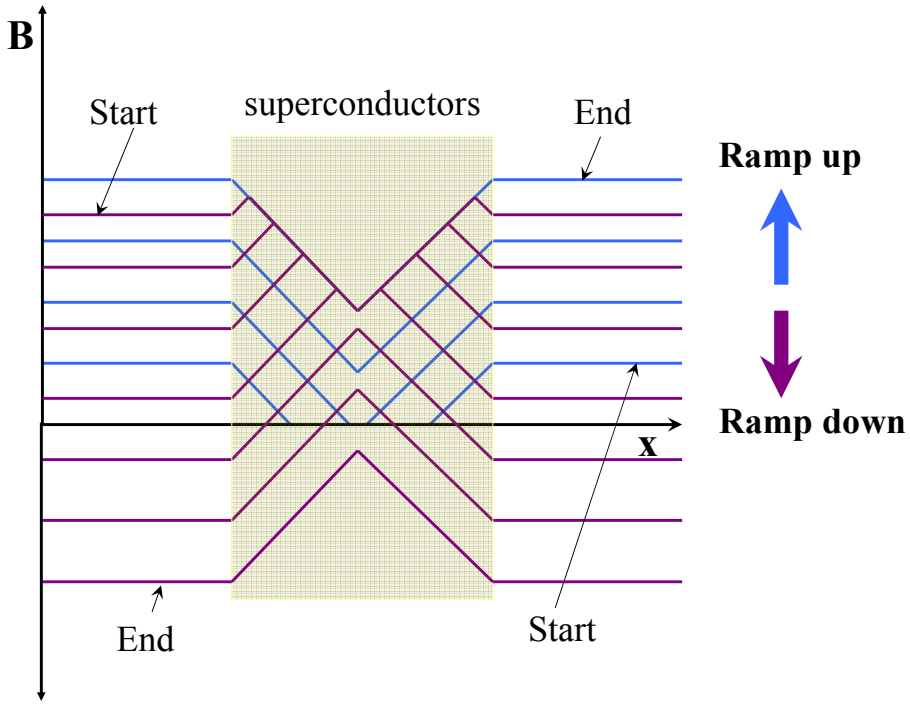

Figure 1.7: The Bean Model: Lines indicate the magnetic field strength as function of position. Blue lines result from an increase of the magnetic field. The flux starts to penetrate the sample from the outside with a field gradient to the center of the sample. The centre stays field free for low fields. By decreasing the field (ramp down with a violet colour) to zero again, flux will be trapped inside the sample.

There is a critical value of B_E where the field B penetrates to the centre of the slab. When a field $B > B_E$ is reduced to zero flux remains trapped at the center of the superconductor.

CHAPTER 2

PREPARATION AND CHARACTERIZATION

Introduction

The scope of this chapter is to introduce the preparation and characterization of high temperature superconducting $YBa_2Cu_3O_7/PrBa_2Cu_3O_7$ superlattices and $YBa_2Cu_3O_7$ films. All thin film samples are prepared by high pressure dc-sputtering in an UHV chamber. Depending on the different transport measurements planned for the respective samples, the detailed assembly of the thin film structures varied. Also the lithography methods used did depend on the planned transport measurements. Therefore I will make a general description of the common part "target and thin film preparation" followed by a classification into subsections which are related to specific patterning of the films, in order to investigate the transport properties perpendicular or parallel to the CuO_2 planes.

2.1 Preparation

2.1.1 Target

The $YBa_2Cu_3O_7$ target was prepared from a mixture of Y_2O_3, $BaCO_3$ and CuO (Alpha Aesar) powders with cation ratio Y:Ba:Cu = 1:2:3. The powder mixture

was calcinated in air at 890 ^{o}C for 24h. After grinding, the powder was pressed into a disk of 4cm in diameter and about 3mm in thickness and was sintered in air at 850 ^{o}C for 24h.
The $PrBa_2Cu_3O_7$ target was prepared by the same method.

2.1.2 UHV chamber

Sputter deposition is a technique for deposition of thin films. The sputtering method involves atomization of a solid target in a vacuum chamber by means of a plasma discharge of an inert gas between a grounded anode (where the substrate is placed) and a cathode with a negative potential (target), that is biased under a d.c. voltage between 0.2 kV and 2.0 kV.
In this work, epitaxial high quality HTSC superlattices and pure films were prepared in a multicathode sputtering UHV chamber as in Fig. 2.1 constructed and designed by G. Jakob [31]. Our targets $YBa_2Cu_3O_7$, $PrBa_2Cu_3O_7$ and Gold are started to work by applying a negative dc-voltage on it. The chamber offers the possibility to use up to four different targets. The substrate holder was controlled by a stepper motor and computer.

2.1.3 Substrate

$SrTiO_3$ (001) oriented single crystal substrate has a cubic perovskite oxide structure with lattice parameter $a = 3.905$ Å. The tetragonal unit cell for YBCO or PBCO has a lattice parameter $a = 3.89$ Å. Therefore, it is possible to grow films with the c-axis oriented perpendicular to the substrate. On the other hand, three unit cells of $SrTiO_3$ ($3a = 11.715$ Å) fit well with lattice parameter $c = 11.68$ Å of YBCO. In this case epitaxial growth with the a-axis perpendicular to the substrate is possible. The epitaxial growth of both c-axis and a-axis oriented films strongly depends upon substrate temperature. This point will be discussed in detail in chapter 6. The choice of an appropriate thermal treatment is essential for high quality and reproducible thin film growth.

2.1.4 Deposition with high oxygen pressure

During the sputtering process the oxygen pressure plays an important role to achieve high quality thin films. While sputtering is normally done at 10^{-2}-10^{-3}mbar gas pressure, for HTSC oxygen gas pressures around 1 mbar are often used.

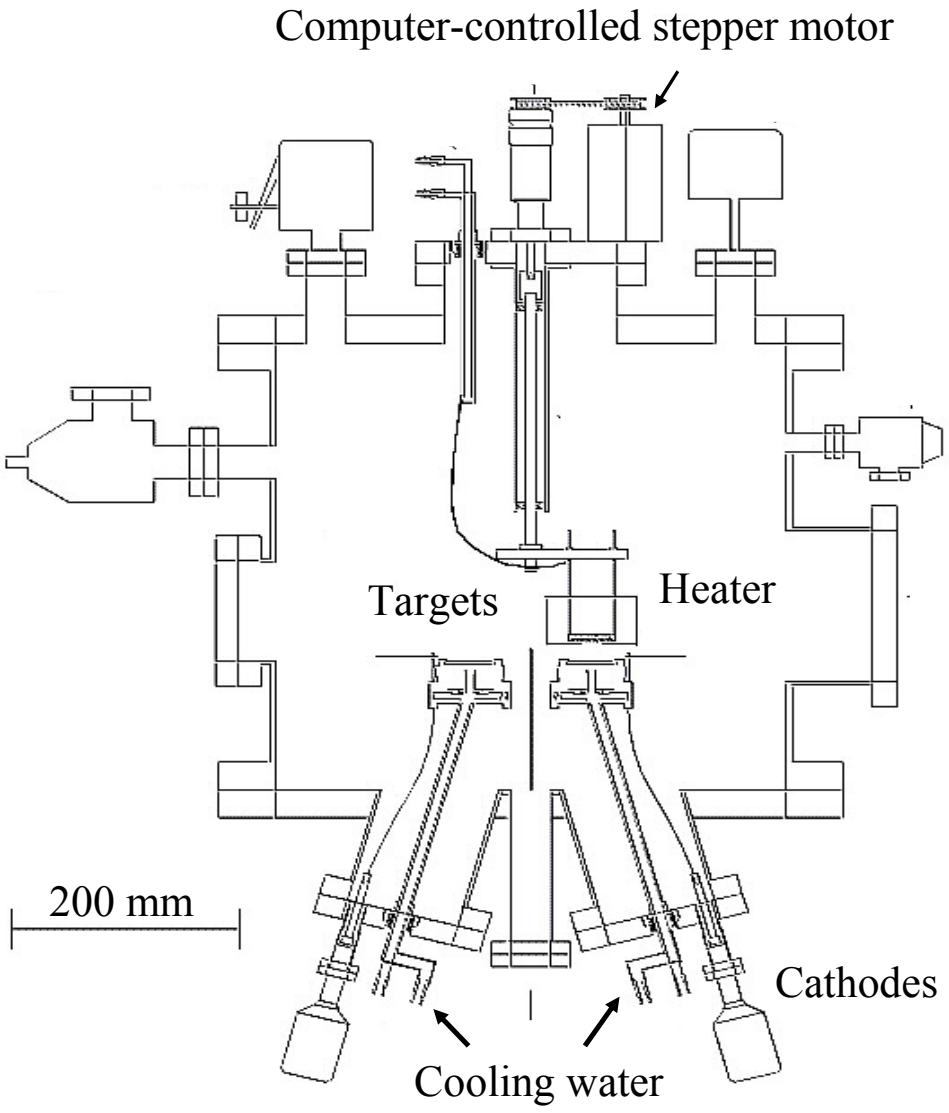

Figure 2.1: Cross section of the sputtering chamber used for film deposition.

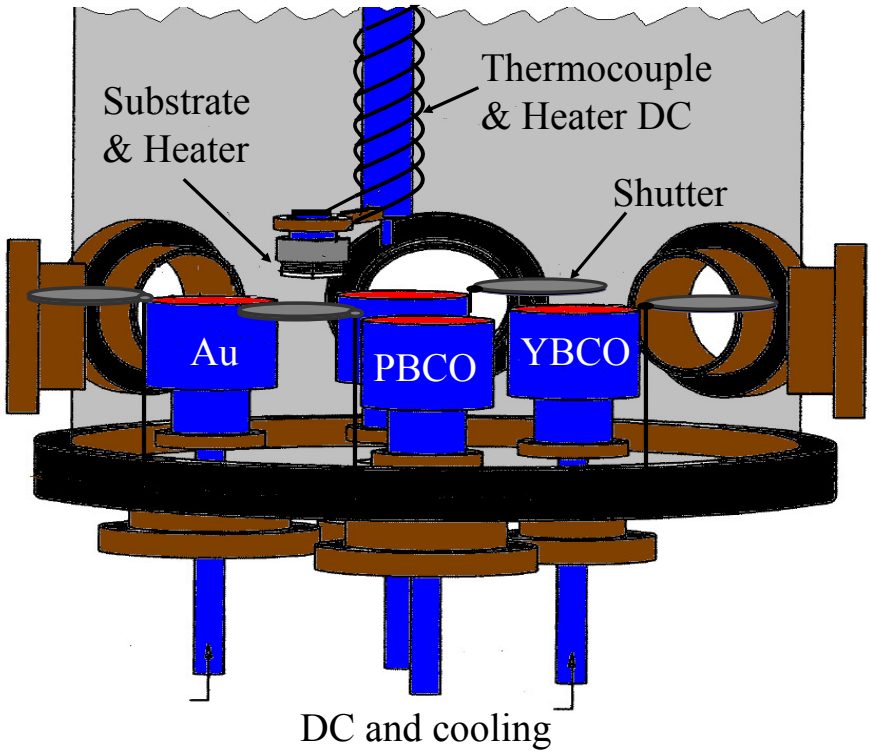

Figure 2.2: Sketch of the cathode and substrate holder geometry.

What is the main purpose for the use of a high oxygen gas pressure?
To answer this question let us see what happens at low pressure. Oxygen forms positive as well as negative ions in the sputtering plasma. The negative ions will accelerate away from the target surface, where the electric field is strongest. These oxygen atoms can gain high kinetic energy. At low pressure, the mean free path becomes large and there will be few collisions in the plasma. Therefore, high-energy oxygen ions can hit the substrate and sputter away already deposited film material (resputtering). Since resputtering is non-stoichiometric, this effect must be avoided. Therefore, in order to prevent fast oxygen ions resputtering the already deposited film, our process is performed at high pressure (3mbar). In this situation, the ions undergo frequent collisions on the way to the substrate and will not have enough kinetic energy for resputtering. The process of slowing down the fast oxygen ions is the so-called "thermalization". The other reason for using high oxygen pressure is the growing of high quality oxide films, which

requires full oxidation of the metal atoms deposited at the substrate surface. In general, the presence of oxygen in the plasma can increase the oxygen content in the growing film; however, it can also influence the film morphology.
The disadvantage of a high oxygen gas pressure during sputtering in this work is the appearance of some holes on the film surface. However, the homogeneity of the surface is very important, especially in case of perpendicular "c-axis" transport [32].

2.2 Superlattices for in-plane transport measurements.

2.2.1 Preparation

For preparation of superlattices the substrate holder was turned from the YBCO target to the PBCO target and this process was repeated until 200 nm thickness was reached. Typical deposition rates are low enough, that the thickness of the individual layers can be controlled on the unit cell scale. The rotation of the holder and the deposition time at the targets were controlled by a computer via a stepper motor. Fig. 2.3 shows a photography of the burning plasma and the substrate heater during deposition.

2.2.2 Characterization

X-ray diffraction

In order to achieve a high structural quality of the superlattices, one must be able to deposit good single crystalline films of the individual compounds. PBCO and YBCO samples showed c axis orientation only. The full width at half maximum of the rocking curves of the (005) peak was $\Delta\omega \leqslant 0.2^o$ indicating a good epitaxy. This is the basis for a c axis oriented epitaxial growth of the superlattices.

Low angle diffraction, and simulation

The superlattice quality is determined by comparison to simulated diffraction patterns using the program SUPREX; this program was developed by Fullerton et al. [33] to model the X-ray diffraction profiles from superlattices. The combination of n_Y YBCO and n_P PBCO unit cells defines a new supercell with a large c axis and consequently a small reciprocal lattice vector, which shows up in

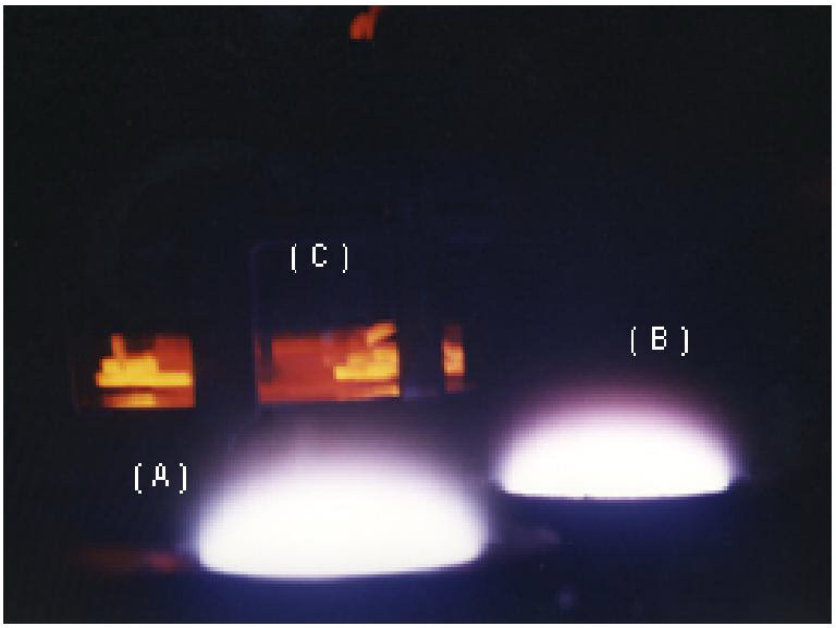

Figure 2.3: Targets and the heated substrate in the sputtering chamber, (A) is the plasma on the YBCO target, (B) on the PBCO target, and (C) substrate heater.

satellite reflections. With the angular position of two consecutive satellites, the modulation length $\Lambda = (n_Y + n_P) \cdot c$ was determined, where c is the c-axis length. Moreover, the modulation length is given by $\Lambda = r_Y \cdot t_Y + r_P \cdot t_P$, where r are the deposition rates and t the known deposition times, respectively. Therefore, we can determine the rates and optimize the exact deposition times for growing a single cell of each material.

By using low angle x-ray diffraction the finite size thickness oscillations can be detected (see figure 2.5). The thickness calculated from these oscillations will be a good indication to estimate the first target's rate. To find the right rate with higher accuracy many Y/P superlattice samples with different modulation lengths were prepared. From the modulation lengths of successive superlattices

$$\begin{aligned} \Lambda &= r_Y \cdot t_Y + r_P \cdot t_P \\ \Lambda' &= r_Y \cdot t_Y' + r_P \cdot t_P', \end{aligned}$$

one can set up two equations with different modulation lengths and times but the respective rates are assumed to be identical. Therefore, by solving these

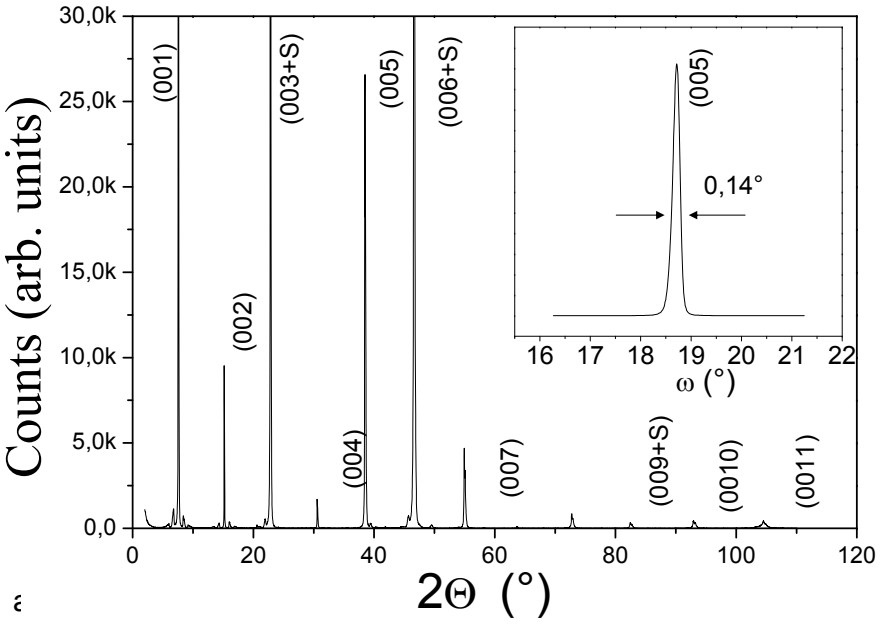

Figure 2.4: X-ray diffraction of a $(YBCO)_2$ /$(PrBCO)_6$ sample. The full range $\theta/2\theta$ scan is in linear scale with an inset showing the rocking curve of the (005) reflection.

two equations, the result will give us the new rates of the targets r_Y and r_P. The new rates will be used for preparation of the next Y/P sample (with different modulation length). By iterative application of this method we get fixed rates. In this work more than 15 different Y/P superlattic samples were prepared to get stable rates for both of the targets. Figure 2.6 shows the change in the target's rate r_Y and r_P ($YBa_2Cu_3O_7$ and $PrBa_2Cu_3O_7$) with different Y/P samples until stable rates were achieved. This iterative procedure was necessary as obviously the sputtering process slowly changes in time due to aging of the target. Physical origins for the target aging are presumably a change in the oxygen content during time and a compaction of the target surface induced by the sputtering plasma.

The appearance of satellite peaks in x-ray diffraction proves the spatial periodicity of superlattices. From the intensity and the position of the satellite lines one can get information on the superlattice quality. As a direct inversion of the x-ray pattern to the spatial structure is impossible due to the loss of phase

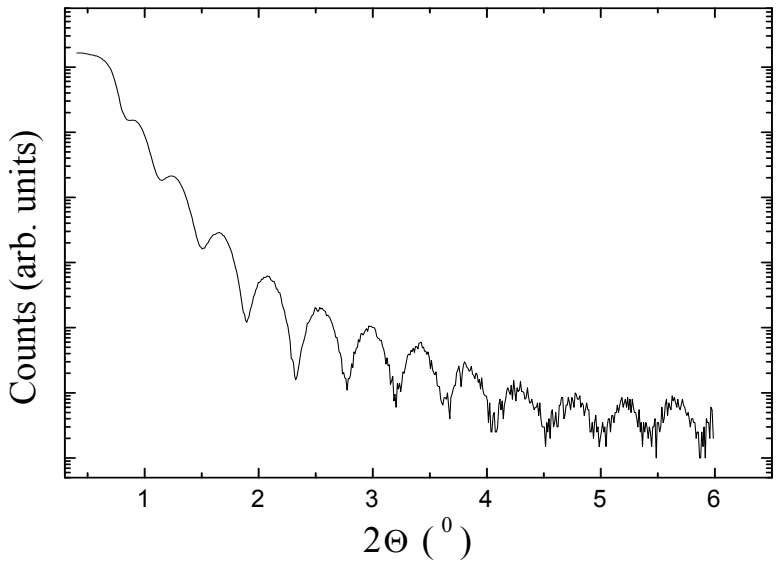

Figure 2.5: Low angle X-ray diffractogram of an $YBa_2Cu_3O_7$ film.

information in the diffraction experiment, the simulation of the diffraction patterns is the suitable method. In the SUPREX program, the parameters relating to the crystal structure of *YBCO* and *PBCO* are kept fixed, while the superlattice parameters are adjusted. Here the number of *YBCO* and *PBCO* layers, n_Y and n_P, are free parameters which are allowed to be non integer and to have a distribution n_Y and n_P. As the c-axis oriented individual layers grow unit cell by unit cell, the thickness of an individual layer at a given position must be a multiple of one unit cell. However, as the superlattice consists of many bilayers the thickness of different bilayers in different heights from the substrate surface can differ by integer numbers. Thus non-integer values indicate the average thickness. If these thicknesses are different at different locations in the sample an additional weakening of the satellite lines occurs, which is reflected in the distribution parameters σ_{nY} and σ_{nP}. An interdiffusion parameter allows for exchange between Y and Pr atoms in the crystal structure, which is found to be usually very small ($<$1%). At the interface of *YBCO* and *PBCO* layers, which do not have an identical crystal structure, lattice distortions lead to small fluctuations of the lattice distances directly at the interfaces. In the simulated curve of Fig. 2.7, we used the parameters n_Y=2.0, σ_{nY} =0.1 and n_P=6.0, σ_{nP} =0.1

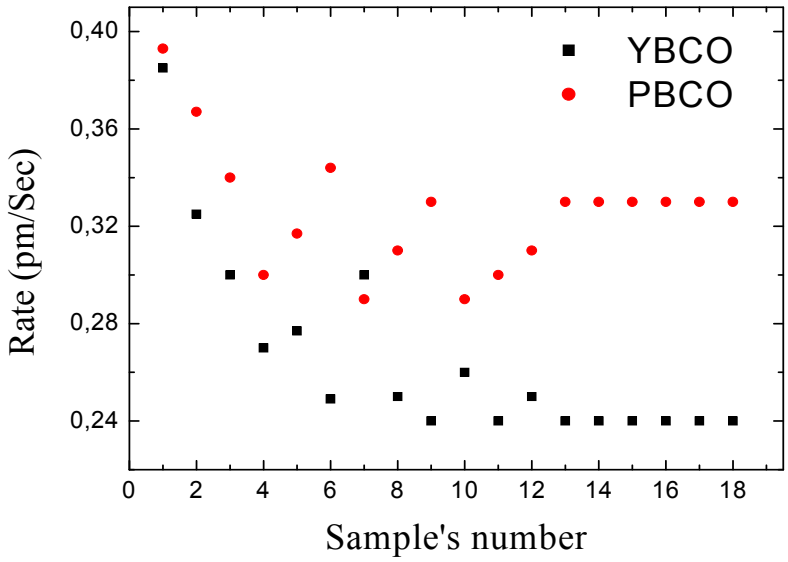

Figure 2.6: $YBa_2Cu_3O_7$ and $PrBa_2Cu_3O_7$ sputtering rate as a function of sample number.

with a continuous interface roughness of 0.02 nm and 1% interdiffusion. These parameters indicate a quite perfect superlattice structure, which was confirmed by previous transmission electron microscopy (TEM) studies on such samples [34].

Magnetic susceptibility

Magnetic susceptibility is the cange in magnetization of a material in response to an applied magnetic field. If it is negative, the material is diamagnetic. AC-susceptibility can be measured as a function of temperature by placing the specimen in a mutual inductance bridge (MIB). Therefore it is quick and easy to measure the transition temperature of superconducting materials. Another advantage is that no contact wires need to be used and thus the surface is not damaged during measurement. We use equipment that works on the principle whereby an alternating current is driven through a field coil. This alternating current generates a small alternating field (generally less than 1 mT) along the axis of the coil, which induces a voltage in the first pick up coil (reference) and

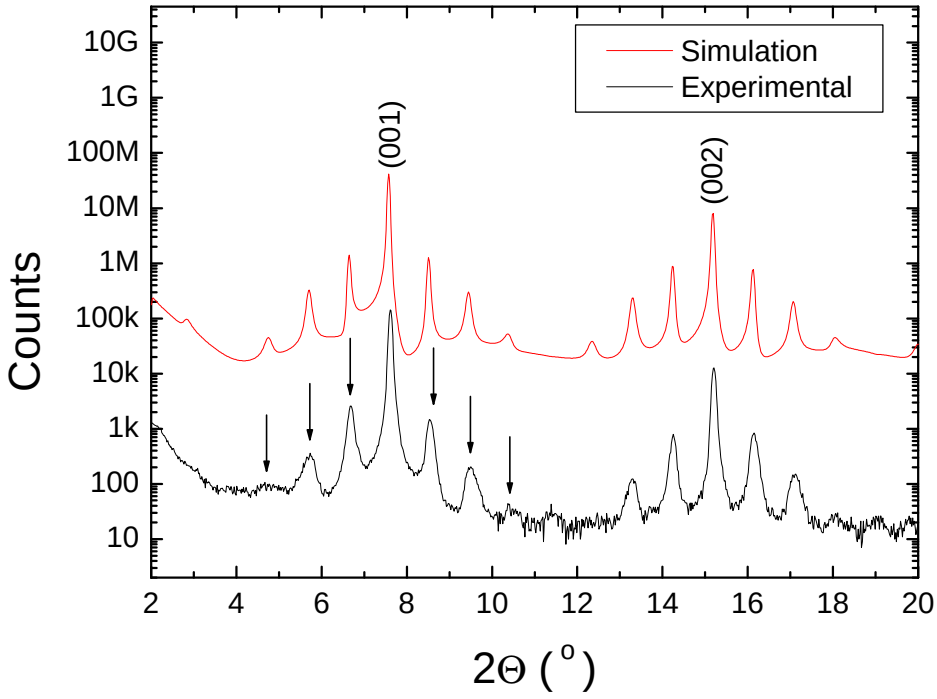

Figure 2.7: Zoom of the low angle region shown in logarithmic scale in order to enhance visibility of the satellite peaks, which prove the additional periodicity. The curve shows experimental (simulated) data for $(YBa_2Cu_3O_7)_2/(PrBa_2Cu_3O_7)_6$.

a voltage in the second coil (where the sample is inside). When a specimen is placed in the sample coil, the alternating magnetic field induces a voltage in the sample. In the superconducting state this leads to screening currents and reduction of the signal of the sample pick up coil.

2.2.3 Photolithography and transport measurements

In this section, the experimental methods used to do the photolithography process and transport measurements will be briefly discussed. In order to achieve patterning dimensions in a range well below one millimeter in case of pure $YBCO$ films or YP-superlattices (in-plane bridges) or a few micrometers in case of superlattices (out-of-plane measurements), photolithographic procedures have been employed. Photolithography is a method to create patterns on a film by using

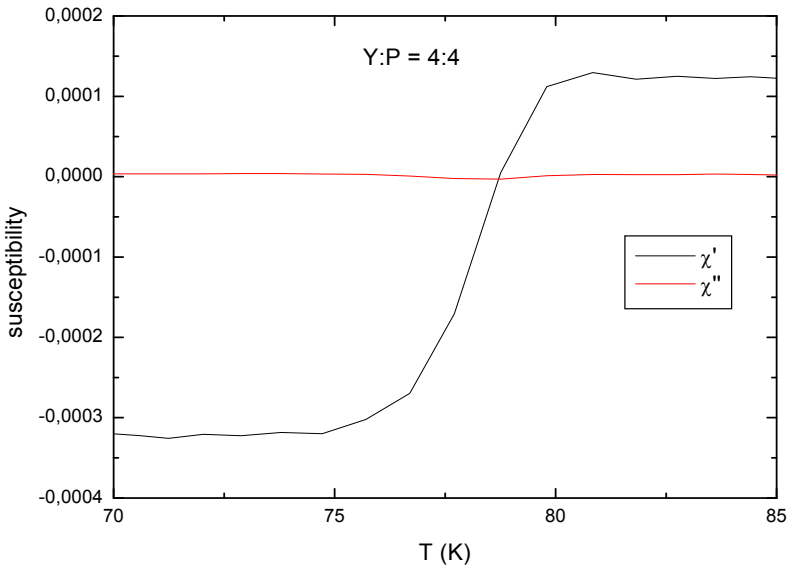

Figure 2.8: Superconducting phase transition of Y4/P4 superlattice as seen by *ac*-susceptibility.

light. It is the means by which the small-scale features of integrated circuits are created.

Patterning

Before starting the patterning processes additional gold spots were deposited in a coating machine to serve as contact pads. They were annealed in the $YBCO$ deposition chamber at 600 ^{o}C for 2 min in vacuum. This leads to a diffusion of the gold into the film surface and provides a low resistance ohmic contact. After the two minutes annealing time the chamber is filled with oxygen (800 mbar) and the cooling program following the initial film deposition is repeated in order to compensate for a possible oxygen loss in the previous annealing step.

Photolithographic patterning is done in the clean room of the institute of physics. Before the resist is applied to the substrate (film + substrate), the surface is cleaned to remove any traces of contamination from the surface such as dust, organic, ionic and metallic compounds. After that, the film is covered with a layer of radiation-sensitive photoresist ma-P 1215 (micro resist technology

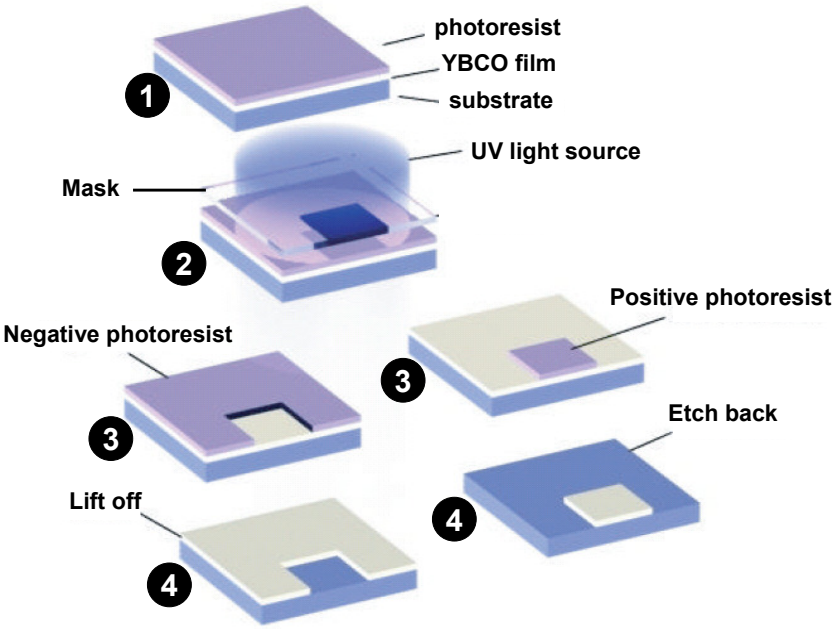

Figure 2.9: The main process steps in photolithography using the proximity method.

GmbH), which is distributed by a spinner rotating at 300 rpm 10 sec. and then 3000 rpm for 30 sec. The resulting thickness is related to the viscosity, angular velocity and time of spinning. The resist needs to be baked before an exposition to UV light through a mask can be performed. The UV light is produced by a mercury discharge lamp. During the exposure process, the resist undergoes a chemical reaction. Depending on the chemical composition of resist, it can react in two ways when the light strikes the surface. The action of light on a negative resist causes it to become polymerized where it has been exposed to the light. A positive resist has the reverse property. Exposure to UV light causes the resist to decompose. By using negative/positive resist, either the regions not exposed/exposed to the light will washed out with a suitable developer. After the developing process, a negative/positive of the mask remains as a pattern of resist. At this point one can perform either chemical or ion beam etching to remove the unprotected areas. Finally, a suitable solvent removes the residual photoresist and only the desired structure remains.

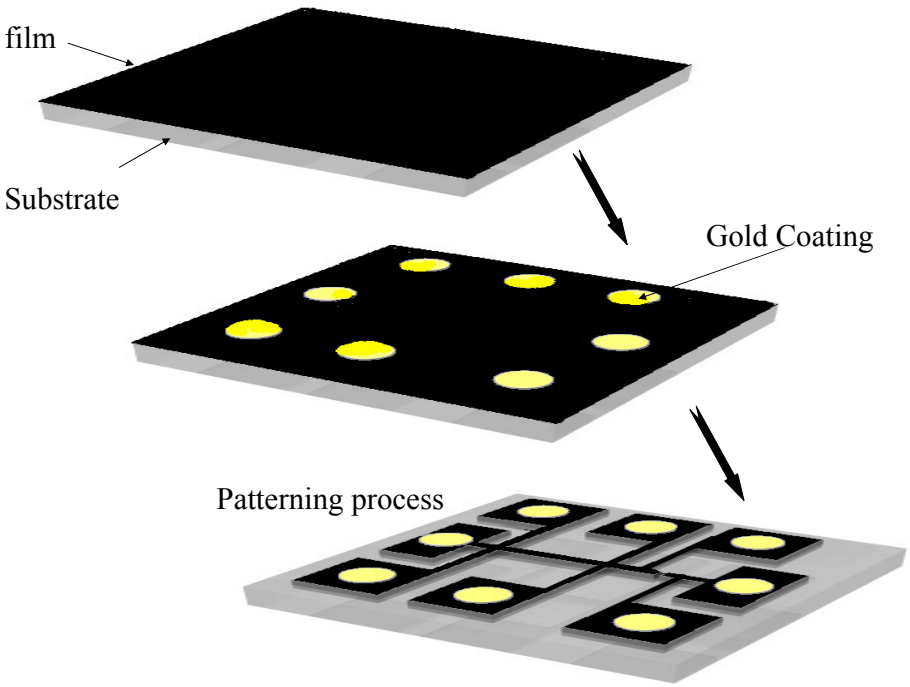

Figure 2.10: Process steps of lithography.

Transport measurements

Measuring the current-voltage characteristics by a four-probe method is a standard experimental technique to eliminate contact reistances. Therefore the four-probe method is a technique for determining the resistance of low resistance materials and essential for measurement of superconductors, see figure 2.11.

2.3 Y/P superlattices for out-of-plane transport

2.3.1 Preparation and characterization

Essentially the preparation and characterization is closely related to that for in-plane superlattices. However, the arrangement of the layers during deposition is different. First a ground YBCO layer of about 150 nm thickness is deposited followed by the $YBa_2Cu_3O_7/PrBa_2Cu_3O_7$ superlattice of 200 nm thickness, then again 50 nm of YBCO and finally the film is protected by a 200 nm gold layer.

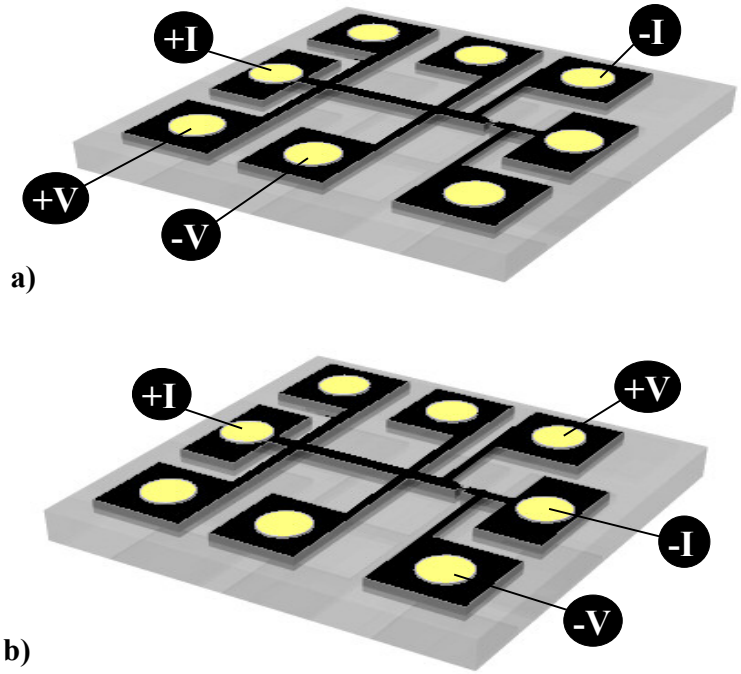

Figure 2.11: Geometry for four-probe measurements, with a) big bridge 200μm width and b) small bridge10 μm width.

The main difference between samples for in-plane and out-of-plane measurements is:

- Samples for in-plane transport measurements have the YP-superlattice directly on the substrate, and the first layer every time starts with PBCO because it grows smoother on $SrTiO_3$ substrate than YBCO.

- Samples for out-of-plane transport measurements have the YP-superlattice in between YBCO layers as a sandwich. Gold protection in this case is very important. For these samples the mixing of oxygen and argon as a sputtering gas has proven useful to overcome the pinhole problem and to reduce roughness.

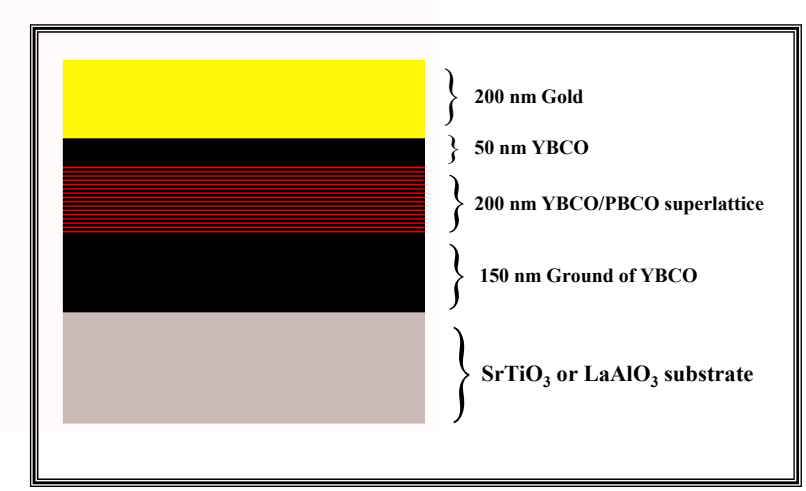

Figure 2.12: Lateral view of a Y/P superlattice for out of plane transport measurement.

2.3.2 Y/P superlattice photolithography

One of the important goals of micro or nano-electronic applications is to make the devices as small as possible in order to reduce the power needed. This is also important for superlattices in order to reduce heating effects. That is why we need every time to search for the smallest mesa. For this purpose, to achieve pattering dimension with the smallest mesa, photolithography is used. The patterning is similar to that for in-plane measurements as described in sec. 2.2.3.

Mesa structure

To fabricate the mesa structures in this work there are many steps necessary, e.g. several etching steps using chemical and ion-beam mechanisms. Above the ground electrode (150 nm YBCO) eight mesas are constructed with different square sizes between 16×16 μm^2 and 50×50 μm^2. These mesas were patterned by photolithography close to the longitudinal edges of the ground electrode which had the dimension of 10 mm×1 mm and was patterned as seen in Fig. 2.13. Subsequently, the sample was subjected to ion beam etching where the unprotected part was removed by ion milling until a depth of about more than 450 nm was reached (related to superlattice + top YBCO layer + gold layer). Then the photoresist was removed with acetone and plasma etching what guarantees a

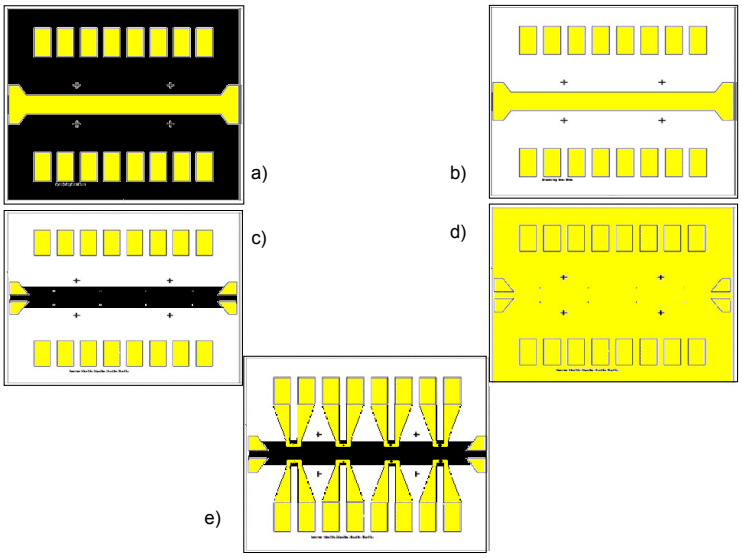

Figure 2.13: Sketches indicating the patterning steps. a) After using a positive resist with suitable mask and developer, the unused parts of gold are removed by chemical etching. b) In a second, different chemical etching step the unused residual film is etched down until the substrate surface appears. c) There are three important steps: 1- Mesa dimension construction by means of positive resist and developer. 2- Ion-beam etching until reaching the YBCO ground electrode. 3- Negative resist with suitable mask to make a window on the top of mesa. d) Sample covered completely with gold in order to make two gold terminals for every mesa through the windows. e) Using a positive resist and developer, the unused parts of gold are removed by chemical etching.

clean surface on the top of the mesa. The patterned sample was coated again with a negative photoresist which will be also used as an insulator around each mesa. A small window has to be opened on the top of each mesa. In order to avoid short circuit due to mismatch of the alignment, the window areas must be smaller than the mesa area. A mask with four 10×10 μm^2 and four 16×16 μm^2 squares was used for this purpose. Additionally a mask aligner that allows to position the mask onto the mesas with a resolution of about 2 μm was built.

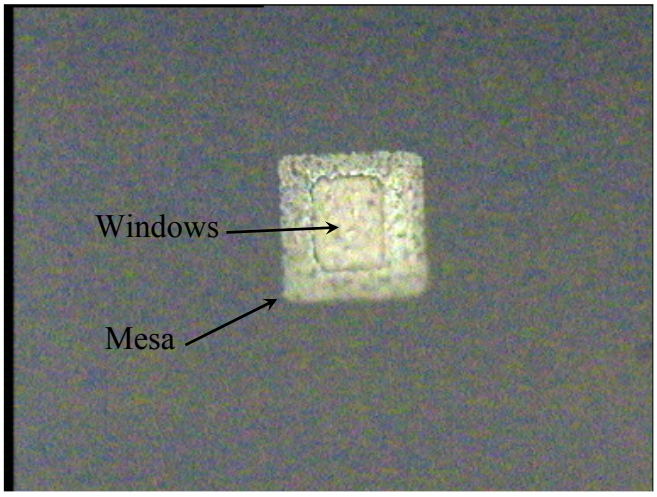

Figure 2.14: Top of view for the windows o the top of mesa after step c in 2.13.

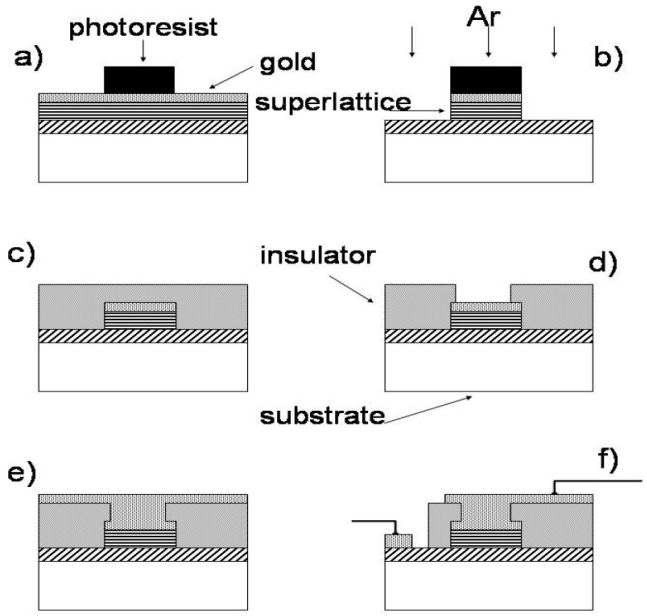

Figure 2.15: Fabrication process of mesa structures using photolithography and argon ion milling.

Wiring the junction

In order to wire the mesa, a window on the top of each mesa was opened by photolithography. This process was very delicate because inside the window the surface must be free of photoresist residues. The photoresist outside the window served as insulating layer, because it has properties like a polyimide.

After using the photoresist, a soft annealing step is very important to dry the photoresist. In this case after the photoresist cooled again to the room temperature, it will be selectively illuminated with UV light. For this purpose a glass mask with the fine desired structure is used fig. 2.15. When the photoresist is exposed to the UV light, it will induce a change in the chemical properties of the photoresist and the illuminated area can be removed with an appropriate liquid developer. Now, the photoresist-free area (negative photoresist) can be etched and removed. Generally, chemical etching or ion beam etching can be used. In chemical etching, the sample is typically exposed to an acid ($HNO_4 : H_2O \equiv 1 : 400$) which dissolves the unprotected film. The disadvantage of using this method is that it is very diffcult to control the etched depth of the film. It is important to notice that superlattice layers must remain to send a current through the mesa. On the other hand, it is not clear if the acid also destroys or dissolves the layers under the photoresist or not. For these reasons, the ion beam is the best choice. The samples are etched in an argon ion etching chamber situated inside the clean room where the lithography is carried out. The quantity of material removed from the sample is proportional to the bombardment time. A reference sample with the same thickness of the top electrode (mesa) can be etched simultaneously, until the substrate of the reference sample appears. The etching process is continued until a part of the bottom electrode is also etched. After the etching process, the sample is in the situation shown in Fig. 2.15. The sample is cleaned with aceton and ultrasound to remove the residual particles. After that we use a negative photoresist to open the window with the same steps as before in fig. 2.14.

Using photolithograpic (negative photoresist) patterning again a window with an area smaller than the mesas area is opened (Fig. 2.15) with the same steps as before. This step is very delicate because a mismatch in the alignment between window and mesa can lead to short circuits between the base electrode and the contact leads. Afterwards the photoresist is hardened in U.V. light and at 180^0C baking temperature it becomes mechanically stable. Subsequently the sample is transfered carefully from the clean room in an exsiccator to minimize the contact with air and dust particles and put into a sputtering chamber where a 200 nm thick gold layer is deposited (Fig. 2.15). Finally the gold layer is patterned

photolithographically into contact leads and the $YBa_2Cu_3O_7/PrBa_2Cu_3O_7$ superlattice device is contacted with Au bonding pads (Fig. 2.15).

Chip layout

There are three important parts: ground electrode $YBa_2Cu_3O_7$, heterostructure mesa (superlattice) embedded in an insulator (hardened photoresist) and gold leads on the top. Figure 2.13 shows the chip layout, where the base electrode is represented by a shadowed rectangle, eight mesas are located over the electrode together with a pair of pads on the ends of the base electrode, just above each mesa there is a gold strip. The out-of-plane transport properties are measured as sketched in Fig. 2.13. In fact a true four point measurements was not possible because of the small window size the current and voltage pads on the mesa could not be separated. A splitting into two pads is very diffcult. All measurements were carried out in this geometry where the contact resistance on the top of the mesa is included. The in-plane transport properties of the ground layers can be measured using the four pads at the ends of the base electrode as in fig 2.16.

2.4 Y/P superlattice photolithography for relaxation measurements

The samples (YBCO or Y/P superlattice) were prepared by the same method as mentioned before. Standard dc magnetization measurements were performed on disk-shaped with radius 2 mm as shown in Fig. 2.17

2.5 Thick $YBa_2Cu_3O_7/PrBa_2Cu_3O_7$ superlattices

The sputter chamber has stable deposition parameters that allow to run continually 29 hours in order to produce thick films, where the actual film contains a $YBa_2Cu_3O_7/PrBa_2Cu_3O_7$ superlattice with ($1\mu m$) thickness between two YBCO electrode (50 nm) on the top and (150 nm) on the bottom. Finally, the film is in-situ covered with (200 nm) gold as protection layer.

Patterning and layout

These thick films were prepared for patterning experiments using a focussed ion-beam (FIB) system. In such a system a focussed ion beam is rastered over

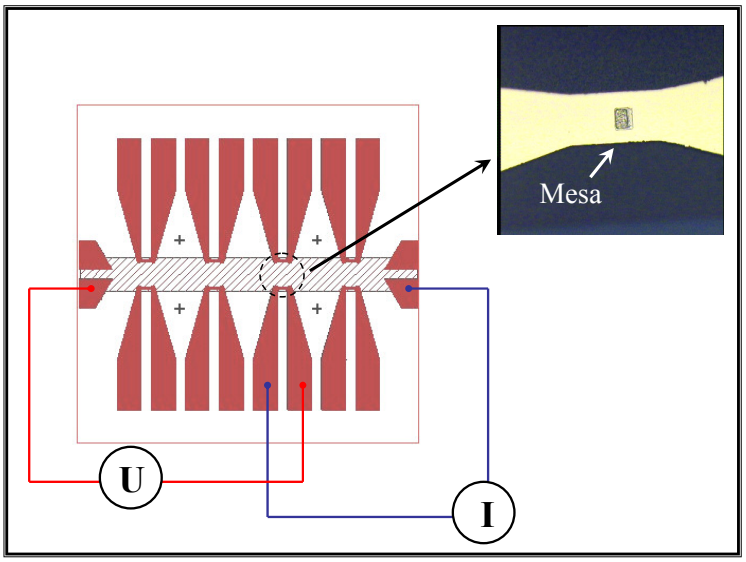

a)

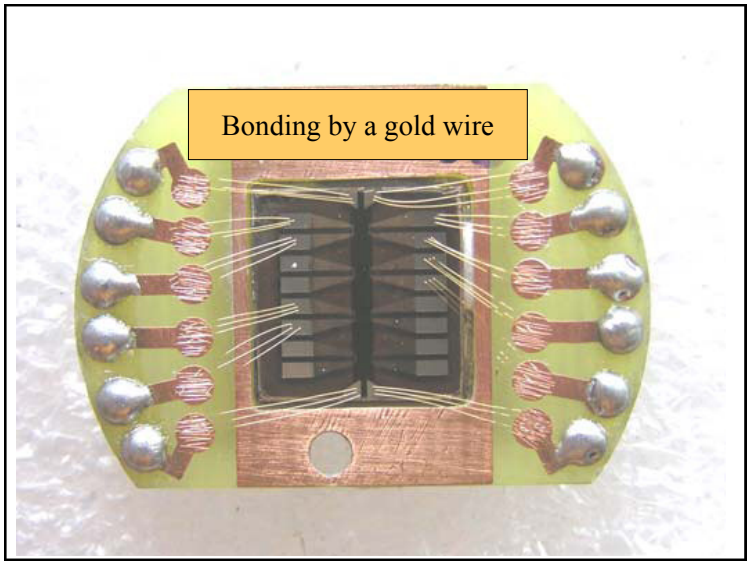

b)

Figure 2.16: Top view of the chip after step e in fig 2.13. a) The striped rectangle represents the ground electrode, each mesa was contacted with a gold strip. The out-of-plane electrical measurement was performed between the pads (on the base) and the gold strip, the detail shows a picture of a mesa structure contacted with gold strip (top right). b) The actual chip layout after bonding step.

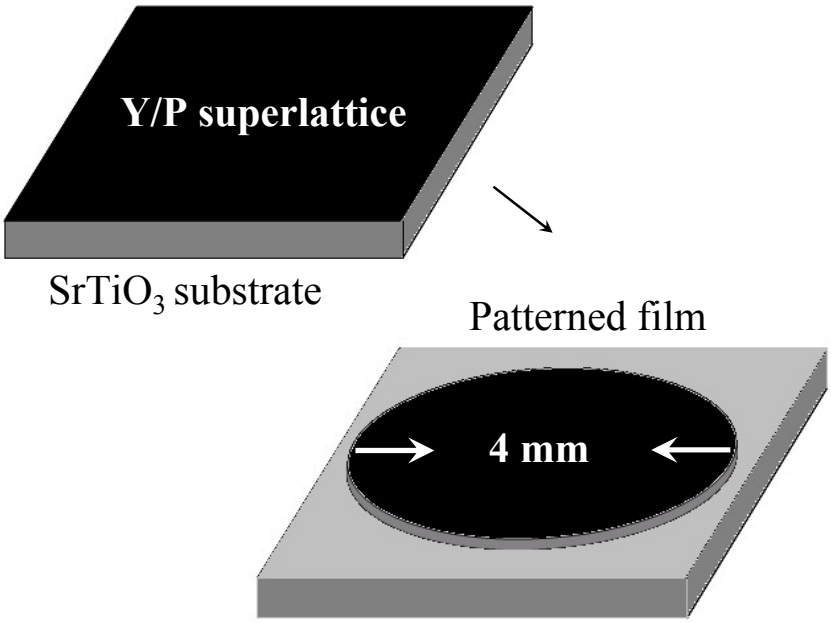

Figure 2.17: Patterning steps of $YBa_2Cu_3O_7/PrBa_2Cu_3O_7$ superlattices for magnetic relaxation measurements .

the surface and sputters the film locally. It offers additional degrees of freedom as will be evident below. Here the FIB system of the University of Frankfurt could be used in cooperation with Prof. Dr. M. Huth. However, due to the rasterizing process only very small areas can be directly patterned using the FIB and a prepatterning step using optical lithography is necessary. After the photolithography an ion-etching step should be performed. However, with the existing equipment it will take longer than 10 hours to etch $2.45\mu m$ (700 nm PrBCO, 300 nm YBCO, $1\mu m$ Y/P superlattice, 400 nm YBCO, and 50 nm Gold). Cathode lifetime and general stability of the ion etch system prohibited use of this method. Therefore chemical etching was necessary. The normal way to etch YBCO films chemically uses diluted nitric acid ($HNO_3 : H_2O \equiv 1 : 400$). However, for the very thick films underetching the photoresist is a severe problem. As evident in Fig. 2.18, it is clear that the acid dissolves the layers under the photoresist. For these reasons, a combination of ion beam + acid was the best choice.

Using this combination the film is patterned to define a $10\mu m$ track with four contacts. After using a focused ion beam (FIB), a portion of this track

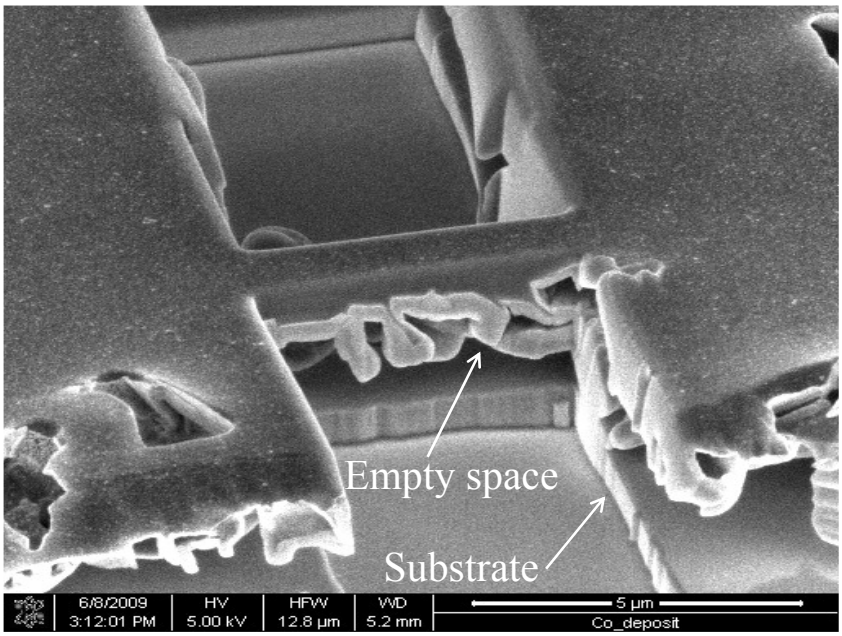

a)

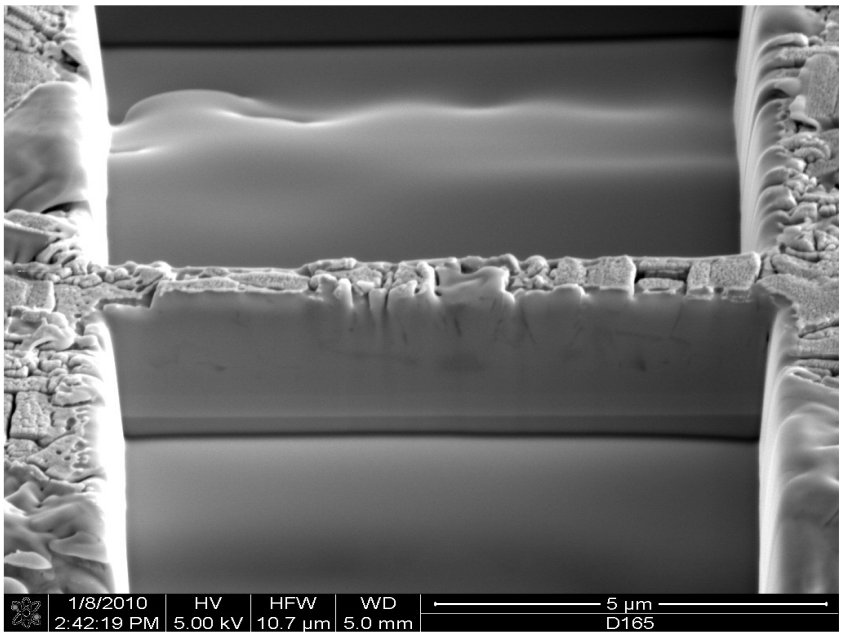

b)

Figure 2.18: a) Underetching produced using chemical etching only on a thick film. The view is from the side after a segment of the bridge has been removed using the FIB. Though in a perpendicular view in the light microscope the bridge looks o.k., the underetching is nearly complete. b) Thick film with optimal patterning with focused ion beam (FIB). The underetching has completly disappeared.

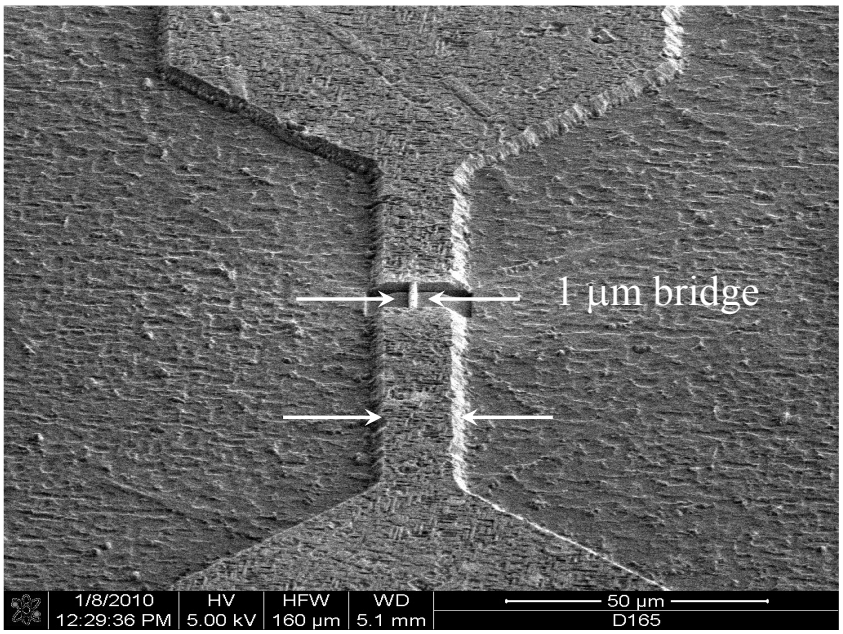

a)

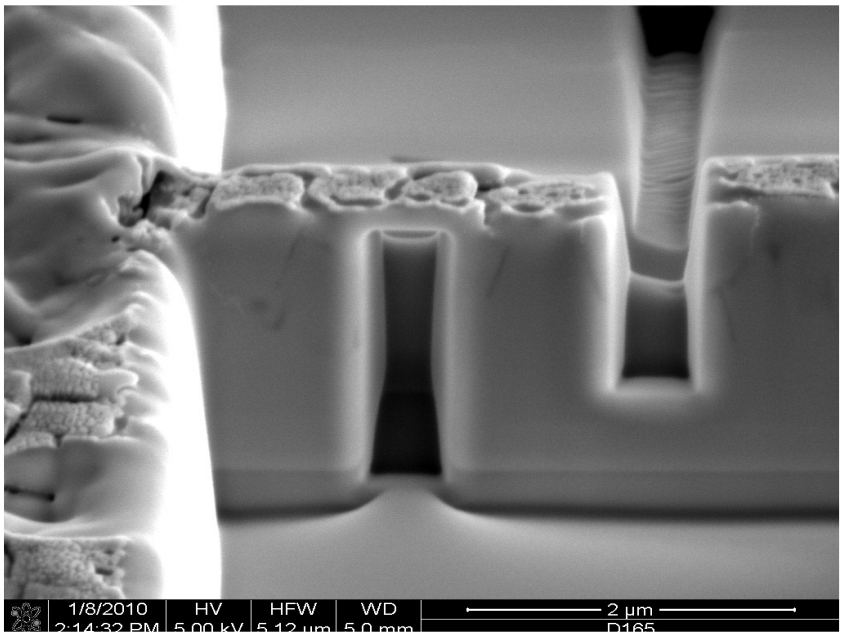

b)

Figure 2.19: a) The film is patterned to define a $10\mu m$ track. Using a focused ion beam (FIB), a portion of this track is narrowed to $1\mu m$. b) The lateral cut is made from top at one position of this track with a lateral distance of $1\mu m$ or smaller a cut is made from below.

is narrowed to $1\mu m$. Then a lateral cut is made from top at one position of this track. At a lateral distance of $1\mu m$ or smaller a cut is made from below, i.e. a hole is drilled in the remaining bridge close to the substrate which leaves the surface intact. Finally, as shown in fig 2.19 the current will flow vertically through the superlattices with area dimension $1 \times 1\mu m^2$.

CHAPTER 3

IN-PLANE TRANSPORT

Introduction

In this chapter I will introduce first the comparison between the different crystal structures of YBCO and then the matching with $SrTiO_3$ substrate for epitaxial growth. The main content of this chapter, however, will be the investigation of the vortex dynamics in superlattices in a geometry where the current flows in the plane of the superlattices and the magnetic field is applied perpendicular to the film. The vortex-creep activation energy U is determined by analyzing the in-plane resistive transition of 200 μm and 10 μm wide bridges with the external magnetic field B oriented along the c-axis. The activation energies for two series of superlattices were investigated. In one series $(YBa_2Cu_3O_7)_4/(PrBa_2Cu_3O_7)_{nP}$ the thickness of the YBCO layers was constant ($nY = 4$) and the number of the PBCO unit cells was varied, while in the other series $(YBa_2Cu_3O_7)_{nY}/(PrBa_2Cu_3O_7)_4$ the number of PBCO layers $nP = 4$ was constant and nY varied. $YBa_2Cu_3O_7/PrBa_2Cu_3O_7$ superlattices represent a model system which has been widely studied [9, 14, 13, 35, 36, 37, 38]. The aim was to determine the effect of thickness and external magnetic field on the activation energy for these two series. In these results the strength of the coupling of the vortex system in neighbouring YBCO layers is visible.

3.1 Crystal structure

After the discovery of superconductivity in $(La, Ba)_2CuO_4$ by Bednorz and Müller (1986) with transition temperature T_c 35 K, the $YBa_2Cu_3O_{7-\delta}$ was discovered with T_c above 90 K [39]. This structure is very sensitive to the value of the oxygen deficiency δ. For $\delta = 0.03$ the highest T_c of 92 K is observed.

3.1.1 Orthorhombic and tetragonal structures

The general chemical formula of perovskite systems is ABO_3. The perovskite structure is cubic with (A) at the centre of the unit cell, (B) at the corners and the oxygen sites at the centre of the cube edges. The $YBa_2Cu_3O_{7-\delta}$ unit cell consists of three cube structures, the first one is an $YCuO_3$ cube at the centre and the other two are $BaCuO_3$ above and below the first one. However, oxygen sites on the same horizontal plane as the yttrium atom are never occupied, so that O_3 atoms in the neighbouring planes are allowed to move slightly in Y direction. The oxygen content is variable in the basal plane. For $\delta = 0$ the oxygen positions at the basal plane are half filled with oxygen atoms arranged in rows resulting in the orthorhombic structure shown in 3.1 left. It yields the highest T_c with nearly full oxygenation when $\delta = 0.03$. In the fully underdoped case the basal plane is void of oxygen atoms resulting in the tetragonal structure shown in Fig. 3.1 right. Concerning the critical temperature the three cases related to the relation between δ and T_c are,

- When $\delta > 0.03$ lower T_c (Under doped)
- When $\delta = 0.03$ highest T_c (Optimum value)
- When $\delta < 0.03$ lower T_c (Over doped)

Exchanging the Y atom in this structure to Pr changes only slightly the lattice constants, but suppresses completely the superconductivity. As origin of this suppression it is assumed that Ba atoms interchange partly with the Pr atoms and their presence in the superconducting CuO_2 double planes is detrimental to superconductivity.

3.2 Matching between $YBa_2Cu_3O_7$ and $PrBa_2Cu_3O_7$

The *ab*-plane lattice parameters of $YBa_2Cu_3O_7$ and $PrBa_2Cu_3O_7$ are suitable for epitaxial growth on $SrTiO_3$ substrate which has a cubic structure with a

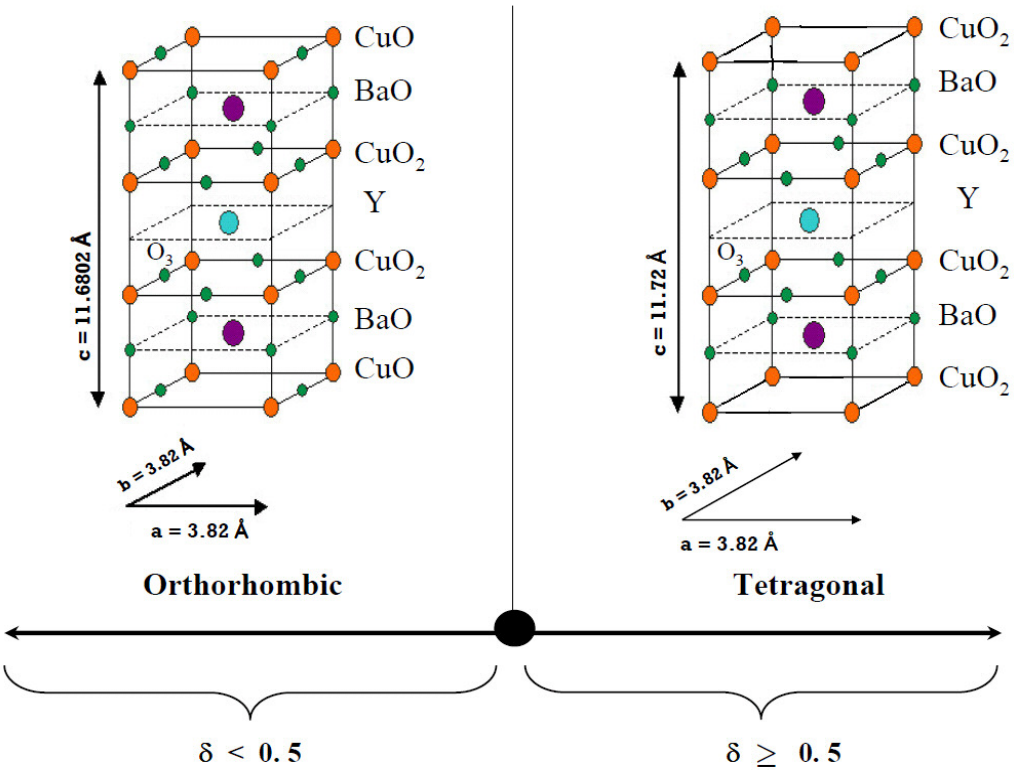

Figure 3.1: YBCO crystal structure for different oxygen content and the delta is close to zero in case of orthorhombic and close to 1 for tetragonal.

similar lattice parameter.

Form a long time, x-ray analysis has been a key tool for the study of thin film structures because it is non destructive and yields structural information on the atomic scale [40]. One can see this easily from the comparison between x-ray data of a YBCO film, a PBCO film and a Y/P superlattice in fig. 3.2. This figure is a x-ray scan around the (001) and (002) reflections of the YBCO structure (the material grows with the c-axis parallel to the growth direction). When compared to pure $YBa_2Cu_3O_7$ and $PrBa_2Cu_3O_7$ films (shown in fig. 3.2, red and green colour), the superlattice diffractogram has additional satellite peaks which are the signature of a modulated structure.

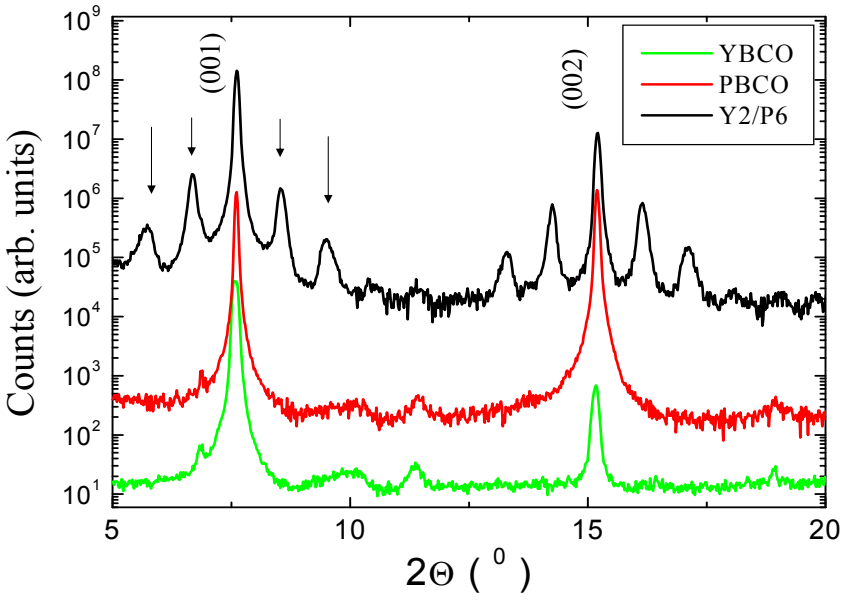

Figure 3.2: X-ray diffractograms in logarithmic scale of a $YBa_2Cu_3O_7$ film (green colour), a $PrBa_2Cu_3O_7$ film (red colour), and a 93,4 Å modulation length $(YBa_2Cu_3O_7)_2/(PrBa_2Cu_3O_7)_6$ superlattice (black colour). One sees satellite peaks (marked with arrows) around the (001) and (002) reflections that are related to the synthetically induced periodicity.

3.3 Vortex dynamics

Measurements of the magnetoresistivity $\rho(B)$ of the superlattices versus the temperature T were performed with DC magnetic field up to 6 Tesla parallel and perpendicular to the c axis, which is perpendicular and parallel to the film plane, respectively. The intrinsic anisotropy of the layered structure shows up in a stronger broadening of the transition for magnetic fields B perpendicular to the layered superlattice structure than for YBCO films, while for B parallel to the superlattice structure the magnetic field results in a reduced influence of the magnetic field on the resistive transition of the superlattice [41]. Qualitatively this was attributed to the cutting of the vortex lines by the PBCO layers [14]. In order to attain quantitative information the vortex-creep activation energy for different magnetic field strengths for a number of superlattices with constant PBCO thickness ($n_P = 4$) and varying YBCO thickness n_Y was determined.

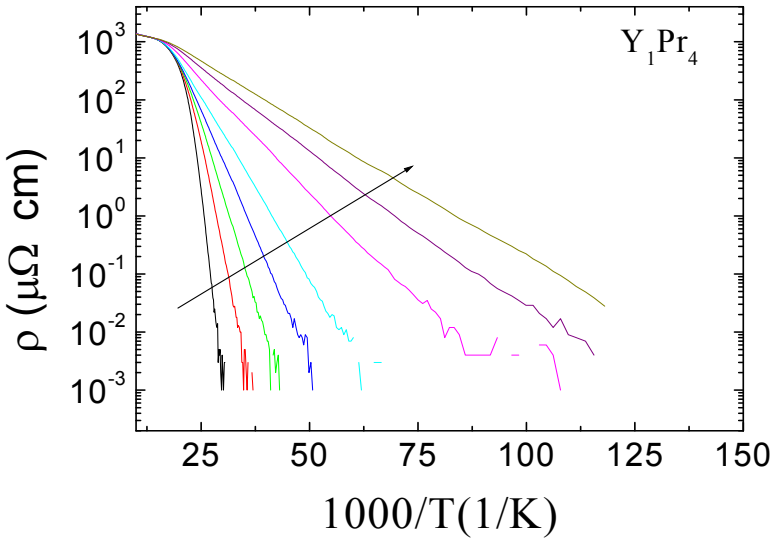

Figure 3.3: Resistive transitions for a superlattice with $n_P = 4$ in magnetic fields of increasing strength $B = 0, 0.125, 0.25, 0.5, 1, 2, 4$, and 6T. The number of unit cells of YBCO is $n_Y = 1$.

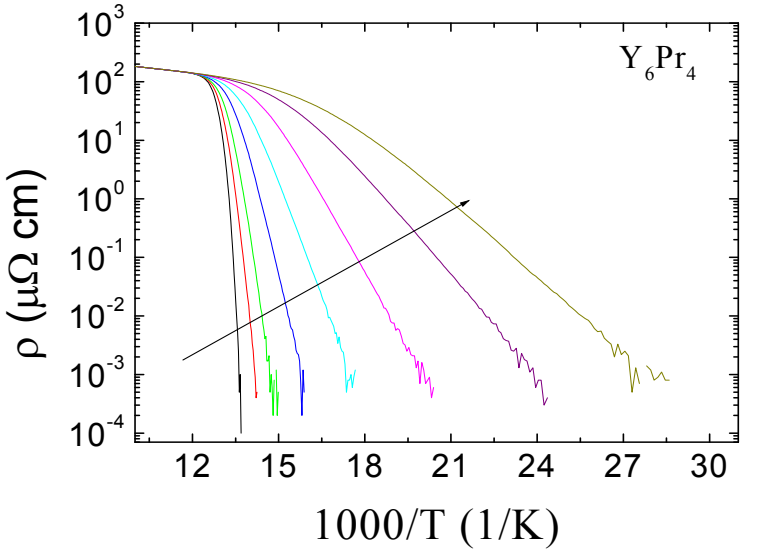

Figure 3.4: Resistive transitions for a superlattice with $n_P = 4$ in magnetic fields of increasing strength $B = 0, 0.125, 0.25, 0.5, 1, 2, 4$, and 6T. The number of unit cells of YBCO is $n_Y = 6$.

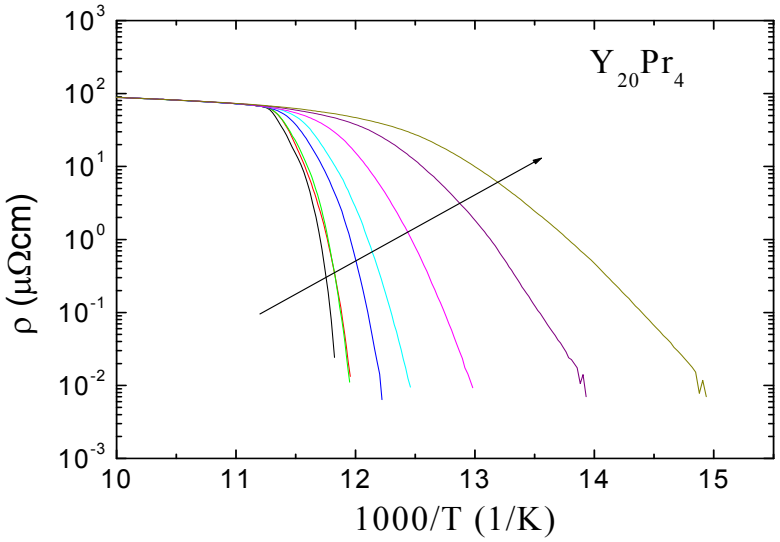

Figure 3.5: Resistive transitions for a superlattice with $n_P = 4$ in magnetic fields of increasing strength $B = 0, 0.125, 0.25, 0.5, 1, 2, 4$, and 6T. The number of unit cells of YBCO is $n_Y = 20$.

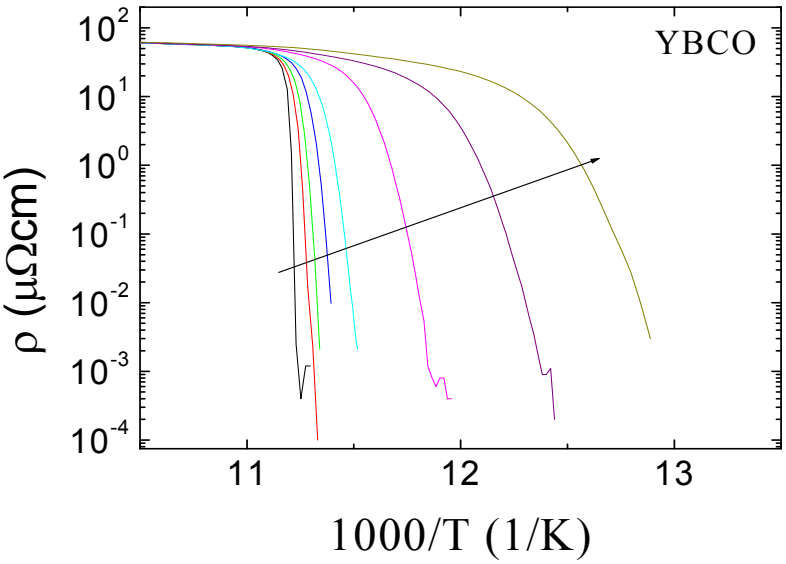

Figure 3.6: Resistive transitions with increasing a magnetic fields of strength $B = 0, 0.125, 0.25, 0.5, 1, 2, 4$, and 6T of a 200 nm thick YBCO film.

The standard technique to extract the activation energy U from the resistivity data is to plot $\ln(\rho(T))$ vs. the reciprocal temperature. Figs. 3.3 to 3.6 show Arrhenius plots of resistive transitions for $n_Y/(n_P = 4)$ superlattices. The data have been measured on 200 μm bridges with magnetic field perpendicular to the layered structure (i.e., along the c axis).

Assuming a temperature independent activation energy U_0, a straight line in the Arrhenius plot will appear, $\rho(T,B) = \rho_0 \exp\left(-\frac{U_0(B)}{T}\right)$. However, the activation energy must vanish close to the critical temperature T_c, where the condensation energy goes to zero. A T dependent activation energy U has to be taken into account, $\rho(T,B) = \rho_0 \exp\left(-\frac{U(T,B)}{T}\right)$, and the slope in the Arrhenius plot is given by $\frac{d[\ln \rho(T,B)]}{d(1/T)} = -U(T,B) + T\frac{dU(T,B)}{dT}$. In this situation, the appearance of a straight line in the Arrhenius plot implies that $U = U_0(1 - T/T_c)$, and the slope in the linear fit will supply U_0, the activation energy linearly extrapolated to $T = 0$.

There exists an immediate qualitative difference in the plots, where one sees straight lines for the superlattice with very thin YBCO layers $nY = 1$. With increasing YBCO thickness the resistive transitions in the Arrhenius plots become strongly curved. This curvature was explained first by Palstra et al. [42] and results from the temperature dependence of the condensation energy and the pinned volume. This indicates a different qualitative behaviour of the quasi two dimensional superlattices compared to YBCO. If one assumes a constant ρ_0 and a known value of T_c, where the activation energy vanishes the resistive transition can be inverted to get the full temperature dependence of the activation energy. However, this is an unusual treatment and for better comparison to literature the usual simple extraction of constant values of the activation energy U_0 by evaluating the slope in the low resistivity regime ($0.01\mu\Omega\text{cm} < \rho < 1\mu\Omega\text{cm}$) is used. The activation energies extracted in this manner are shown graphically in Fig. 3.7. In this figure as in the following figures k_B is used as the energy scale.

Even a single layer of PBCO of only one unit cell thickness has a tremendous influence on the FLL. The strong decrease of the activation energy as function of the PBCO thickness in Fig. 3.7a indicates that the correlation length of the flux lines along c axis direction is strongly reduced and the flux lines are cut into pancake vortices [43, 8]. If the thickness of the PBCO layer is increased to two unit cells a further drop of the activation energy is observed, which proves that the pancake vortices in neighbouring YBCO layers of the superlattice are still coupled by Josephson currents. Increasing the decoupling PBCO layer thickness to $n_P = 4$ leads to a further reduction, while for higher PBCO thicknesses a

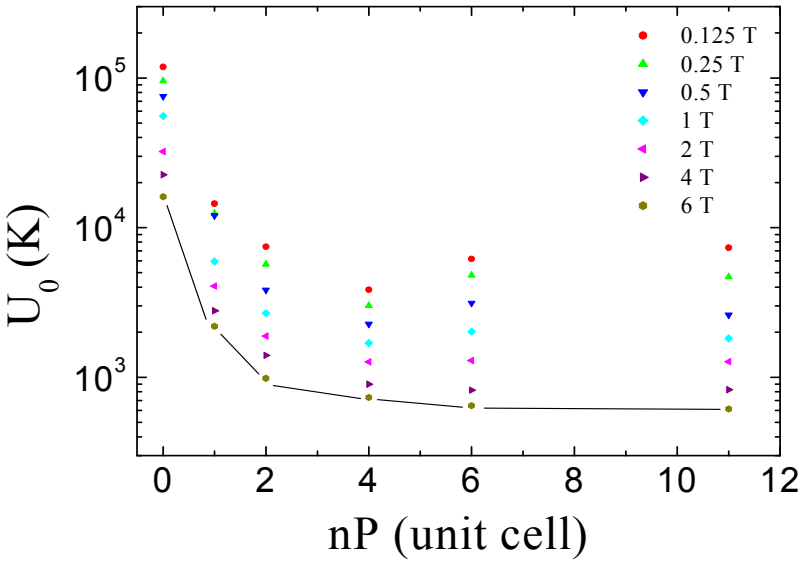

a)

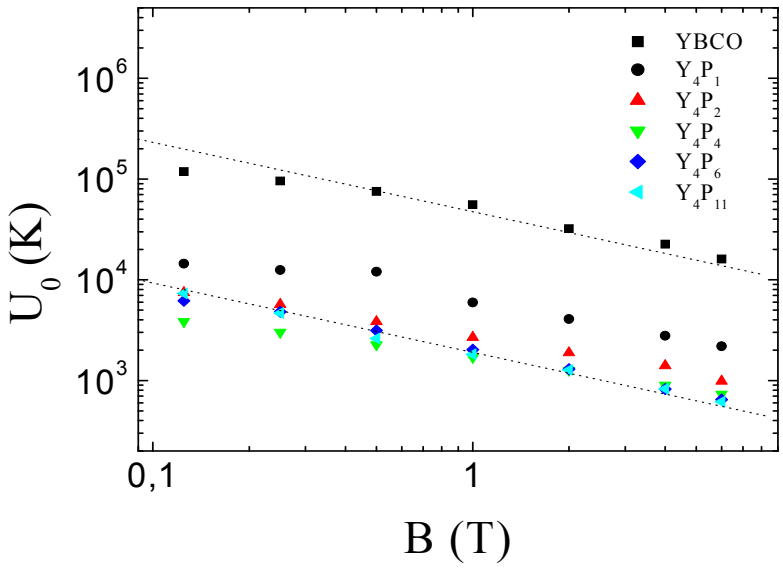

b)

Figure 3.7: Activation energies U_0 extracted from the slope of the Arrhenius plots for superlattices with PBCO layer thickness $n_P = 0, 1, 2, 4, 6$, and 11 for $n_Y = 4$ fixed and different magnetic fields $B = 0.125, 0.25, 0.5, 1, 2, 4$, and 6T. A thickness of $nP = 0$ represents actually not a superlattice but an YBCO film of 200 nm thickness. In a) the data are shown as function of the PBCO thickness, while in b) they are shown as function of the magnetic field.

saturation is evident. Thus one can conclude that for $n_P = 4$ the activation energy is dominated by the reduced correlation lengths in the individual YBCO layers of the superlattices and the possibly remaining residual Josephson coupling has a negligible influence for the vortex motion. In part b) of figure 3.7 the same data are redrawn as function of the magnetic field strength. The B dependence of U_0 is discussed below.

In order to study the influence of the correlation length on the activation energy separately, in the following the thickness of the PBCO layers was kept fixed $n_P = 4$ and the thickness of the YBCO layers n_Y was varied. The resulting thickness dependence of the activation energy is shown in Fig. 3.8a for different B values. As a guide for the eye additionally straight lines are shown in these plots. In the thickness range from 2 unit cells $n_Y = 2$ up to $n_Y = 80$ the lines have a slope 1. Such in this range there is a linear correlation between the YBCO layer thickness and the activation energy as was observed by Brunner et al. [14] using superlattices with $n_P = 8$. The maximum correlation length of the flux lines along c axis direction was concluded to be 45 nm by linear extrapolation in this work. In the samples here with $n_P = 4$, however, the correlation length seems to be closer to 90 nm. One must note that the flux line correlation length in c axis direction will not only depend on fundamental parameters like the vortex line energy, but also on sample dependent parameters. E.g. the sample microstructure leads to pinning which may be dominated by point pinning centres or by extended pinning centres as screw dislocations or twin planes. In the latter case longer correlation lengths are expected as the formation of vortex loops will be strongly suppressed. The sample with $n_Y = 80$ shows activation energies very close to that of an YBCO film and the lines in this thickness range are drawn horizontally. The step from 1 to 2 unit cells however, is qualitatively different. The line has a slope of 2 indicating a four times larger activation energy for double the thickness. This cannot be explained by the increase of the vortex line correlation length alone. Another reason is that the superconducting critical temperatures of the one unit cell thick $n_Y = 1$ superlattices are strongly reduced [44, 10, 12]. In this case the one unit cell thick YBCO layers are neighboured by insulating PBCO layers on both sides and finite size effects become important.

The scaling in Figs. 3.7b and 3.8b is chosen double logarithmically and the drawn dotted straight lines correspond to $U_0(B) \propto B^{-1/2}$. Besides the increase of the absolute value of the magnetic field exponent with increasing B [14], the data points indicate a power law $U_0(B)$ dependence with a mean exponent close to -0.5. This was also found for thin films of the two dimensional superconductor

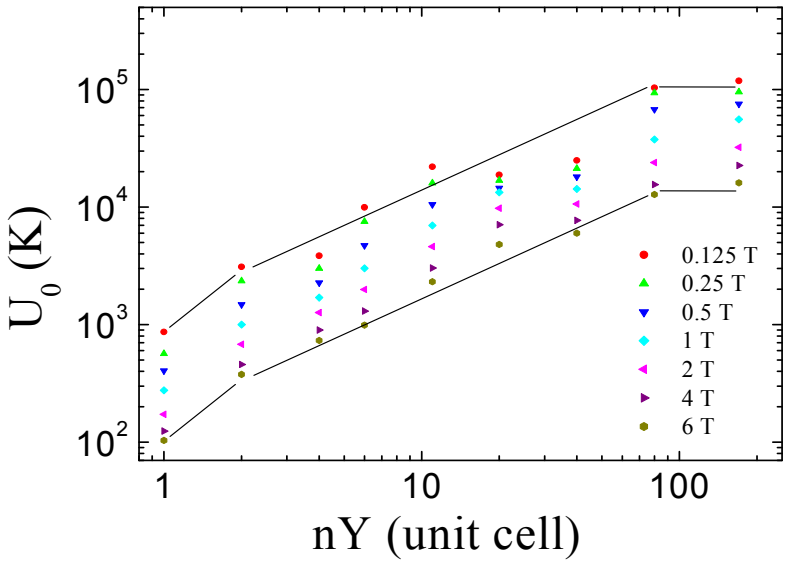

a)

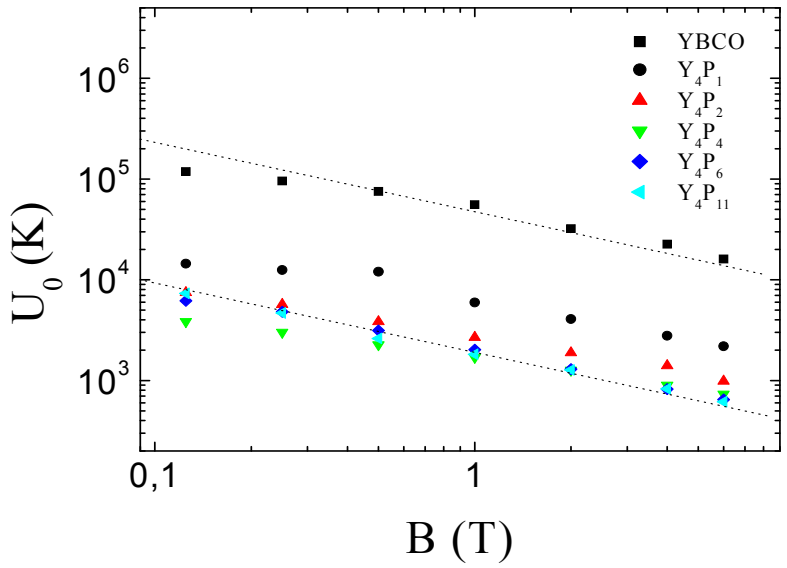

b)

Figure 3.8: Activation energies U_0 extracted from the slope of the Arrhenius plots for superlattices with YBCO layer thickness $n_Y = 1, 2, 4, 6, 8, 11, 20, 40,$ and 80 unit cells for $n_P = 4$ fixed and an YBCO film of 170 unit cells, i.e. 200 nm thickness, for different magnetic fields $B = 0.125, 0.25, 0.5, 1, 2, 4,$ and 6T. In a) the data are shown as function of the YBCO thickness, while in b) they are shown as function of the magnetic field.

$Bi_2Sr_2CaCu_2O_8$ by Kucera et al. [45]. Such a proportionality was explained as plastic movement of vortices in a vortex liquid by Vinokur, Feigelman, Geshkenbein and Larkin [46, 47]. The energy barrier for thermally activated shear is determined by the energy necessary to create double kinks in flux lines

$$U_{Pl} = 2E_k a_0 \approx \frac{2\Phi_0}{16\pi^2 \lambda_{ab}\lambda_c} \ln(\kappa) \left(\frac{\Phi_0}{B}\right)^{1/2} \tag{3.1}$$

where E_k is the characteristic kink formation energy, $a_0 \approx (\phi_0/B)^{1/2}$ is the average distance between flux lines, ϕ_0 - the flux quantum and κ - the Ginzburg-Landau parameter, whereas λ_{ab}, λ_c are the penetration depths in the (a, b) plane and along the c axis, respectively. However, in the limit of decoupled superlattices this energy contribution vanishes and is therefore not expected in the decoupled superlattices with $n_P = 4$, where at most a weak Josephson coupling is expected. Moreover, U_{Pl} does not depend on the layer thickness d.

There are two possibilities to explain the observed thickness dependence of the activation energy. The first one is that the pinning of vortices is collective. This has been considered by Matsushita et al.[48, 49, 50]. They give the pinning potential for the 2D superconductors with point like pinning centres as

$$U_0 \propto \frac{J_{c0} g^2 d}{\sqrt{B}} \qquad \text{for} \qquad d < L_0 \tag{3.2}$$

where g^2 is the number of flux lines in the flux bundle, L_0 the vortex correlation length and J_{c0} is the (virtual) critical current density in the ideal flux creep free case, which is almost field independent in the low-B domain for small d [48]. The latter formula not only explains the $U_0(B)$ dependence, but also the linear $U_0(d)$ variation, as shown in Fig. 3.8a. However, in this situation a justification for the occurrence of collective (elastic) creep has to be given.

The second possibility would be the consideration of thermally activated dislocation pairs in a $2D$ FLL [14], leading to an activation energy

$$U_0 \propto d \ln\left(a_0/\xi_{ab}\right). \tag{3.3}$$

These dislocation pairs can be considered as either vacancies or interstitials with a finite characteristic energy proportional to d, and are induced by the quenched disorder, as well [47]. Equations 3.2 and 3.3 corroborate the linear $U_0(d)$ variation shown in Fig. 3.8a, as well as the decrease of U_0 with increasing B.

Since the $U_0(B)$ variation offered by Equation 3.2 is not quite different from that supplied by Equation 3.3 [14], in order to decide between the above two models the variation of U_0 with the current I in the specimen was investigated. This is shown in Fig. 3.9 for the superlattice with $n_Y = 20$ and $n_P = 4$. In the considered current domain, no significant heating at the current contacts was detected. Here U_0 was determined in the T interval corresponding to $12 \leq 1000/T \leq 12.25$. An obvious crossover in the $U_0(I)$ variation appears, as illustrated in the inset of Fig. 3.9. For I below ≈ 0.3 mA U_0 is independent of I, indicating thermally assisted flux flow (TAFF). The TAFF regime is possible when the activation energy remains finite in the limit $I \to 0$, as in the case of the (plastic) motion of vacancies and interstitials.

However, for I above ≈ 0.3 mA a significant decrease of U_0 with increasing I is present, which indicates a strong nonlinearity of the current density J dependence of the actual vortex-creep activation energy U. As known, this is expected for elastic (collective) pinning, where $U(J)$ takes the form [51]

$$U(J) = \frac{U_c}{\mu}\left[\left(\frac{J_c}{J}\right)^{\mu} - 1\right] \tag{3.4}$$

Here U_c is a characteristic pinning barrier and $\mu > 0$ is the collective creep exponent [21]. It is worthy to note that Eq. 3.4 accounts for the $U(I)$ decrease at high I from the inset to Fig. 3.9, as well as for the appearance of a downward curvature in the Arrhenius plots from the main panel of Fig. 3.9. In the collective creep regime, for a fixed J both U_c and J_c increase with decreasing T, resulting in a higher local slope in the Arrhenius plot.

A similar crossover from plastic vortex creep at low J to collective creep at high J was observed in magnetization relaxation measurements for various HTS [52, 53] and in the next chapter also, where the induced J decreases with increasing T. The easiest way to understand this crossover is to consider the competition between the thermal energy, the effective pinning energy generated by the quenched disorder E_p, and the elastic energy of the vortex system E_{el}. As known, if the thermal energy is small compared with E_{el} and E_p, when E_{el} overcomes E_p the vortex creep becomes collective [54]. A distinction must be made between the static situation (no transport current) and the dynamic situation (finite current density J in the specimen). In the latter case, the current reduces E_p [which can be roughly described by the actual activation energy $U(J)$ in the vortex creep process]. At the same time, E_{el} is independent of J, and, for a constant T, the current in the specimen will change the relationship between E_p and E_{el}. At high I the elastic energy is dominant, and both vortices

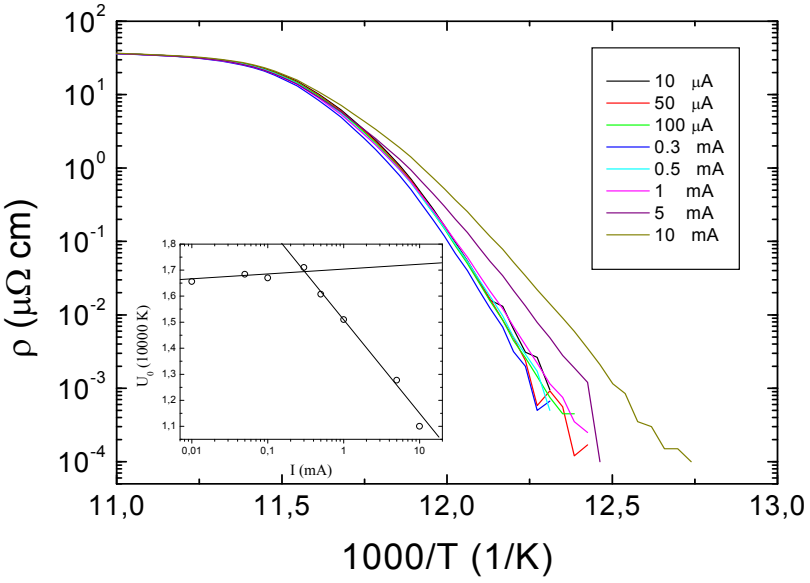

Figure 3.9: Main panel: Arrhenius plots of the resistive transitions of the superlattice with $nY = 20$ and $nP = 4$ for $B = 1$ T and different values of the measuring current I between $10\mu A$ and 10 mA. The inset illustrates the $U_0(I)$ variation, with U_0 extracted from the slope in the Arrhenius plot in the T interval corresponding to $12 \leq 1000/T \leq 12.25$. An obvious crossover in the $U_0(I)$ variation appears. In the low-I domain U_0 is practically independent of I, indicating thermally assisted flux flow (TAFF), whereas for I above$\approx$ 0.3 mA a significant decrease of U_0 with increasing I is present.

and dislocations will be elastically pinned [55]. At low I, the pinning energy overcomes E_{el}, and the vortex creep process will involve plastic motion through vacancies and interstitials.

As known, the magnetization relaxation involves very low magnetoresistivity levels. When $\rho(T)$ is measured with not a very good sensitivity (classically), in order to get a voltage signal one usually increases J toward the actual critical current density J_c where a large amount of vortex creep is present. In this situation, the effective pinning energy (decreasing with increasing J) is low, and the elastic energy (i.e., the vortex-vortex interactions, leading to weak collective pinning) becomes important.

Above we neglected the thermal energy. In the case of superlattices closer

to the 2D case ($n_Y = 1, 2$ for example, where U_0 is small), the 2D vortex fluctuations are predominant, and the proliferation of dislocations (melting) will lead to a large amount of plastic (dislocation mediated) vortex creep, exhibiting clear thermally assisted flux flow behaviour (constant slope in the Arhhenius plots over an extended T interval, Figs. 3.3 to 3.6). Thus a collective creep scenario considering additionally thermal fluctuations can explain the observed magnetotransport behaviour.

3.4 Thickness dependence of the critical temperature

If one examines the resistance vs. temperature curves of superlattices for different layer thicknesses of the YBCO and PBCO layers, one finds that the the critical temperature (T_c) reaches higher values with increase of the thickness of YBCO (or decrease of PBCO thickness) until a saturation value corresponding to a pure YBCO film is reached as shown in Fig. 3.10.

Finally, using superlattices with variable YBCO thickness and fixed PBCO thickness we investigated systematically the correlation length of the vortex system, which was found to be 80 nm along the c axis direction for our samples. Superlattices with fixed thickness of the superconducting layers and variable thickness of the insulating layers were prepared to study coupling of flux-lines across the insulating layer. Even a single PBCO unit cell effectively cuts the flux lines into shorter weakly coupled segments, and the coupling of the vortex systems in neighbouring layers is negligible already for a thickness of four unit cells of the PBCO layers. A characteristic variation of the activation energy for the two series of superlattices was found, where U_0 is proportional to the YBCO thickness [29, 48].

We observed a change in the variation of U_0 with the current I in the specimen: U_0 exhibits a plateau in the low-I region, then decreases significantly with increasing I. This can be explained in terms of a crossover in the vortex creep process, generated by the transport current. At low I values the dislocations mediated (plastic) vortex creep leads to TAFF behavior, whereas at high I the dc transport measurements are dominated by elastic (collective) creep.

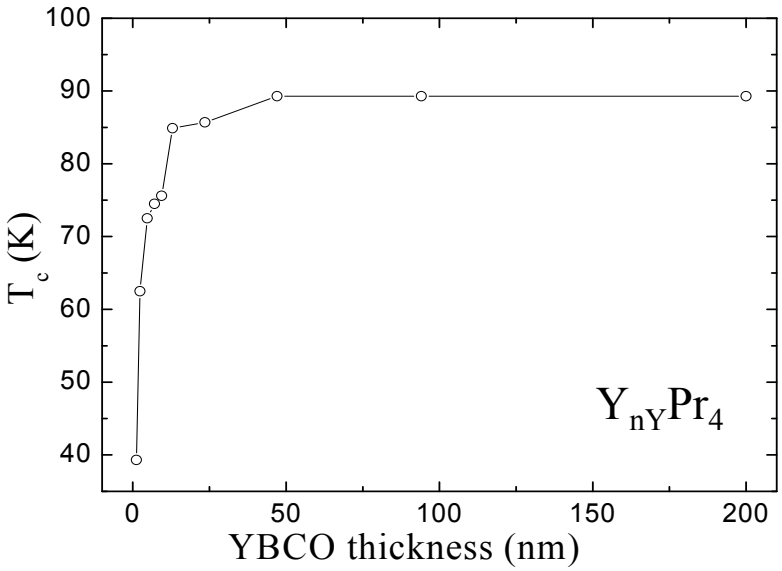

a)

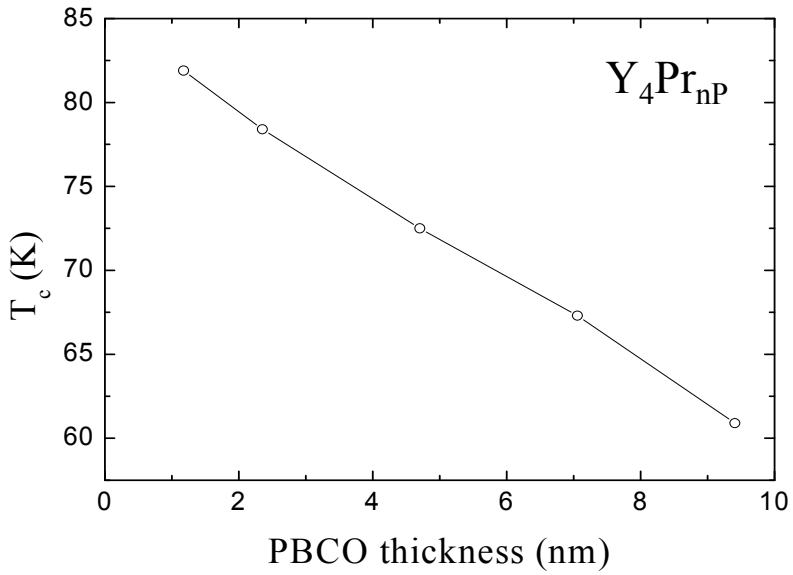

b)

Figure 3.10: The critical temperature of $YBa_2Cu_3O_7/PrBa_2Cu_3O_7$ superlattices with a) $PrBa_2Cu_3O_7$ thickness of four unit cell, as a function of the $YBa_2Cu_3O_7$ thickness. and b) $YBa_2Cu_3O_7$ thickness of four unit cell, as a function of the insulating $PrBa_2Cu_3O_7$ thickness

CHAPTER 4

MAGNETIC RELAXATION MEASUREMENTS

DC magnetization measurements on Y_n/P_4 superlattices

Standard DC magnetization measurements were performed on disk-shaped (radius $R = 2$ mm) $(YBCO)_n/(PBCO)_m$ superlattices (Y_nP_m, where $n = 1$, 2, 4, 11, 20, and $m = 4$), using a commercial Quantum Design Magnetic Property Measurement System, with the external magnetic field H (oriented along the c axis) applied in zero-field cooling conditions. In the considered (H, T) domain the measured diamagnetic moment m was usually identified with the irreversible magnetic moment. The magnetization curves $m(H)$ were registered over a large temperature T interval for H up to 50 kOe, and the relaxation of the magnetic moment $m(t)$ was measured with the superconducting magnet in the persistent mode. The relaxation time t was considered to be zero when magnet charging was finished, and the first data point was taken at $t_1 \approx 100$ s.

We investigated superlattices (with the overall thickness $d = 200$ nm) for which the superconducting $(YBCO)_n$ layers are decoupled by the presence of the $(PBCO)_4$ layer in between. Studying this model system we focused on the determination of the current density J dependence of the vortex-creep activation energy U, which can represent a signature of various vortex phases generated by the presence of relevant quenched disorder in HTS [56, 22, 57] (some of them

with possible zero electrical resistivity in the limit $J \to 0$ at a finite temperature T). Due to thermally activated vortex motion (flux creep), infinite conductivity can only result if the effective pinning barriers diverge at low J, i.e., if the vortex creep exponent is positive. Of particular interest was the possible occurrence of a vortex-creep crossover generated by J, as revealed by the transport measurements discussed in a previous section [58, 37, 59, 60, 61, 62]. In the case of standard DC magnetization measurements J is the density of the macroscopic currents induced in the specimen.

4.1 Magnetically determined superconducting critical temperature T_{c0}

The critical temperature T_{c0} was determined here at the onset of the diamagnetic signal for a field $H = 10$ Oe applied in zero-field cooling conditions, as illustrated in the main panel of Fig. 4.1 in the case of $Y_{11}P_4$. The inset of Fig. 4.1 shows T_{c0} vs. the thickness of the YBCO layers measured in unit cells (n) while $m = 4$. As can be seen, a strong T_{c0} depression occurs for $n \leq 4$, which can be qualitatively explained through the depletion of the superfluid density caused by proximity effects. At the same time, some interdiffusion is not excluded.

4.2 Magnetization curves and the magnetically determined critical current density

Fig. 4.2 illustrates the DC magnetization curves $m(H)$ of Y_4P_4 at various T values between 4 K and 35 K. The hysteresis curves are almost symmetric, which means the influence of surface barriers is negligible. Thus, the magnetization curves allow the determination of a bulk critical current density J_c (affected by thermally activated flux creep) using the Bean model [63, 64]. For our disc-shaped thin film specimens, the Bean relation for practical units is

$$J_c = \frac{3\,|m|}{\pi 10^{-12} d R^3} \tag{4.1}$$

The above relation supplies J_c in A/cm^2 if m is taken in emu, d in $\overset{o}{\text{A}}$ and R in mm. For Y_nP_4 superlattices, where the $(YBCO)_n$ blocks are decoupled, the thickness d (200 nm) must be substituted by an effective thickness

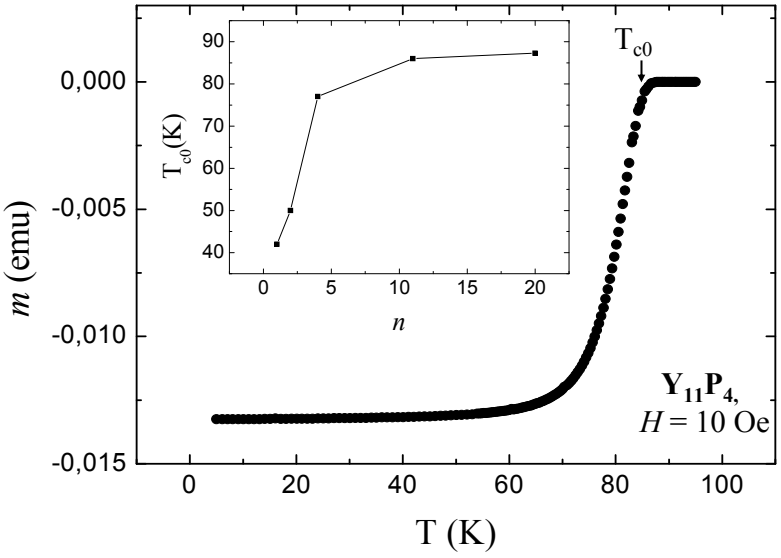

Figure 4.1: Temperature variation of the magnetic moment m for the $Y_{11}P_4$ superlattice in an applied magnetic field $H = 10$ Oe applied in zero-field cooling conditions and oriented along the c axis. The critical temperature T_{c0} corresponds to the onset of the diamagnetic signal. The inset shows the rapid T_{c0} decrease when the thickness of the YBCO layers measured in unit cells (n) decreases below ≈ 4.

$d_{eff} = nd/(n+m)$, corresponding to the volume of the superconducting material $(YBCO)_n$. In the case of $n = 4$, $m = 4$, for example, $d_{eff} = \mathrm{d}/2$.

Fig. 4.2 (main panel) shows the $m(H)$ curves for Y_4P_4 at various T values between 4 K and 35 K. In the inset of Fig. 4.2 we plotted the resulting critical current density J_c determined with Eq. 4.1, where the irreversible magnetic moment was approximated by the measured m in decreasing H. Rigorously, m in Eq. 4.1 is the irreversible magnetic moment, experimentally extracted using the measured m for increasing H, $m(+)$, and decreasing H, $m(-)$, as $m_{irr} = [m(+) - m(-)]/2$. However, when the irreversible magnetic moment of the sample overcomes by orders of magnitude the reversible magnetic moment of the sample (strong vortex pinning) and the magnetic moment of the sample holder (which is the case of our samples over a large (H, T) domain) m_{irr} can be substituted, for simplicity, by $m(-)$. Fig. 4.3 (main panel) is to compare

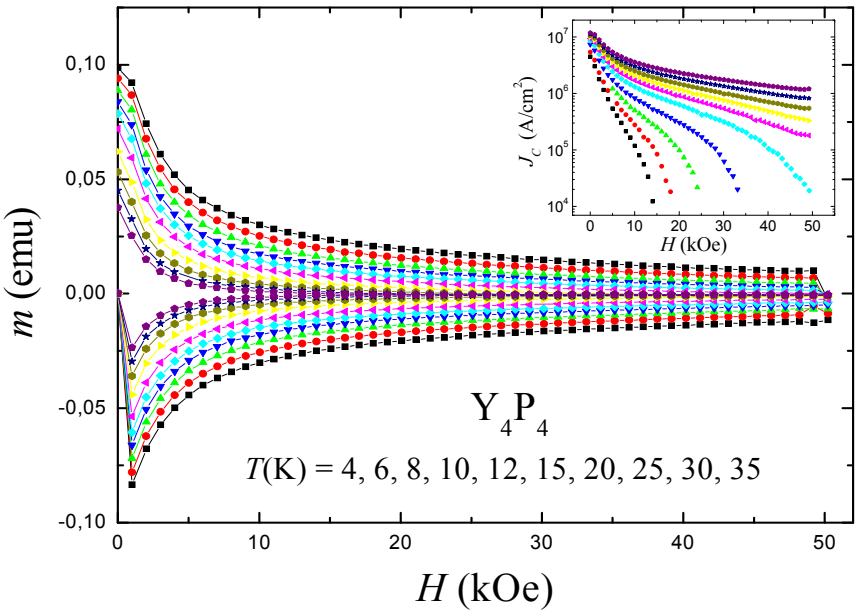

Figure 4.2: Main panel: Magnetic hysteresis curves $m(H)$ for Y_4P_4 at various T values. The inset shows the critical current density J_c determined with Eq. 4.1 where the irreversible magnetic moment m_{irr} was approximated by the measured m in decreasing H.

the $m(H)$ curves of Y_2P_4 and Y_4P_4 registered at $T = 4$ K, whereas the upper inset illustrates the H dependence of the irreversible magnetic moment m_{irr} determined as shown above. In the lower inset the J_c(H) variation obtained with Eq. 4.1 (where $m = m_{irr}$) is plotted. One notes that J_c of Y_2P_4 slightly overcomes J_c of Y_4P_4 at low H, due probably to the influence of the self-field, which is higher for Y_4P_4.

4.3 Magnetization relaxation in Y_nP_4 superlattices

The vortex pinning behavior and the dynamics of vortices are widely investigated using standard magnetization relaxation measurements, with a fixed relaxation time window t_w. As known [65], the vortex pinning energy barrier would easily be extracted from the relaxation of the $m_{irr}(t)$ [approximated in the following by

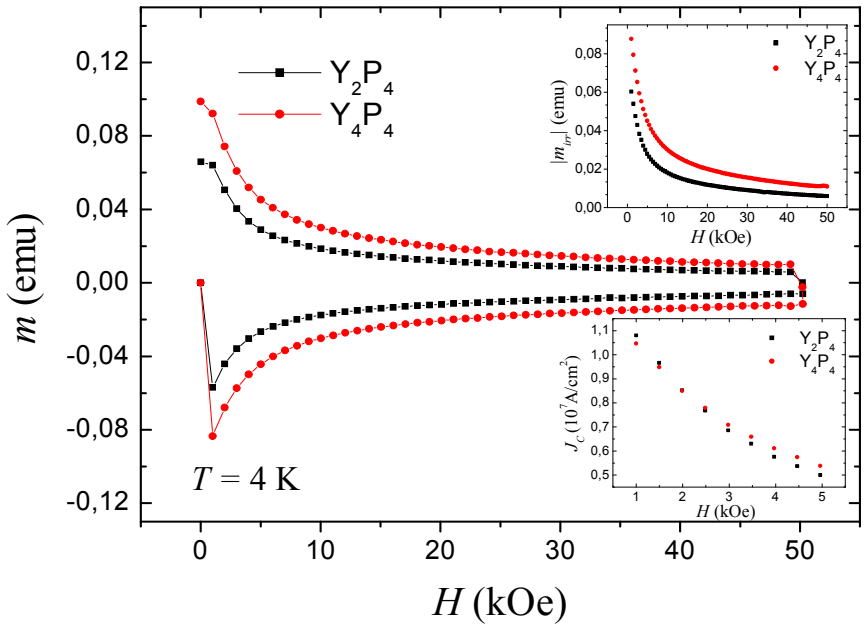

Figure 4.3: Main panel: The m(H) curves at $T = 4$ K for Y_2P_4 and Y_4P_4. The upper inset illustrates the H dependence of the irreversible magnetic moment m_{irr}. In the lower inset the $J_c(H)$ variation resulting from Eq. 4.1 is plotted. At low H, J_c of Y_2P_4 slightly overcomes J_c of Y_4P_4.

the relaxation of the measured magnetic moment $m(t)$], where t is the relaxation time, if the current density J dependence of the vortex-creep activation energy U would be linear (the Kim-Anderson model [15]).

$$U(J) = U_0 \left(1 - \frac{J}{J_{c0}}\right), \tag{4.2}$$

where U_0 is the pinning barrier in static conditions (no current in the sample) and J_{c0} is the true critical current density (in the ideal case of absence of thermally activated vortex creep). The above linear $U(J)$ is equivalent with m decreasing logarithmically in time,

$$m(t) = m(t_0)\left[1 - (T/U_0)\ln\left(t/t_0\right)\right],$$

where t_0 is the time scale for creep [66]. This leads to the determination of U_0 as

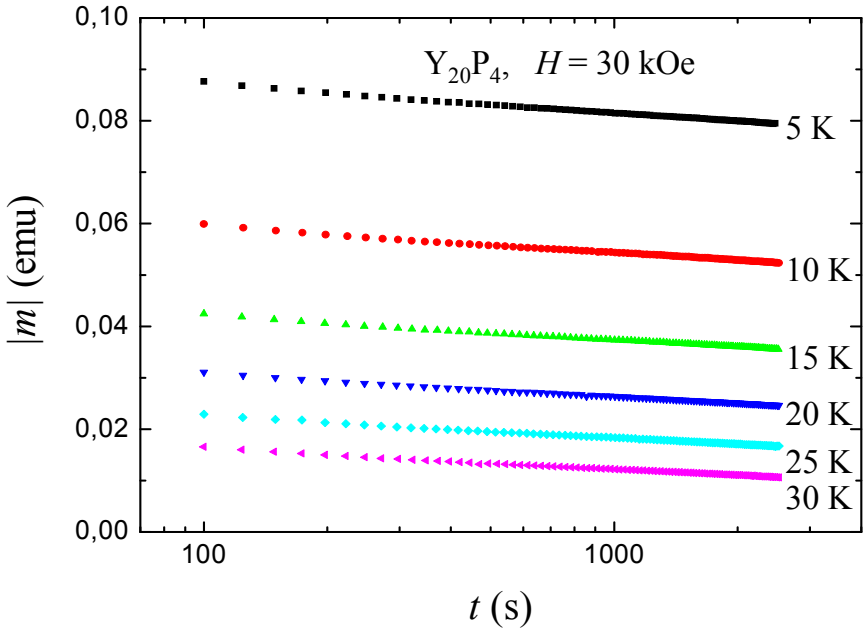

Figure 4.4: Relaxation of the magnetic moment $m(t)$ (logarithmic x-scale) for $Y_{20}P_4$ in $H = 30$ kOe at several T values. In this representation, the magnetization relaxation curves are almost linear for a limited relaxation time window.

$$U_0 = -Tm(t_0)\frac{\Delta \ln(t)}{\Delta m}, \tag{4.3}$$

where t_0 is substituted by a plausible low value ($10^{-12}s - 1s$) [66] and $m(t_0)$ is extracted by extrapolation. Fig. 4.4 illustrates, as an example, $|m|$ vs. $\ln(t)$ for $Y_{20}P_4$, ($H = 30$ kOe). Due to a relatively small overall magnetization relaxation in the relaxation time window $t_w \approx 2500$ s, the plots are almost linear. Thus, it is tempting to consider the linear $U(J)$ from Eq. 4.2 and to determine the pinning barrier U_0 (averaged over t_w) using Eq. 4.3.

Fig. 4.5 shows the T dependence of U_0 obtained with the relaxation curves from Fig. 4.4, by taking $t_0 = 10^{-3}$ s and $|m(t_0)|$ extracted by the linear extrapolation in the representation from Fig. 4.4. As can be seen, U_0 decreases with decreasing T in the low-T range (where the T variation of the superconductor parameters is weak), which indicates that U_0 does not represent the true pinning barrier. This behavior appears for all plausible t_0 values, and can easily be

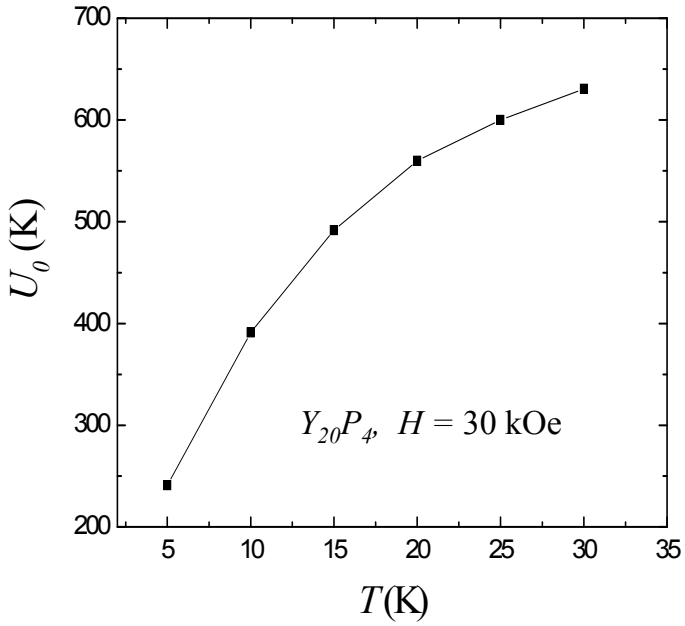

Figure 4.5: T variation of the pinning barrier U_0 determined with Eq. 4.3 using the relaxation data from Fig. 4.4.

explained if a nonlinear $U(J)$ is considered [16], as illustrated in Fig. 4.6., where the graph is drawn for the special condition when $U_c = unit$ and $P = 1$ in the general equation 4.7 in sec. 4.3.1.

In the low-T domain ($T \leq T_{c0}/3$), the main role of the thermal energy is to change the J interval probed in the m relaxation experiment. At low T, the probed J is closer to J_{c0}, due to a reduced overall m relaxation between $t = t_0$ and $t = t_1$, where the first point on m(t) was taken. In this situation, by applying the linear $U(J)$ model the resulting U_0 (see Fig. 4.6) is small. This explains the unphysical result from Fig. 4.5 and indicates that more elaborated analyses are required to obtain information about the vortex pinning energy, as shown below.

4.3.1 The Maley technique

In its original form [67], the Maley scheme refers to the low-T domain, where the T variation of the superconductor parameters is weak, and the main effect of increasing T is to produce monotonically decreasing values of $J \propto |m|$. This allows

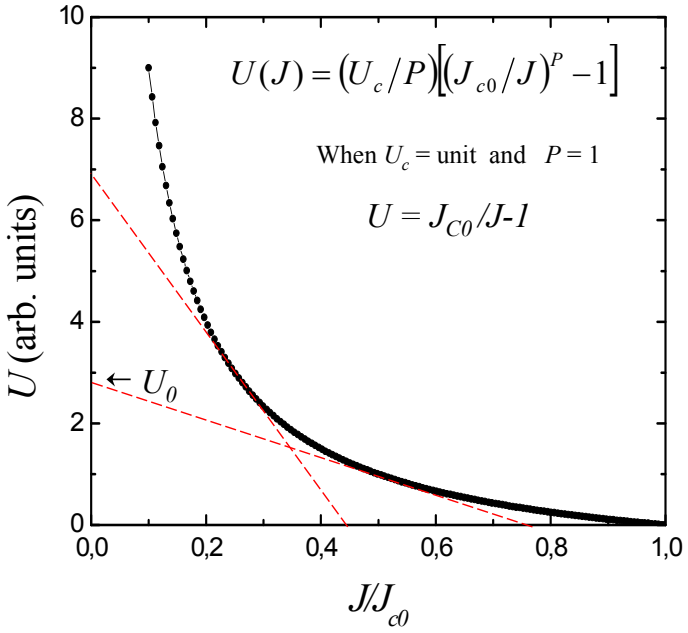

Figure 4.6: A nonlinear $U(J)$ relation leads to U_0 (given by the intercept on the U axis) decreasing with the decreasing of T in the low-T range.

an analysis of the magnetization relaxation data without a *priori* assumptions for the J dependence of U. Briefly, the procedure uses the master rate equation

$$\frac{dm}{dt} \propto \frac{dJ}{dt} = \left(\frac{J_{c0}}{t_0}\right) \exp[-U(J)/T], \tag{4.4}$$

where t_0 is the time scale for vortex creep, as above, which leads to

$$U(J) = -T\left[\ln\left(\frac{dm}{dt}\right) - C\right], \tag{4.5}$$

where C is a T independent constant at low T, uniquely fixed by requiring that U is a continuous function of J. With (dm/dt) and m experimentally determined, one can generate plots of $[-T\ln(dm/dt)]$ vs. $|m|$ at different T. Up to the additive quantity $C\,T$, the plots represent U vs. J.

In this form, the Maley technique can be applied to low-T m(t) data ($T \leq T_{c0}/3$). The technique was extended to the high-T domain, by considering a factor $[1/G(T)]$ accounting for the intrinsic T dependence of U [68]. For a given

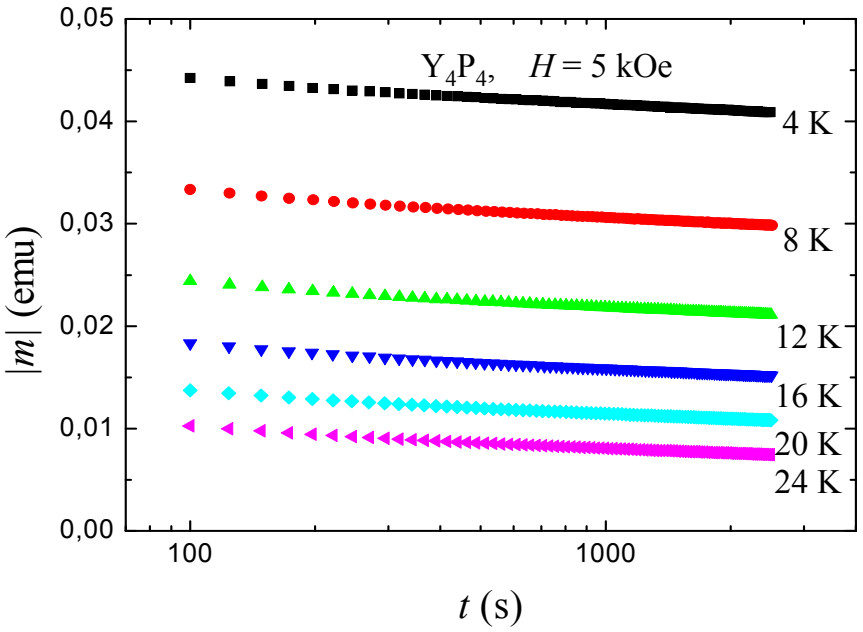

Figure 4.7: Characteristic $m(t)$ curves for the investigated superlattices at various T values.

H, the model dependent $U(J)$ is then represented by $[U(J)/G(T)]$, where $G(T)$ is usually related to the irreversibility temperature T_r [69]

$$G(T) = \left[1 - (T/T_r)^2\right]^{3/2} . \tag{4.6}$$

The procedure was also adapted to field ramping experiments [70]. In these forms, the Maley technique was used for a large variety of HTSC with relevant quenched disorder, such as melt-textured (Y,Pr)BCO [69], thin films [70], detwinned single crystals exhibiting a second magnetization peak [71], YBCO single crystals with columnar defects [72], melt-grown YBCO [73], etc. Below we apply this technique to the $m(t)$ data obtained for various superlattices at $T \leq T_{c0}$, using the simple form (Eq. 4.5).

Fig. 4.7 illustrates characteristic $m(t)$ curves for Y_4P_4 in $H = 5$ kOe at various low-T values. From the experimentally determined $m(t)$ one obtains (dm/dt) and $|m|$, and Fig. 4.8 shows the $U(|m| \propto J)$ dependence constructed with Eq. 4.5. (J can be determined from $|m|$ with the same Bean model, as shown above.) The continuity of $U(J)$ was obtained with the constant $C = 8$

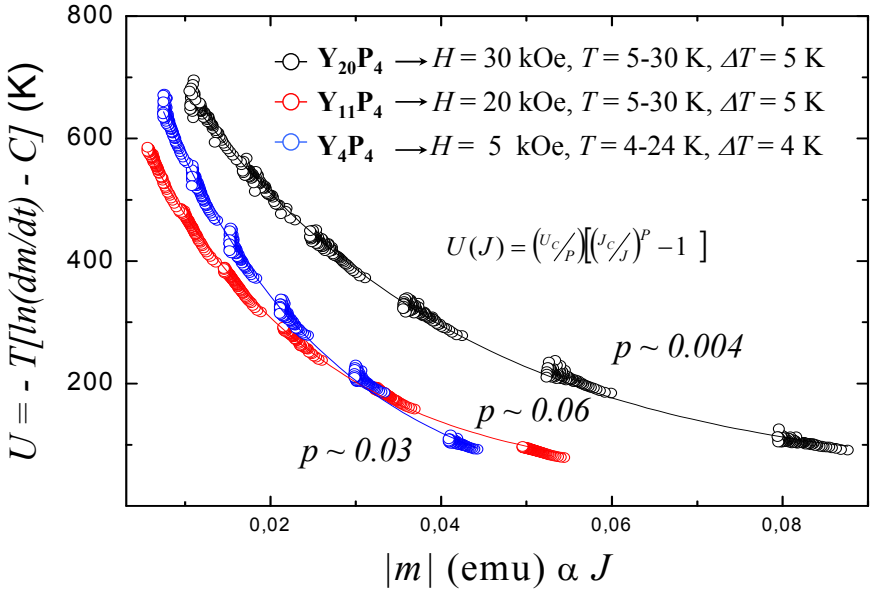

Figure 4.8: The $U(|m| \propto J)$ dependence constructed with Eq. 4.5. The continuous lines represent the fit with the general $U(J)$ relation in Eq. 4.7.

for $Y_{20}P_4$($H = 30$ kOe, $C = 5$ for $Y_{11}P_4$($H = 20$ kOe), and $C = 12$ in the case of Y_4P_4 in $H = 5$ kOe. From the $U(J)$ forms from Fig. 4.8, one can try to obtain the characteristic parameters of the vortex creep process, and in the following the focus is on the creep exponent.

As known, the vortex creep activation energy $U(J)$ can be generally expressed [51] as

$$U(J) = (U_c/p)\,[(J_{c0}/J)^p - 1]\,, \tag{4.7}$$

where U_c is a characteristic pinning energy, J_{c0} is the critical current density for the ideal creep-free case, whereas the creep exponent p is identified with the (positive) collective pinning exponent μ of the order unity in the case of elastic (collective) vortex creep [21], and $p < 0$ for plastic creep. The value $p = 1$ corresponds to the classic Kim-Anderson model [15], whereas a value $p = -0.5$ often appears [74].

As can be seen in Fig. 4.8, the constructed $U(J)$ variation can be fitted with Eq. 4.7 with plausible U_c and J_{c0} values, but the problem is that the resulting

collective creep exponent is unreasonably low. The lowest μ value supplied by the collective pinning theory [21] is 1/7, and should appear at small H, in the isolated vortex limit. For the H values from Fig. 4.8 and by considering the aspect ratio of the samples the collective creep exponent should be of the order unity (even in the $2D$ case).

The above discrepancy raises some questions concerning the sensitivity of the Maley technique in the case of significant pinning and a usually limited t_w. Another more straightforward analysis for the determination of the vortex creep parameters using the same $m(t)$ data is presented in the following.

4.3.2 The normalized vortex-creep activation energy

The same standard $m(t)$ data can be analyzed by determining the so called normalized vortex-creep activation energy $U^* = -T\,(d\ln(t)/d\ln(m))$. This quantity was introduced [65] with the aim to reduce the intrinsic ambiguity of flux creep experiments, and it was thought that it represents an "effective pinning energy". However, the determined T variation of U^* at low T exhibits a decrease of U^* with decreasing T, similar to that from Fig. 4.5. The meaning of U^* can be found as follows [53]. With Eq. 4.7 and considering $J \propto |m|$ as explicit variable, one can derive

$$U^*(J) = -T\left(\frac{d\ln(t)}{d\ln(|m|)}\right), \tag{4.8}$$

using the general creep relation [75] $U = T\ln(t/t_0)$. Assuming a small change of t_0, for the elastic-creep domain (collective creep) one obtains

$$U^*(J) = U_{ce}\,(J_{c0}/J)^{\mu} \tag{4.9}$$

In the plastic creep regime U^* has an opposite variation with J,

$$U^*(J) = U_{cp}\,(J_{c0}/J)^{p} \tag{4.10}$$

Since for collective creep the pinning centers do not accommodate vortices, the characteristic pinning energy for elastic creep U_{ce} can be much lower than the characteristic pinning energy for plastic creep U_{cp}.

With a fixed t_w and taking now T as explicit variable, for T well below T_{c0} the above equations lead to

$$U^*(T) \approx U_{ce} + \mu T\ln\left(t_w/t_0\right), \tag{4.11}$$

for elastic creep, and

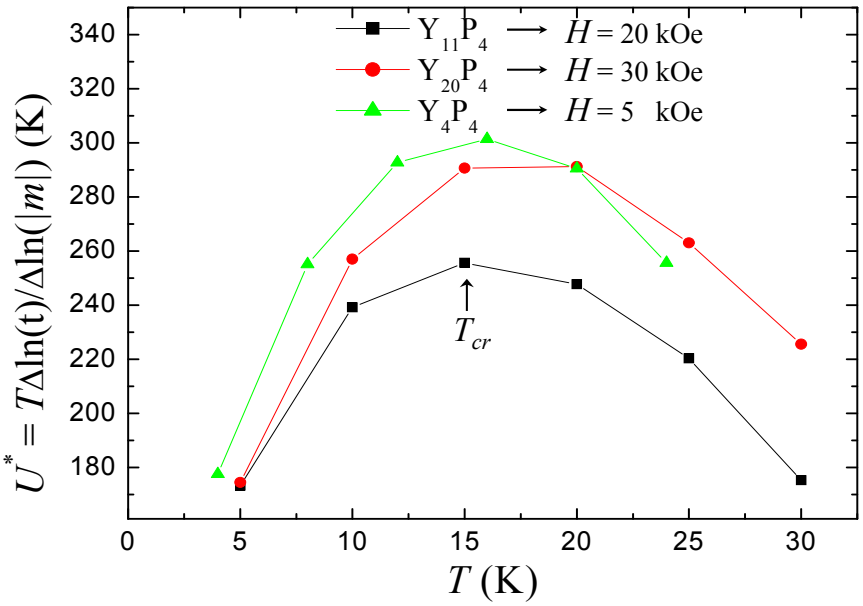

Figure 4.9: U^* averaged over t_w vs.T, where U^* was determined with the $m(t)$ data used to construct $U(J)$ in Fig. 4.8. $U^*(T)$ exhibits a maximum, at a crossover temperature T_{cr} indicated by an arrow.

$$U^*(T) \approx U_{cp} - |p|\, T \ln\left(t_w/t_0\right), \tag{4.12}$$

in the case of plastic creep. [For simplicity, the same t_0 for elastic and plastic creep is considered.]

As shown in Fig. 4.7, the $m(t)$ data in a log-log plot are almost linear for a relatively reduced t_w. In this situation, one can determine a U^* value averaged over t_w, as $U^* = -T\Delta\ln(t)/\Delta\ln(|m|)$, and Fig. 4.9 illustrates $U^*(T)$ for various superlattices and H values. The notable aspect is the appearance of a maximum in $U^*(T)$, which, according to Eqs. 4.11 and 4.12, suggests the existence of a crossover in the vortex system at a crossover temperature T_{cr}: elastic (collective) creep at low T - plastic creep at high T.

The U^*(T) maximum has been reported for HTS with weak quenched disorder, such as $Tl_2Ba_2CaCu_2O_{8+\delta}$ thin films [76], $Bi_2Sr_2CaCu_2O_{8+\delta}$ single crystals [52], and high-quality YBCO films with a smaller J_{c0} obtained by high-pressure dc sputtering [53], as well as for YBCO films obtained by PLD, where

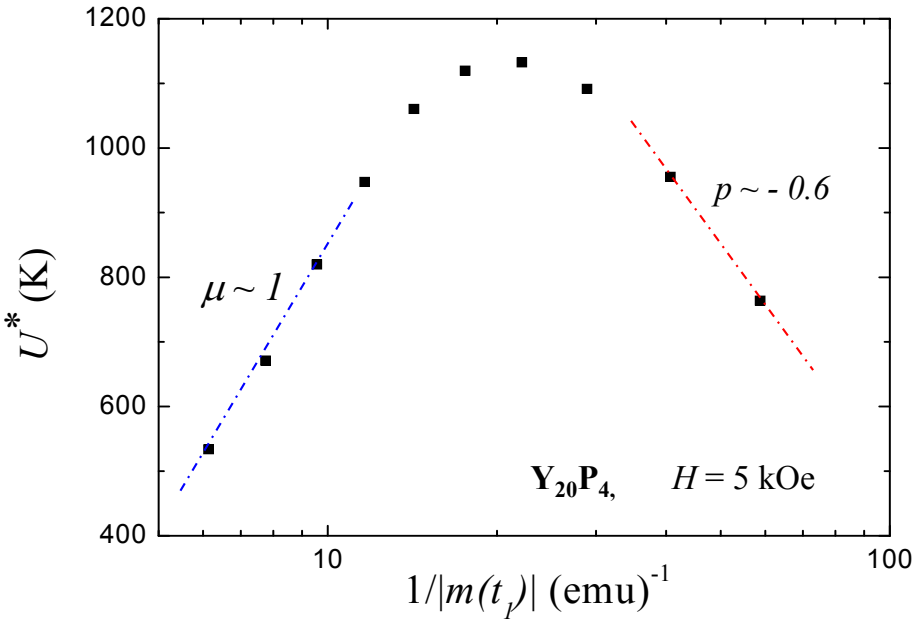

Figure 4.10: U^* averaged over t_w vs. $1/|m(t_1)| \propto 1/J(t_1)$ for $Y_{20}P_4$ at $H = 5$ kOe, which allows the extraction of the elastic creep exponents μ and p.

strong vortex pinning on growth induced linear defects is present [77]. The difference is that in the latter case T_{cr} is significantly higher. Plotting U^* vs. $[1/|m(t_1)|] \propto 1/J(t_1)$ and using Eqs. 4.9 and 4.10 one can determine the creep exponents μ and p, as can be seen in Fig. 4.10. The collective creep exponent $\mu \approx 1$ is in the range offered by the collective creep theory [21], whereas the plastic creep exponent p is not far from the value -0.5 [74], which may indicate that the vortex motion at high T is similar to that of atoms in solids, through dislocations. The slightly higher p (in absolute value) obtained here is probably due to the fact that at high T the influence of thermal fluctuations is important.

In the approximation $t_0 =$ constant, Eqs. 4.11 and 4.12 give the creep crossover temperature.

$$T_{cr} = (U_{cp} - U_{ce}) / (\mu + |p|) (\ln (t_w/t_0)) \tag{4.13}$$

A simple way to understand the creep crossover appearing in standard magnetization measurements is to consider the energy balance relation [78] for dynamic conditions [53] (finite J).

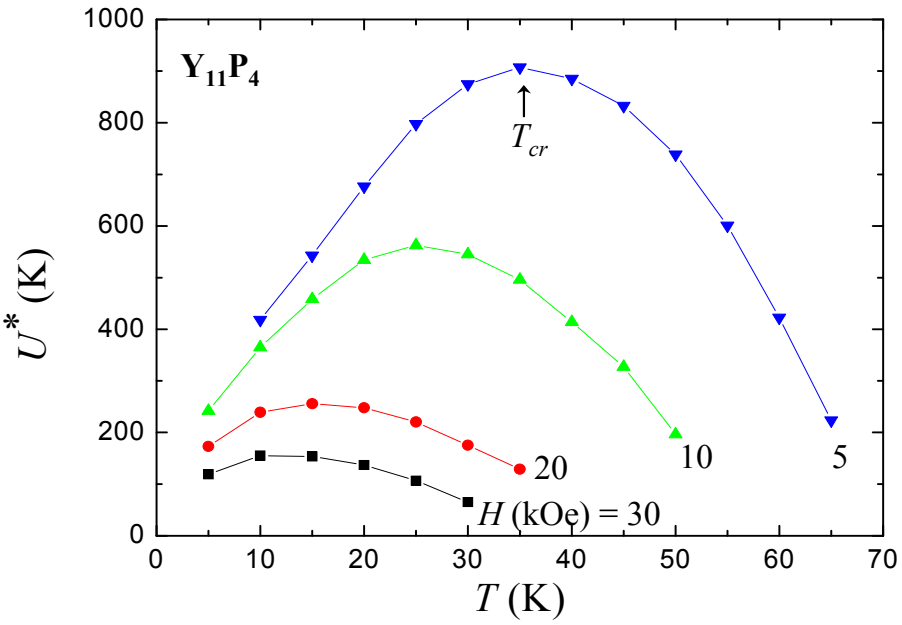

Figure 4.11: U^* vs. T for $Y_{11}P_4$ at different H. The crossover temperature T_{cr} decreases with increasing H.

As noted above (see Fig. 4.6), at least for T well below T_{c0} the main role of the thermal energy is to change the probed J interval relative to J_{c0}. At low T, due to a reduced overall relaxation between t_0 and t_1, the probed J [$\propto |m(t)|$] is closer to the true J_{c0}. Consequently, the effective pinning energy E_p (decreasing with increasing $J/J_{c0)}$ can be lower than the elastic energy in the vortex system E_{el} (independent of J), and the creep will be elastic, regardless of the fact that vortex pinning in static conditions ($J = 0$) is weak or strong (like in thin films). At high T, J is much lower than the true J_{c0}, and E_p becomes higher than E_{el}. In these conditions dislocations proliferate, the pinning centers accommodate vortices, and one expects vortex creep in a plastically pinned vortex assembly at low driving currents (J).

In a crude approximation, one can consider $E_p = E_{el}$ at $T = T_{cr}$, and $E_p \propto U$. Using the general vortex-creep relation and $E_{el} \propto H^{-1/2}$, for a fixed t_w it results $T_{cr} \propto H^{-1/2}$. This relation was proven for YBCO films having the thickness larger than the vortex correlation length along the c axis [53]. As can be seen in Fig. 4.12, where we plotted $H(T_{cr})$ [with T_{cr} resulting from the $U^*(T)$ data

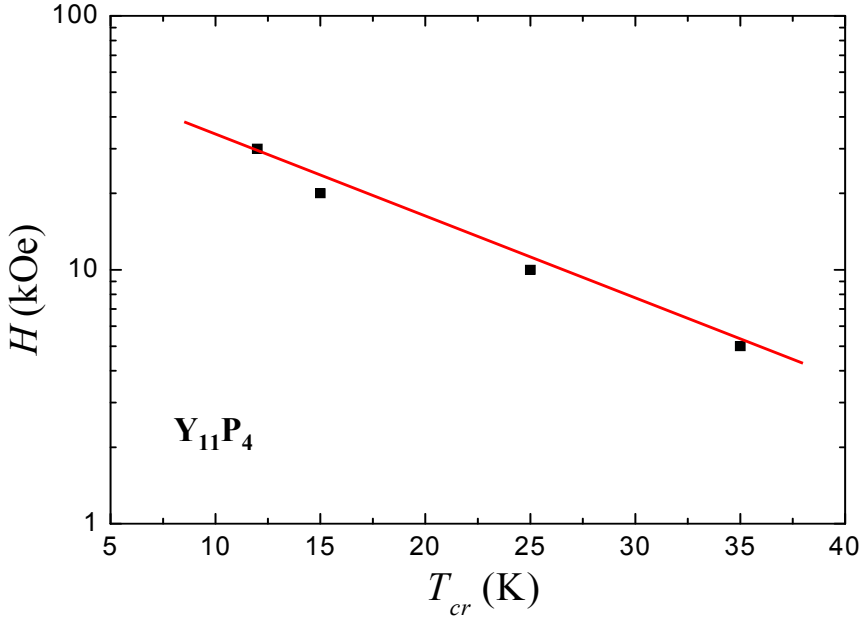

Figure 4.12: The creep crossover in the (H, T) diagram, obtained by plotting T_{cr} from Fig. 4.11 vs. H. The creep crossover line is close to T_{cr} decreasing linearly with increasing $\ln(H)$.

for $Y_{11}P_4$ from Fig. 4.11], a better relation describing the creep crossover line in the (H, T) plane would be T_{cr} decreasing linearly with increasing $\ln(B)$. Such a relation results by taking into account that when the thickness of the superconducting layer (n unit cells) is lower that the vortex correlation length along the c the creation of dislocation pairs is representative for the plastic deformation of the vortex system, and the energy of a dislocation pair is $\propto n \ \ln(H)$ [62], and it will substitute E_{el} in the above discussion.

Finally, we discuss the effective thickness dependence of the creep crossover temperature observed for our Y_nP_4 superlattices (decoupled Y_n superconducting blocks). Fig. 4.13 (main panel) illustrates the U^*(T) maximum for several superlattices ($H = 10$ kOe). Here the $U^*(T)$ variation is included for a 200 nm thick film ($n = 170$ unit cells) obtained in the same sputtering conditions. As shown in the inset, in the case of superlattices T_{cr} increases roughly linearly with the effective thickness (measured in cell units, n). This is in agreement with Eq. 4.13,

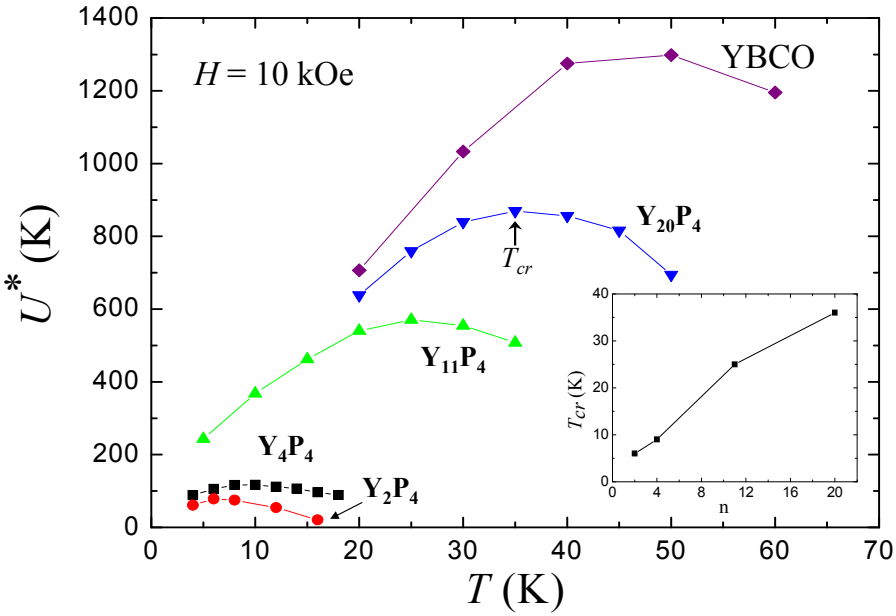

Figure 4.13: Main panel: U^* vs. T for different superlattices in $H = 10$ kOe, where the $U^*(T)$ data is included for a 200 nm thick YBCO film prepared in the same conditions. As shown in the inset, T_{cr} is roughly proportional to the thickness of the superconducting YBCO block measured in unit cells (n).

since both the plastic barriers [62, 14] and the collective pinning barriers [48] are proportional to the effective superconducting layer thickness, when the latter is smaller than the vortex correlation length along the H direction, which is the case for the considered superlattices. By taking into account the T_{cr} value for the YBCO film (≈ 45 K), it can be concluded that $T_{cr}(n)$ should saturate at large effective thicknesses. This happens when the effective thickness overcomes the vortex correlation length, as discussed in the previous chapter.

CHAPTER 5

OUT-OF-PLANE TRANSPORT IN SUPERLATTICES

Introduction

There are several main motivations behind the effort which is taken in the growth and the study of high-T_c multilayer structures. There is a technological need for heterostructures containing superconductors and insulating (or metallic) layers, for instance in the fabrication of Josephson effect junctions. Tunneling experiments in a classical superconductors play an important role in testing the local superconducting density of states [79]. However tunneling experiments are extremely sensitive to the quality of barriers and interfaces. Artificial $YBa_2Cu_3O_7/PrBa_2Cu_3O_7$ superlattices are considered as one possibility to realize tunneling junctions. In this case it is possible to modify the tunneling properties for investigation of c-axis tunneling in $YBa_2Cu_3O_7/PrBa_2Cu_3O_7$ superlattices (YBCO/PBCO) by varying the periodicities of the YBCO or PBCO layers. For this purpose high-pressure dc sputtering has been used to prepare series of 200 nm thick YBCO/PBCO superlattices. The high quality of the samples was checked by detecting up to third order satellite peaks in x-ray diffraction.

In this chapter the c-axis transport in $YBa_2Cu_3O_7/PrBa_2Cu_3O_7$ superlattices is investigated by two different methods. The first one uses mesa structures prepared with a lithography process using 200 nm thick $YBa_2Cu_3O_7/PrBa_2Cu_3O_7$

Table 5.1: Layer arrangement of thin film structures used for patterning of mesas or FIB patterned bridges.

Layers	Mesa	FIB-Bridge
Sustrate	$SrTiO_3$	$SrTiO_3$
PBCO	—	700nm
First YBCO	150 nm	300nm
Y/P superlattice	200 nm	$1\mu m$
Number of repetitions	17 times	86 times
Second YBCO	50 nm	400 nm
Gold layer	200 nm	50 nm
Total thickness	600 nm	$2.45\mu m$

superlattices. The other uses 1 μm $YBa_2Cu_3O_7/PrBa_2Cu_3O_7$ thick superlattices embedded in pure YBCO layers (thick bridge). Here a comparatively thick bridge is prepatterned photolithography and the final patterning step uses a focused ion beam (FIB). This allows patterning on a submicron scale. In both of these cases, the current J will pass vertically through the $YBa_2Cu_3O_7/PrBa_2Cu_3O_7$ superlattice (and the Copper Oxide planes). Table 5.1 shows the comparison between these layer arrangements.

5.1 C-axis transport in mesa structures.

5.1.1 Temperature dependence of the resistivity

The temperature dependence of the resistances $R(T)$ in the direction of the c-axis of heterojunctions was investigated using mesa structures with different areas. In Fig. 5.1 a semi-logarithmic plot of the c-axis resistances is shown for four mesas with 50×50, 40×40, 30×30 and 16×16 μm^2 area, respectively. All were prepared from the same $YBa_2Cu_3O_7/PrBa_2Cu_3O_7$ superlattice which contained a periodic sequence of 2 layers $YBa_2Cu_3O_7$ and 7 layers $PrBa_2Cu_3O_7$ (2:7). The transition observed at 88.5 K corresponds to the superconducting transition T_c of $YBa_2Cu_3O_7$ layers. A reduced T_c typical for the non-fully developed order parameter in the 2 unit cell thick $YBa_2Cu_3O_7$ layer [80] would have been expected. Above T_c, the larger mesas show a temperature dependence that is similar to the (ab)-plane measurement.

In Fig. 5.2 the resistances of four mesas with 50×50, 40×40, 30×30 and $16\times$

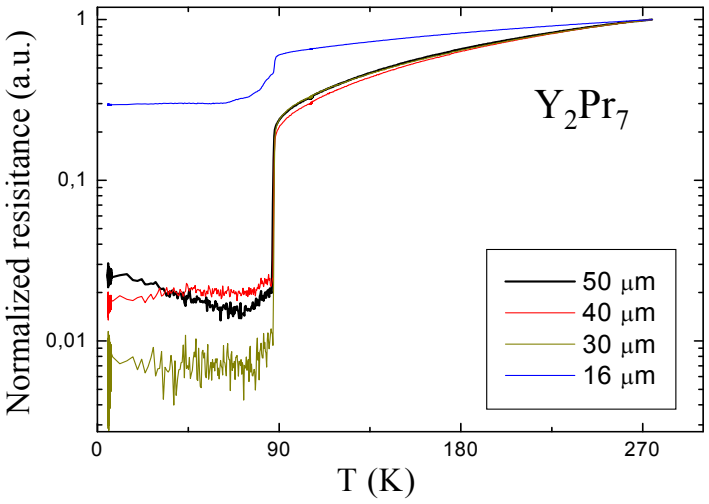

Figure 5.1: Resistance as function of temperature for 50×50, 40×40, 30×30 and 16×16 μm^2 mesas patterned on a 2:7 YBCO/PBCO superlattice. The four measurements are normalized to the resistance at 274 K and presented with a logarithmic y-axis.

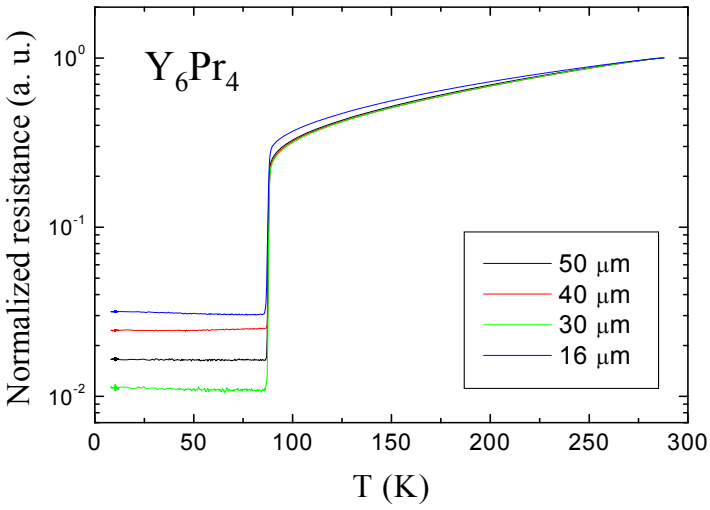

Figure 5.2: Resistance as function of temperature for 50×50, 40×40, 30×30 and 16×16 μm^2 mesas patterned on a $(YBa_2Cu_3O_7)_6/(PrBa_2Cu_3O_7)_4$ superlattice. The four measurements are normalized to the resistance at 274 K and presented with a logarithmic y-axis.

16 μm^2 area are shown. They contain as active structure a superlattice with 6 layers $YBa_2Cu_3O_7$ and 4 layers $PrBa_2Cu_3O_7$ (6:4). The transition temperature T_c observed at 88.5 K has the same value as the mesas based Y_2/P_7 superlattice. This result is not expected. So, let us try to understand what happened? X-ray diffraction for these superlattices proved that they were epitaxially grown with a high quality. The modulation length of multilayer structure was checked by SUPREX program, which indicated that the superlattice structure had a well modulated structure. Such the first step was successful.

However the problem persisted. For many attempts to measure different superlattices with different mesa dimension, all of the resistance-teperature curves had the same transition temperature T_c. To solve this problem, I suppose three reasons:

- This may be due to bad photoresist.
- Surface morphology, because pinholes can influence the junction behavior in the sense of a shunt resistance.
- Too low c-axis resistivity of the fully oxygenated PBCO layers.

To check for the first reason Y_6/P_4 superlattice mesas were prepared. Here on the mesas with 50×50 and $16 \times 16 \mu m^2$ the photoresist was not opened on the top of mesa, and in the same film the other mesa structures with 50×50 and $30 \times 30 \mu m^2$ were processed normally with a contacting window on top of the mesa. As in Fig. 5.3 the resistance-temperature curve shows that no superconducting transition for the fist two closed mesa structures with 50×50 and $16 \times 16 \mu m^2$ exists. For the two others (50×50 and $30 \times 30 \mu m^2$ mesas) again a T_c of 88.5 K is observed. This confirms that the photoresist is a good isolator.

Thus the two other possibilities remain. Surface morphology investigations showed severe roughness. Usually that is resulting from CuO_2 crystallites, which are insulating aid therefore not disturbing the transport measurements. However, *a*-axis oriented grains could shunt the mesa structure. Also the resisitivity of the PBCO layers depends strongly on the oxygen concentration. The geometry of the mesa measurement is only a three contact geometry. If the resistance of the PBCO interlayers is too low, the transition might be masked by the contact resistance and one only would effectively see the transport in the *ab* plane. Working on theses problems would require smoother films and/or different targets e.g. Ga doped PBCO. In both cases extensive optimization of film deposition parameters would be needed. Therefore a different method was tried as described in the following.

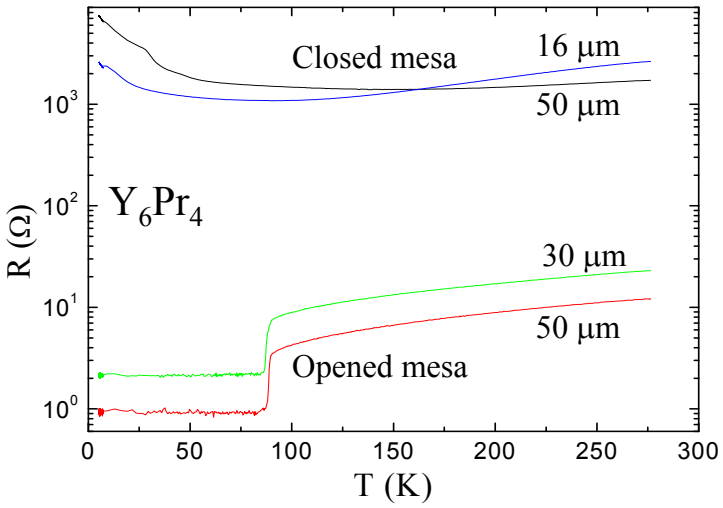

Figure 5.3: Temperature dependence of the c-axis resistivities of 50×50 and 30×30 μm^2 mesas patterned on a $(YBa_2Cu_3O_7)_6/(PrBa_2Cu_3O_7)_4$ superlattice with opened mesa (bottom), and 50×50 and 16×16 μm^2 with closed mesa (top).

5.2 Transport in FIB cut structures

As possibly the resistivity of the PBCO interlayers is not high, the area of the mesas should be reduced in order to increase the c-axis resistance contribution. This will also allow to reduce the total current or to increase the current density while reducing heating at the contacts. With the available photolithography equipment this reduction would be extremely difficult or impossible. Therefore a combined technique was used. The films are patterned photolithography to define a $10\mu m$ wide track with four contacts. In cooperation with the group of Prof. M. Huth in Frankfurt a focused ion beam (FIB) system could be used in order to narrow a portion of the track to $1\mu m$. Then lateral cuts force the current to flow vertically through the $YBa_2Cu_3O_7/PrBa_2Cu_3O_7$ superlattices, as shown in fig. 5.4. Actually the cuts are under 60^0 to the surface normal and one is made from top. The other is a rectangular hole that is 'drilled' from the other side at the substrate film interface. The geometry of this hole is chosen in a way that the film surface is undamaged leaving a current path through the YBCO cover layer intact.

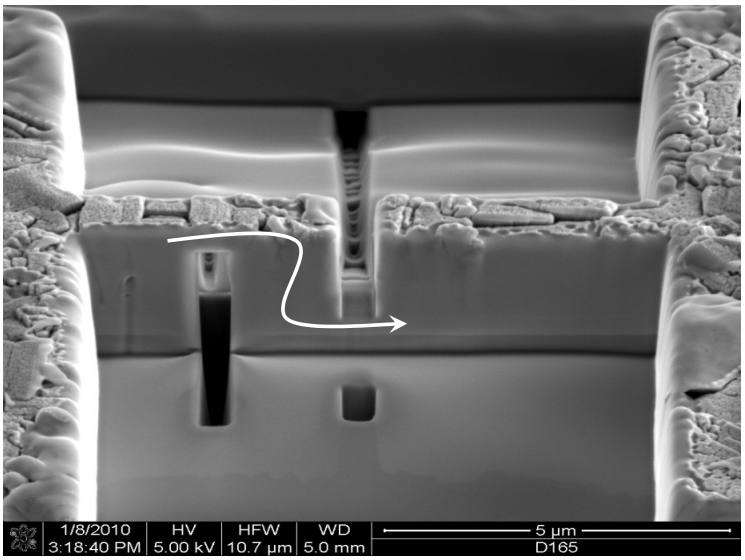

a)

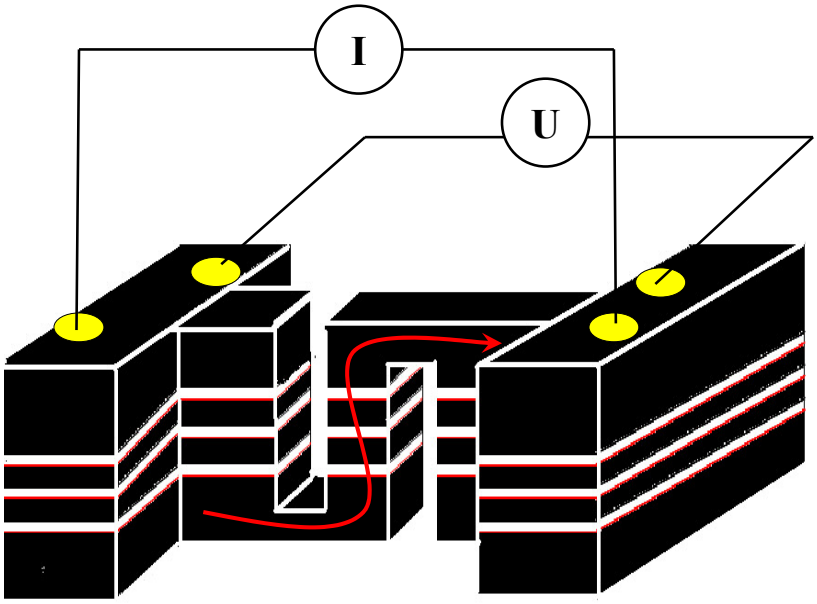

b)

Figure 5.4: Lateral cuts for a $YBa_2Cu_3O_7/PrBa_2Cu_3O_7$ thick superlattice by a) Focused-ion beam (FIB) with area dimensions $1 \times 1\mu m^2$. b) Schematic diagram of lateral cuts, where the current J flows vertically through the $YBa_2Cu_3O_7/PrBa_2Cu_3O_7$ superlattice layer

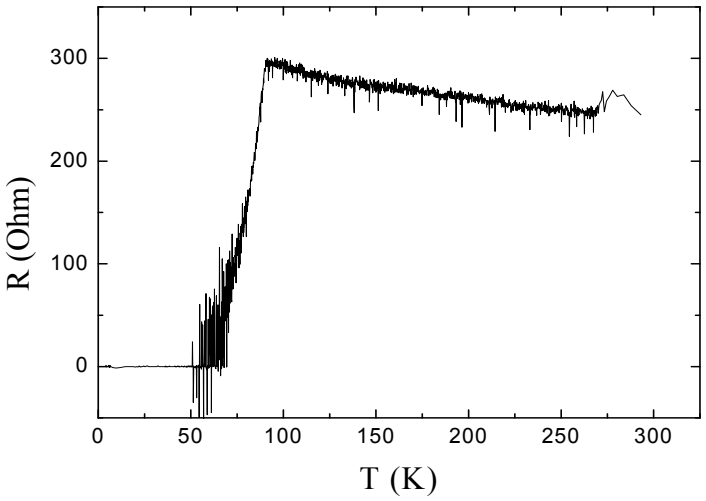

Figure 5.5: Temperature dependence of the c-axis resistance of a nanostructure of area dimension $1 \times 1\ \mu m^2$ cut into Y6P4 superlattice.

5.2.1 Temperature dependence of the resistance

A measurement of the temperature dependence of the resistance in the direction of the c-axis as a function of temperature for a FIB cut nanostructure ($1 \times 1\,\mu m^2$) of a Y6P4 superlattice is shown in Fig. 5.5. In contrast to the photolithographically patterned mesa structures here the resistivity in the normal state is decreasing with increasing temperature as is expected for transport in PBCO. Also the total resistance is more than one order of magnitude higher than for the photolithographically patterned opened mesa structures. As the superlattice is much thicker than in the previous case in-plane contributions will be reduced and the enhancement is from the out-of-plane contributions. The normal state resistance of the PBCO layers in the mesa structures can be estimated to be larger than 12Ω (using the thickness of the PBCO layers 400nm and ρ_{ab}(PBCO)=3mΩcm [31]). The anisotropy of the resistivity ρ_c/ρ_{ab} will be larger than one. However, it is expected to depend strongly on the oxygen content and is therfore not a well established quantity. Nevertheless it seems clear that a c-axis contribution should be visible in Fig. 5.5. A superconducting onset starts at T_c=87 K, which, however, is broadened compared to the in-plane measured transitions. The resistance measurements cannot decide whether this broadening is induced by a finite Josephson-coupling between the PBCO layers or by an Ion-Beam induced damge in the FIB cut structure or by an oxygen loss at

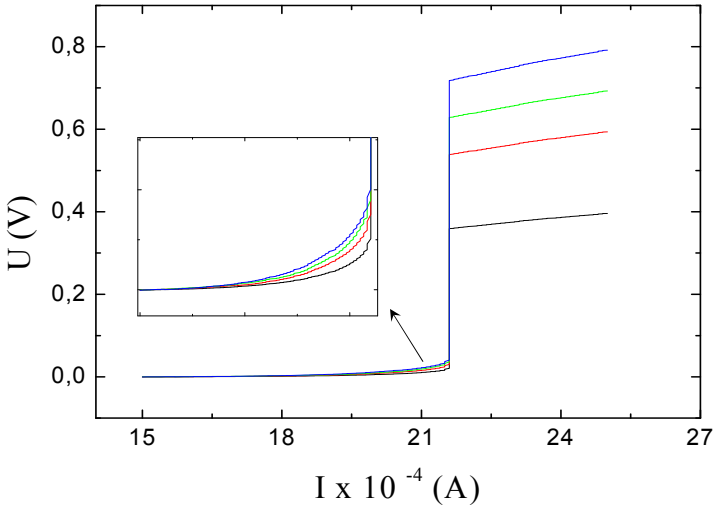

Figure 5.6: IU-curve measured four times at 55 K in zero field for $1 \times 1\ \mu m^2$ FIB patterned nanostructure in a $(YBa_2Cu_3O_7)_6/(PrBa_2Cu_3O_7)_4$ superlattice.

the surface layer of the superconductures visible due to the strongly enhanced surface to volume ratio of the nanostructure.

5.2.2 Current-voltage-curves

If the c-axis transport is dominated by Josephson currents the critical current of these junctions could be visible in the current-voltage curves. Ideally this critical current would be modulated by the magnetic field applied parallel to the layer structure. The first derivative of the current-voltage curves should show anomalies at the superconducting gap for tunneling charge carriers. Therefore current-voltage curves were taken. Current voltage curves for a FIB patterned structure are shown in Fig. 5.6. While on a first look it seems a critical current is detectable, one must note that neither features in the derivative of the IU curve could be detected at lower voltage levels (not shown), nor an influence of the magnetic field. Unfortuntately the jump in the IU curve at high voltage levels is most probably caused by overheating. The residual resistance visible at 'low' currents in the inset of Fig. 5.6 leads to a dissipation of typically several μW before a jump appears. For the volume of the FIB structure of the order of $(1\mu m)^3$ this is a huge power density. For currents of 2mA the current density is already of the order of $2 \cdot 10^5$ A/cm^2, well above the expected Josephson critical currents.

Also the resistance before the jump is found to be of the order of 10Ω. Thus the actual FIB structure must already be normal conducting before the jump occurs. The dissipated heat, however, will be transported away by the large width layers leading to the nanostructure. The connecting structures are epitaxially grown on the substrate and are effectively cooled by the substrate in contrast to the FIB cut nanostructure. A current above a threshold current will lead to a thermal runaway if the actual temperature of the connecting layers becomes higher than the critical temperature, since then not only the nanostructure will be normal conducting, but large parts of the thin film. The four curves in Fig. 5.6 correspond to four measurements at nominally the same temperature. However, one must note that in the variable temperature insert used, the temperature of a helium gas flow is controlled, while the helium gas pressure and thus the cooling power is not controlled. Therefore the differences in the resistivity visible in the dissipation levels before the jump are most probably related to the fact that the size of the regions driven to a normal state are different in these repetitions. The differences after the jump are related to different voltage limits set for the current source, which prevent an unlimited heating.

In summary the experiments on the out-of-plane transport in the superlattice structure could not yield a direct proof of Josephson coupling between the neighbouring YBCO layers in the investigated YP superlattices. It could be verified that the photolithography steps were not responsible for these failure and the insulating behavior of the photoresist was sufficient. One can speculate that the PBCO layers had a too high conductivity and Ga doped PBCO layers with lower conductance would have been the better choice. These had been used in previous experiments [32, 81]. However, in these preceeding experiments the quality of the insulating photoresist layer was questionable. Future work should combine the use of Ga doped PBCO in superlattices with the patterning steps developed and improved in this work.

CHAPTER 6

A-AXIS ORIENTED $YBA_2CU_3O_7$ FILMS

In this chapter, I present a systematic investigation of the structural, microstructural and T_c evolution of a-axis into c-axis orientation in $YBa_2Cu_3O_7$ (YBCO) thin films on (001) $SrTiO_3$ with the enhancement of growth temperature from 610 to 825^0C using short post-annealing at 825^0C or two temperature template growth followed by post annealing. Post-annealing or template approach produced different results. This suggests that a complex optimization approach must be followed in order to achieve a higher quality of the films. While c-axis as grown thin film have shown high quality ($T_c = 89.5$ K), the best a-axis thin film was obtained after post-annealing of the film grown at 650^0C ($T_c = 74$ K). The two temperature template growth followed by post-annealing was overall less efficient than post-annealing only. At intermediate temperatures of $630 - 690^0$C some whiskers-like grains with triangular tips and being perpendicular to the substrate were observed.

6.1 Introduction

High temperature cuprate superconductors (HTCS) such as $YBa_2Cu_3O_7$ are layered highly anisotropic materials. For YBCO the coherence length in the ab-plane (ξ_{ab}) is about 1-2 nm, while in the c-axis direction (ξ_c) it is significantly shorter (about 0.03 nm). One the one hand, this situation is useful for electron-

ics applications of HTCS, but, on the other hand, it raises significant challenges in the device fabrication and integration. One immediate idea for the device fabrication is to stack in the c-axis direction alternating layers of the superconductor and of an insulator to produce artificial tunneling SIS (superconductor-insulating-superconductor) Josephson junctions. Growth of top quality individual c-axis HTCS thin films was performed by many groups [1] and the next step of SIS c-axis heterostructures growth may look straightforward. Despite this positive fact, success rate of demonstrating Josephson junctions on SIS c-axis heterostructures is rather low [2]. Among the reasons is that the very short ξ_c imposes serious requirements on the flatness of the surfaces, on inter diffusion problems and, not least, on the thickness of the insulating layer that should be of the same order of magnitude with the short ξ_c. One sound solution is to build devices using a-axis HTCS thin films and heterostructures taking advantage of the longer ξ_{ab}.

In the literature different attempts are presented for the growth of a-axis HTCS thin films and heterostructures [1, 82, 83, 84, 85, 86, 87, 88, 89]. For the growth of a-axis $YBa_2Cu_3O_7$ (YBCO) and heterostructures the strategies were to use different deposition techniques and conditions and to grow the films on (001) or (110) substrates with low lattice mismatch and convenient lattice relationship between the substrate and the film. It was mentioned that, usually, when using (001) or (110) perovskite substrates, mixed a-axis/c-axis and a-axis/(103) orientations are obtained, respectively. A lower growth temperature is favorable to obtain a higher ratio of a-axis orientation. However, many papers could not demonstrate very clean a-axis thin films. Also crystal or orientation quality in many cases were not high, critical temperatures were relatively low, or in-plane alignment was poor. Among the solutions to improve the a-axis YBCO thin films was to replace Y with another rare earth such as Pr [86] or Eu [85]. For these elements a-axis high quality 123 thin films are obtained easier. Buffers of PrBCO or EuBCO can be used for subsequent deposition of high quality a-axis YBCO thin film. Other template solutions can be found in the literature [88, 89, 90]. New means to control and improve orientation and quality in a-axis YBCO thin films are highly desired and this work shows the results of three different deposition programmes as indicated in table 6.1:

- **No.1** After finishing the deposition, oxygen is introduced up to a pressure of 900mbar, cooling with 10^0C/min is undertaken from the growth temperature down to 550^0C and after keeping the sample at this temperature for 30min cooling to room temperature is done with a rate of about 15^0C/min.

Table 6.1: Samples investigated for a-axis growth. Given is the substrate temperature during deposition and the heat treatment program.

Sample	Substrate temperature °C	Program No.
A	610	1
B	610	2
C	630	1
D	630	2
E	630 →690	2
F	630 →720	2
G	650	1
H	650	2
I	650	3
J	690	1
K	750	1
L	780	2
M	825	2

- **No.2** After finishing the deposition, the sample is heated to 825^0C with 10^0C/min and cooled down to 735^0C with 10^0C/min. Oxygen is introduced up to a pressure of 900mbar at this temperature and cooling to 550^0C and the other steps are similar to No. 1.

- **No.3** After finishing the deposition, the sample temperature is stabilized for 60 min, oxygen is introduced up to a pressure of 900mbar, cooling with 10^0C/min is undertaken from the growth temperature down to 550^0C and after keeping the sample at this temperature for 30min cooling to room temperature is done with a rate of about 15^0C/min.

6.2 Growth of YBCO thin films at different temperatures

In general, it is accepted that the lattice matching relationship between the film and substrate is important to induce a certain orientation in the film. For the growth of YBCO films on (100) $SrTiO_3$ substrate (STO), the most favorable relationship is with (100)STO matching the *ab*-plane of YBCO cell which results

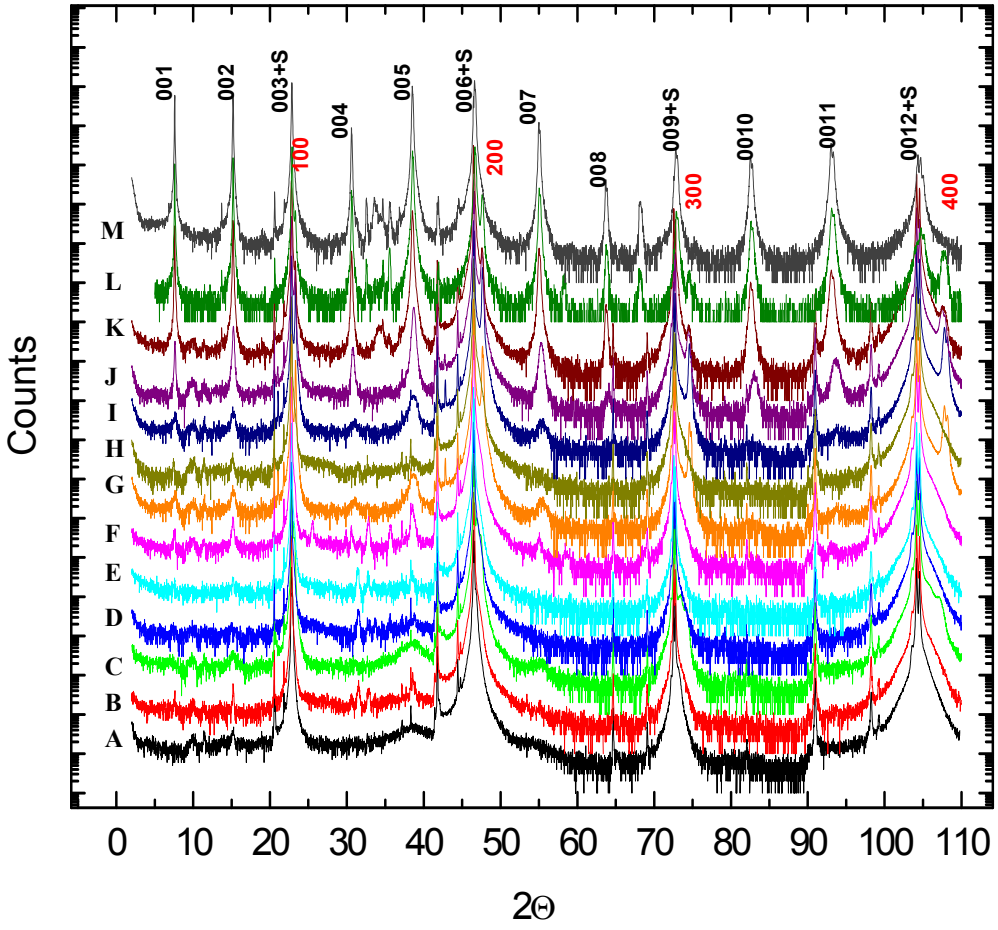

Figure 6.1: XRD patterns of the YBCO thin films. Notation of the samples is as in the Table. 6.1. Notation of the substrate peaks is S.

in a growth with c-axis of the YBCO-cell perpendicular to the substrate. Indeed, many groups succeeded in the growth of high quality single c-axis oriented films on the indicated or other perovskites substrates [1]. However, a second parameter that has a strong influence on the resulting orientation in the film is the mobility of the ad-atoms delivered to the surface of the substrate in the deposition process. This parameter depends in a non trivial way on the substrate state (e.g. vicinal or not, terminal plane, roughness), growth conditions and procedure (atmosphere, plasma, continuous or interrupted deposition), and deposition method (closer to equilibrium such as MOCVD or MBE or far away from it such as sputtering or PLD). A strong influence in controlling mobility has the growth temperature (T_g). A lower growth temperature is suppressing formation of the c-axis orientation and a-axis orientation occurs in YBCO films. The a-axis orientation growth needs less mobility than for the growth of c-axis orientation. This is because of the anisotropic and layered crystal geometry and chemistry of YBCO. For a-axis growth (or b-axis growth, YBCO being tetragonal at high temperatures of growth), there are almost no rearrangements of the atoms necessary to generate the YBCO lattice, and the easy growth direction of YBCO crystals is a-axis. At the same time for the a-axis growth, the lattice mismatch relationship between the film and substrate is less convenient than for c-axis growth. In the former case three $SrTiO_3$ surface unit cells are matched by one surface cell of the YBCO. It results that in the growth of both a-axis or c-axis thin films opposite conflicting influences are involved, but the situation is not symmetric with a-axis growth being less favorable.

All data of this work are supporting the above discussion. For example in case of lower substrate temperature (610^0C) the a-axis has preference. When the temperature goes higher(825^0C), c-axis has preference. In between these two substrate temperature, both a and c-axis will appear. The amount of impurity orientations (c-axis in the a-axis film and a-axis impurity in the c-axis film) and of impurity phases (most probable being $BaCuO_2$ ascribed to the peaks observable on the left side of the substrate peaks in the XRD patterns, Fig. 6.1), as well as T_c (of 18 K for a-axis sample 650-1 and 89.5 K for c-axis sample 825-1/2, Fig. 6.2) are significantly higher for the c-axis film. For the c-axis films (825-1) superconducting transition is sharp hinting on high quality of this film.

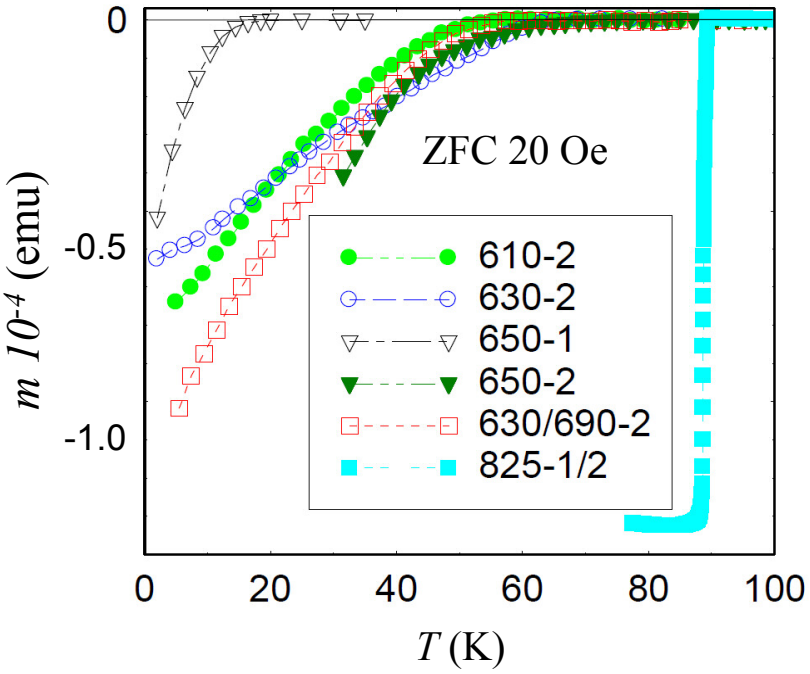

Figure 6.2: Zero-field-cooling magnetization curves for YBCO thin films. Magnetic field was applied parallel to the substrate except for the sample 825 for which it was perpendicular.

Other observations of interest:

(a) The c-axis oriented sample grown at 825°C is likely not totally free of a-axis impurity orientation as suggested by XRD (Fig. 6.1) and rocking curve data (Figs. 6.6 and 6.7). It also might contain an un-known impurity ($2\theta = 34^0$) well observable in the sample grown at 780°C and somehow detectable up to higher growth temperatures (Fig. 6.1). One must emphasize that many articles claiming pure c-axis YBCO films are not showing details of structural characterization (e.g. use of logarithmic scale in XRD data).

(b) At low growth temperatures of 610 or 630°C superconductivity could not be detected by magnetic measurements down to 2K. The difference in the oxygen intake or insufficient atomic ordering is suspected to be responsible, since XRD suggests that the YBCO crystal phase occurs and its crys-

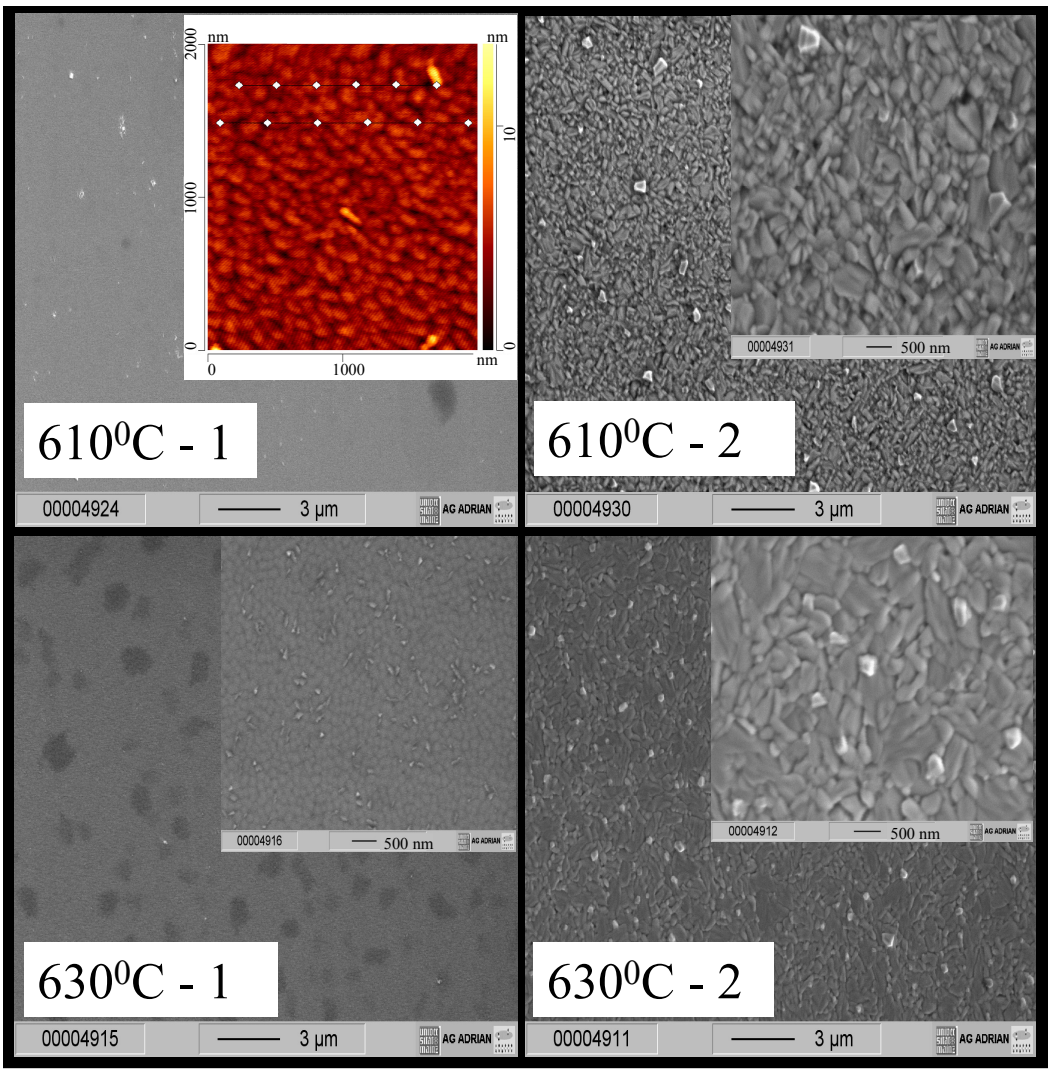

Figure 6.3: Scanning electron microscopy (SEM) images of YBCO thin films prepared with program no.1 (samples indicated with 1) and grown by template approach and post-annealed (samples indicated with 2). Insets are SEM images taken at higher magnification. For sample 610-1 in the inset one AFM image is presented.

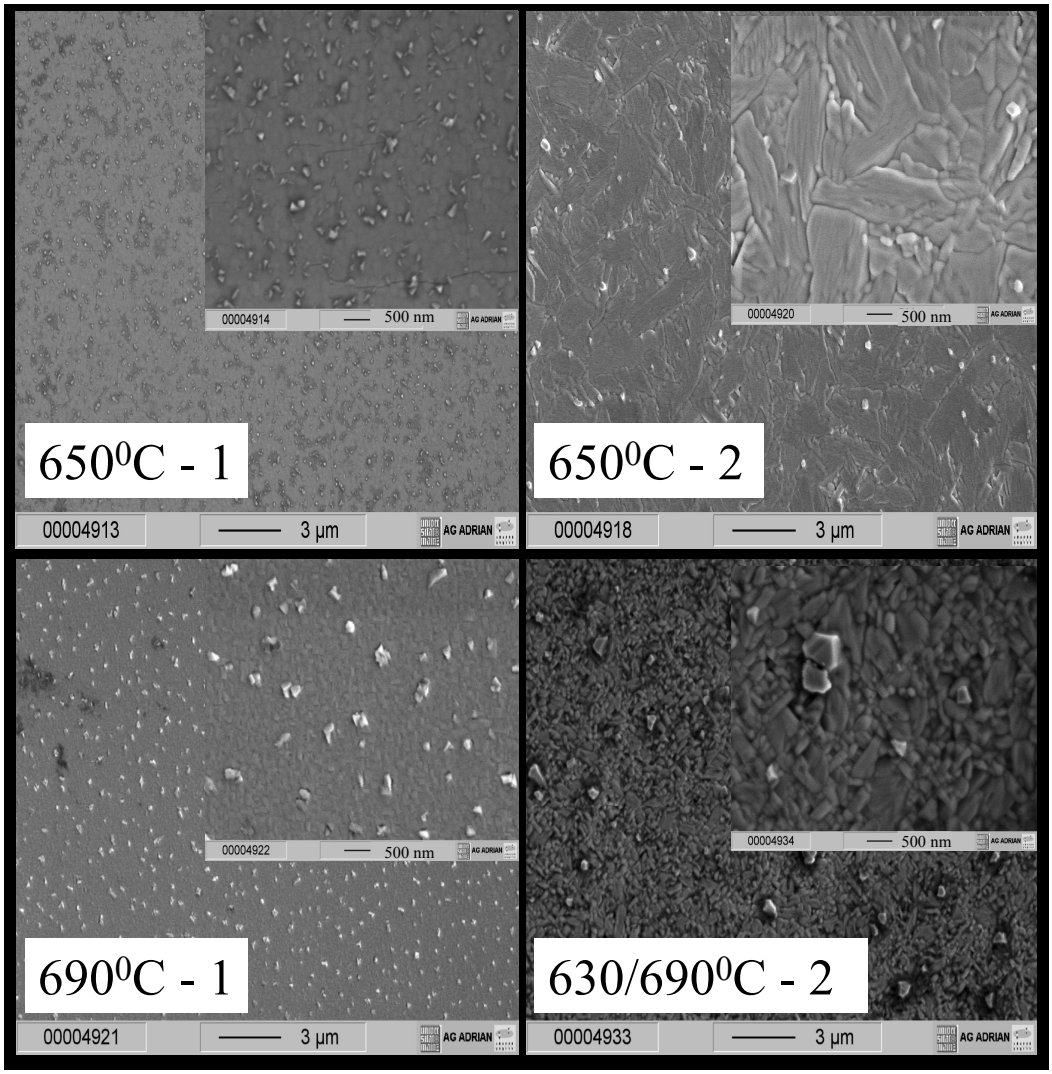

Figure 6.4: Scanning electron microscopy (SEM) images of YBCO thin films prepared with program no.1 (samples indicated with 1) and grown by template approach and post-annealed (samples indicated with 2).

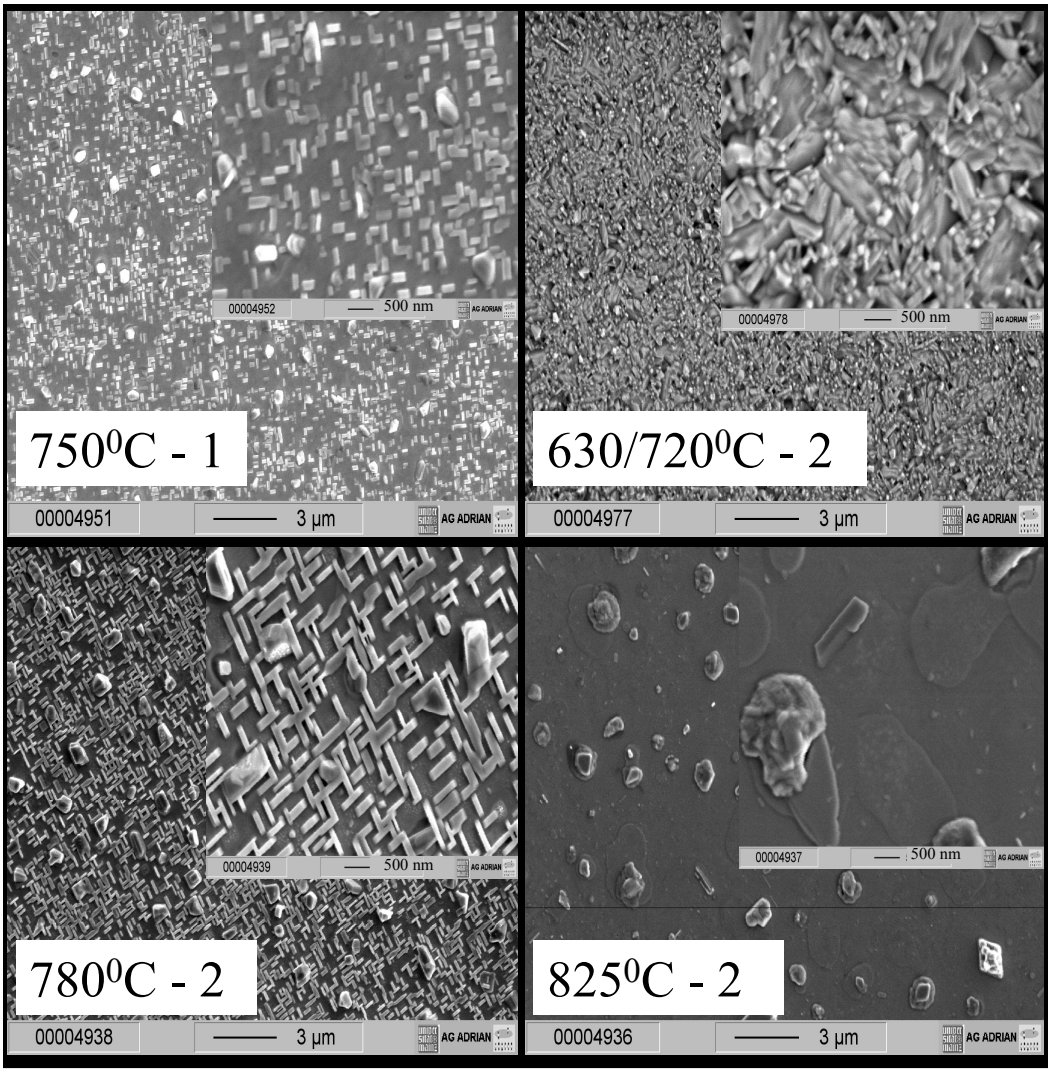

Figure 6.5: SEM images of YBCO thin films prepared with program no.1 (samples indicated with 1) and grown by template approach and post-annealed (samples indicated with 2).

tal/orientation quality is rather good. FWHM of (200) peak (Figs. 6.6,6.7) for the 610-1, 630-1 or 650-1 samples is low. At the same time, the intensity of the rocking curve peak on (005) plane is weak, so that we could not determine FWHM for the samples 610-1 and 630-1. However, for 650-1, FWHM (005) is sharply taking larger values. In fact at growth temperatures of 650 or 690°C, FWHM for both (005) and (200) show a maximum, that is higher for (005) than for (200). At growth temperatures over 690°C FWHM is decreasing for both (200) and (005). The decrease is faster up to 750°C and above this temperature is slow or FWHM is constant. For growth at 750°C the (200) rocking curve peak shows (Fig. 6.6) a splitting meaning that there are macro regions of a-axis crystal grains, each region with its own a-axis misalignment.

(c) XRD and rocking curve data seems to correlate with morphology data as in (Figs. 6.3 to 6.5). At low growth temperature, grains are small, uniform and of rather circular or ellipsoidal shape (Fig. 6.3 and 6.4 from 610-650°C). AFM image (Fig. 6.3 inset) also suggests that poor in-plane alignment occurred, even if SEM data apparently does not confirm this. Roughness is also low. In such circumstances considering that these grains are of *a*-axis orientation (see paragraphs (a) and (b)), probability for *a*-axis misalignment and defects presence is expected to be low. Hence FWHM (200) value is small as already mentioned At higher growth temperatures larger grains form, and rectangular-shape grains are already observable, but not very clear at 690°C. Uniformity of size is good, but roughness is higher. In-plane alignment is significantly improved and can be detected by SEM. This morphology is accompanied by continuous distribution in the *a*-axis and *c*-axis misalignment with the high values of FWHM of (200) and (005) noted at point (b). Samples grown at 750 and 790°C show *a*-axis oriented grains of typical rectangular shape, well defined, in-plane aligned and twinned. These grains are islands in a *c*-axis matrix. Uniformity of size for *a*-axis grains is lower than before especially at 780°C and one may observe smaller and bigger grains. This might be the reason for regions with certain *a*-axis misalignment producing the splitting in the rocking curve of the (200) peak even if FWHM of (200) and (005) reflections is decreasing at high temperatures. The results indicate that the dependence between growth temperature, FWHM of *a*-axis and *c*-axis orientations and morphology is rather complex. Both orientation and morphology evolution bring useful information about the quality of the films and should not be neglected when characterizing thin films.

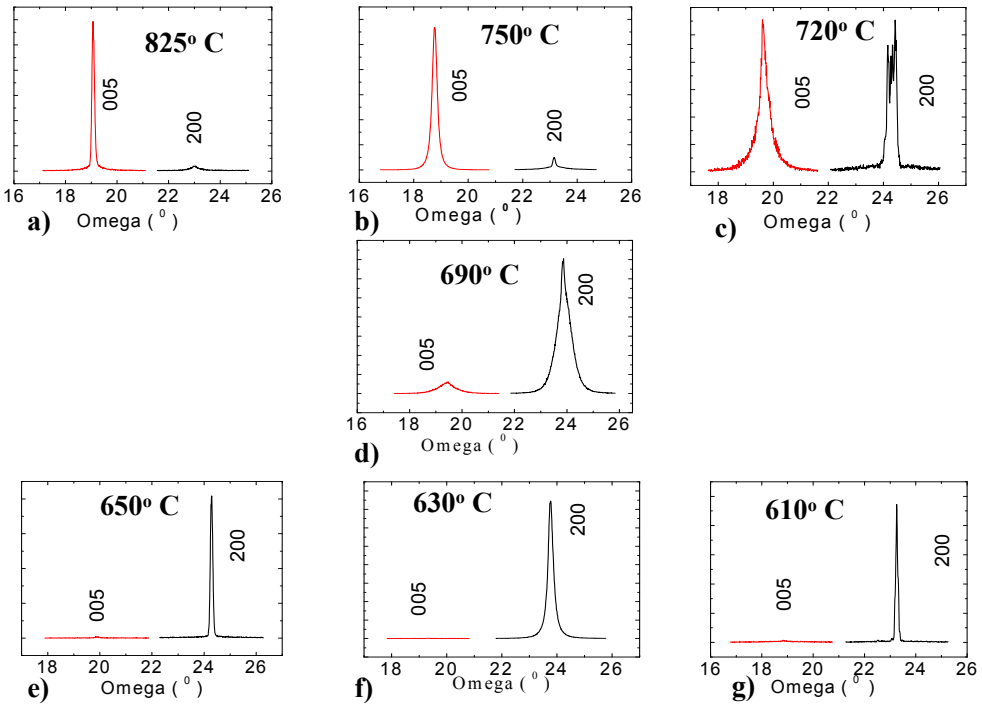

Figure 6.6: Rocking curves of (200) and (005) planes of $YBa_2Cu_3O_7$ thin films. Indicating that the evolution from c-axis to a-axis oriented growth.

(d) At growth temperatures of $630-690^0$C some ribbon whisker-like grains with triangular tips of about 45^0 likely protruding from the surface of the film and being perpendicular to the substrate were observed. They are very similar to conventional single crystal YBCO whiskers and from their shape one can speculate that they are of a-axis orientation perpendicular to the substrate. The mechanism by which such whisker-like grains are grown is not clear now. Especially the formation of the triangular tip is puzzling. It is possible that they grow on the surface of the already formed film on the advanced stages of growth without penetrating down to the surface of the substrate the entire thickness of the mainly a-axis thin films. More research is required.

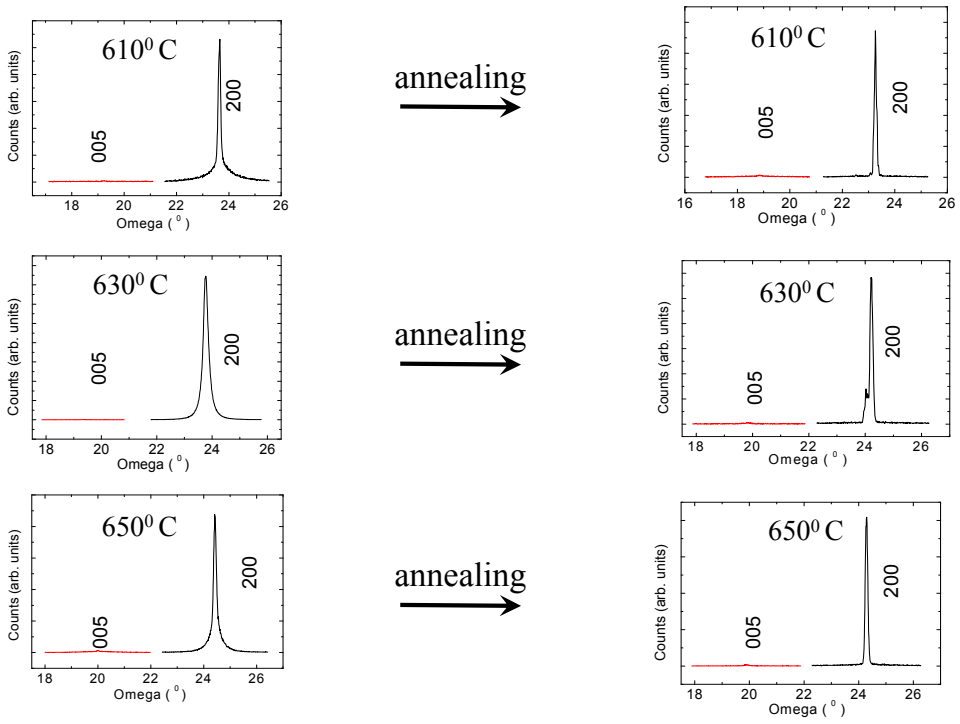

Figure 6.7: Rocking curves of (200) and (005) planes of $YBa_2Cu_3O_7$ thin films before (left) and after (right) annealing.

6.3 Growth of YBCO thin films with post-annealing

As-prepared a-axis thin films presented in 6.2 have shown low T_c (Fig. 6.2). This led to the idea to apply post-annealing at higher temperatures and template growth.

Samples with post-annealing of type (2) (see experimental) have shown enhancement in T_c (57.5 K, 66 K, 73 K for 610-2, 630-2 and 650-3, respectively). T_c-data indicate that the growth history through the growth temperature T_g is important to determine T_c of the post-annealed samples. Post-annealed films of a-axis orientation 610-2, 630-2 and 650-2 had lower or similar values of FWHM (200) than for the as-prepared 610-1, 630-1 and 650-1 samples. On the other hand, FWHM (005) for the same post-annealed samples was higher in 610-2 and 630-2 than for 610-1 and 630-1, but the maximum in FWHM for 650-2 was

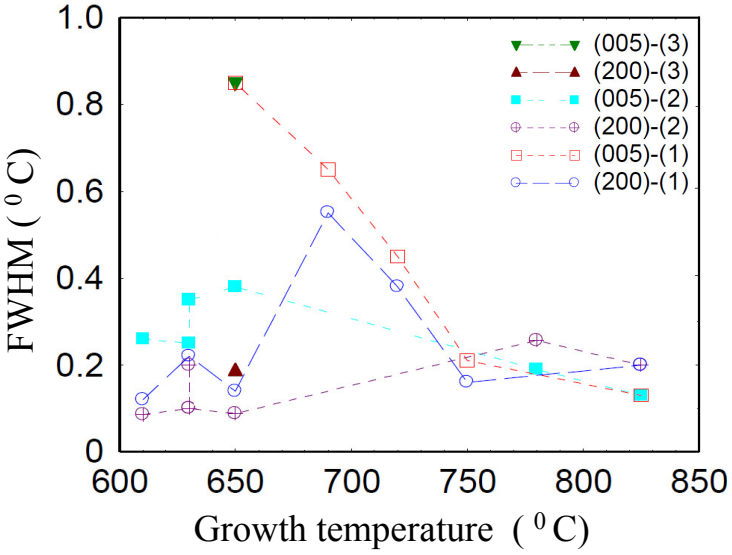

Figure 6.8: FWHM for (200) and (005) vs. growth temperature for YBCO thin films without (regime (1)) and with post annealing (regime (2) and (3)). In some cases the growth of thin films was repeated in identical conditions to see the reproducibility of FWHM. Dotted lines are guide for eyes.

significantly lower than in 650-1. This kind of non symmetric influence of the post-annealing suggests that post-annealing influences in a different way both a-axis and c-axis oriented grains. XRD (Fig. 6.1) seems to support this observation. There is a different decrease of (00l) and (h00) peak intensity in 610-2, 630-2 and 650-2 samples with post-annealing vs. similar ones 610-1, 630-1 and 650-1 without post-annealing (Fig. 6.1). An explanation is missing at this moment and perhaps this is related with some lattice softening at high temperature of post-annealing (825°C) by some kind of local amorphization/melting process. This can help to release strain and/or improve misalignment to improve FWHM, as mentioned. The effect of peak intensity decrease seems to be stronger for the c-axis orientation than for the a-axis in 650-2 and this may suggest some kind of c-axis removal. But, because (h00) peaks are partially overlapping with the peaks belonging to the substrate (S) one cannot draw a conclusion. If the above assumption is real one should imagine some local recrystallization/rearrangement process to explain removal of c-axis orientation by post annealing. A longer post-annealing time of 30 min at 825^0C (sample 650-3) shows a strong influence on

the amount (Fig. 6.1) and FWHM (Fig. 6.7) of the c-axis orientation. Morphology of the samples 610-2, 630-2 and 650-2 is different from the similar samples without annealing. Grain size is enhanced. Size in the post-annealed samples is increasing with the growth temperature of the films and in-plane alignment is poor. Considering the data from 6.2 one concludes that morphology of the post-annealed samples strongly depends on the growth history and in particular on T_g.

Two-temperature template samples 630/690-2 and 630/720-2 were prepared and post annealed. The two samples did not show significant improvement. On contrary data indicate that post annealed sample 630-2 was superior to the template ones from several points of view. A higher template temperature (630/720-2) was better only because it produced a relatively low FWHM (200) similar to sample 630-2. However, a higher c-axis orientation amount was found in the XRD pattern. Morphology of the template samples was intermediate between the morphology of the samples obtained at lower and higher temperatures.

6.4 (110) oriented $YBa_2Cu_3O_7$ on (110)$SrTiO_3$

Since 1988, a lot of effort has been expended to grow a-axis oriented YBCO films. Most of these preparation have been by physical vapor deposition (PVD) methods [91, 92, 93, 94, 95, 96, 97]. a-axis oriented YBCO films may be more suitable for preparing layer-type Josephson junction or weak-link devices because the coherence length in ab-planes is much longer than the direction c-axis [98]. In the present work the growth of high quality films with the ab-plane normal to the film surface on (110)STO is described. The possible growth directions on the (110) $SrTiO_3$ substrate are sketched in Figs. 6.9 and 6.10.

Pure (110) oriented YBCO thin films on $SrTiO_3$ (110) substrates with a high quality growth have been investigated. After having obtained the optimum condition to growth a pure a-axis oriented YBCO film on (100) $SrTiO_3$ substrate with a FWHM $\approx 0.09^0$ at (200) as described in the previous section, the growth of ab-plane (110) oriented films on (110) $SrTiO_3$ was done with the same conditions. The result is that, $YBa_2Cu_3O_7$ films have been grown epitaxially on $SrTiO_3$ (110) substrate with a unique a and b-axis orientation and full in-plane alignment of the c-axis.

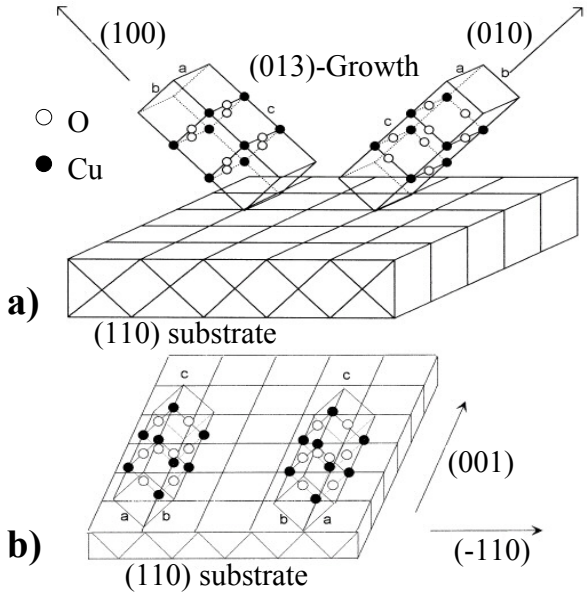

Figure 6.9: Schematic illustrations of the a) (103) or (013) oriented growth b) of (110) oriented of $YBa_2Cu_3O_7$ on the (110) plane of $SrTiO_3$ [99].

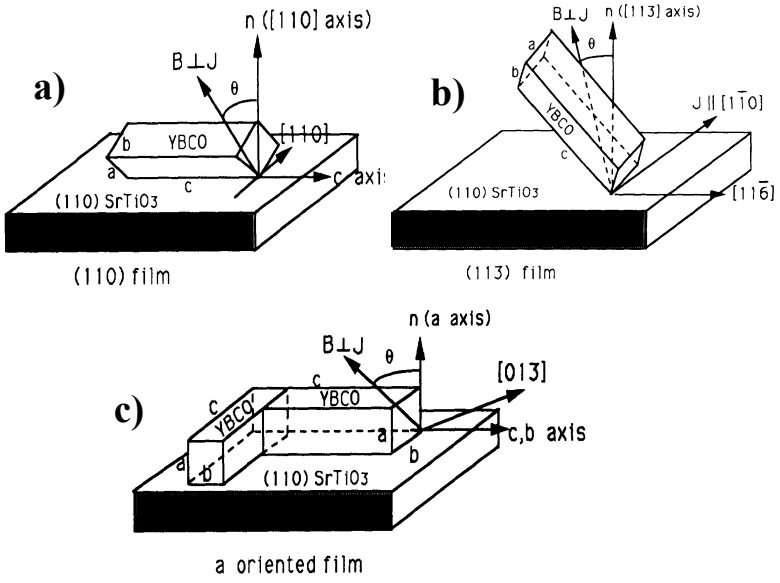

Figure 6.10: Schematic illustrations of the a) (110) growth of $YBa_2Cu_3O_7$ film on (110)STO, b) (113) oriented growth on (110)STO and c) a-axis oriented film growth on $SrTiO_3$ showing only crystal edges [100].

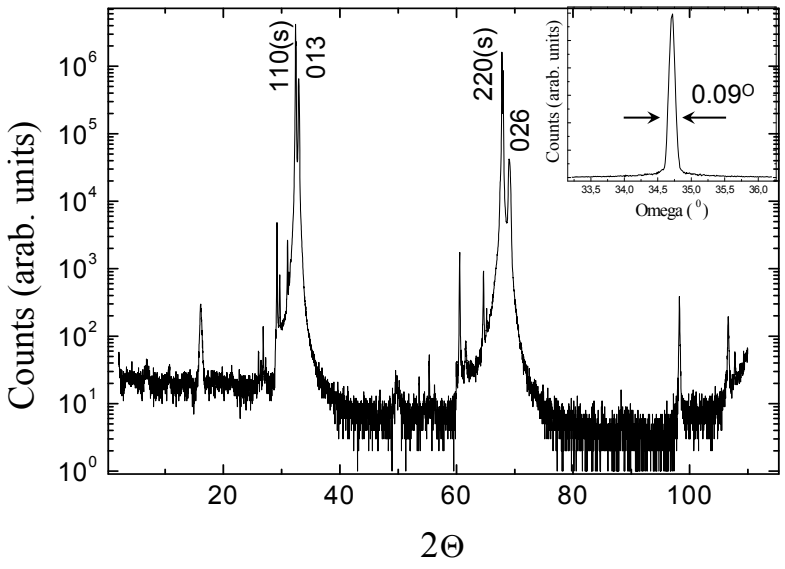

a)

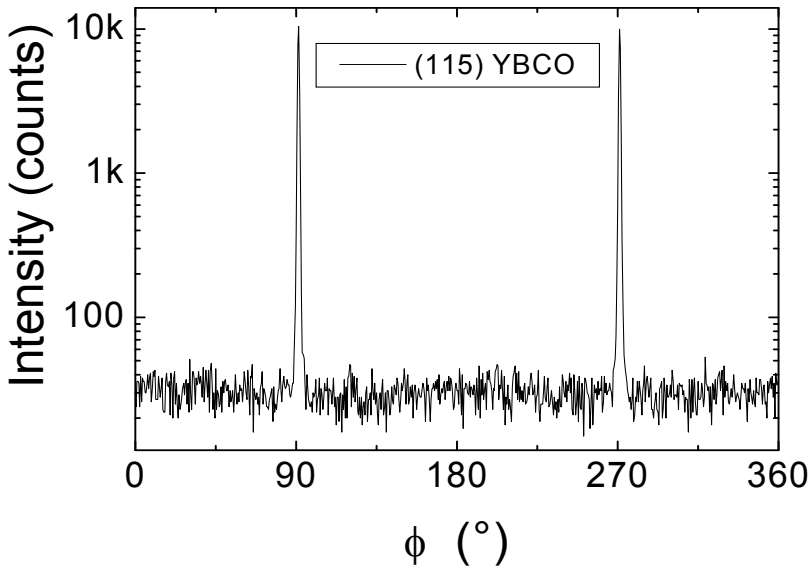

b)

Figure 6.11: X-ray diffraction patterns of YBCO film samples a) Main panel: $\Theta - 2\Theta$ scan on $SrTiO_3$ (100). The inset shows the rocking curve of the (220) reflection with FWHM $\approx 0.09^0$. b) ϕ-scans of YBCO (115) reflections indicating that the c-axis is oriented uniquely within the substrate plane.

6.4.1 In-plane resistance anisotropy for unpatterned (110) oriented films

First experiments on the in-plane resistivity anisotropy simply used four contacts at the corners of unpatterned thin films and the current was applied between contacts in line with the c-axis and ab-plane direction, respectively, as is shown in the inset of Fig. 6.12. A large difference exists between the ab-plane (resistance at room temperature 5 kΩ) and c-axis (resistance at room termperature 1.4 Ω) direction in the films in the normal state. This difference is shrinking rapidly close to the superconducting T_c and the same critical T_c of 85 K is found in both measurements, which are shown in Fig. 6.12. The T_c of these purely (110) oriented film is comparable to the highest values of 89 K reported so far [101, 102]. Already in this measurement the resistance anisotropy is much larger than expected. However, as the current direction is not well defined samples were also patterned with bridges along defined crystallographic directions.

6.4.2 In-plane resistance anisotropy for patterned (110)-axis oriented films

For a better defined current flow bridges with a dimension of $40 \times 260\,\mu m^2$ were photolithographically patterned parallel to the uniquely defined c-axis and ab-plane directions of these films. In Fig. 6.13 the resulting temperature dependence of the resistance is shown for both cases. In contrast to the unpatterned sample for these bridges no real superconducting transition is seen for current parallel to the c-direction. There is at most a superconducting onset visible. This interpretation is supported by the nonlinear current voltage behavior for low temperatures.
As T_c is a thermodynamic quantity one sample should have only one critical temperature. For YBCO the resistance anisotropy between c- and a direction for optimally doped samples is expected to be in the range 5-10. Therefore the observed behavior is hard to explain with intrinsic properties. On the other hand the samples seemed to be homogeneous and the patterning successful as was checked by optical microscopy inspection. These considerations triggered a more thourogh investigation of the sample properties using an electron microscopical and atomic force microscopy inspection of the bridges as shown in Fig. 6.14. No features significant for transport experiments were observed in AFM measurements (part b) of the figure). However, in the scanning electron

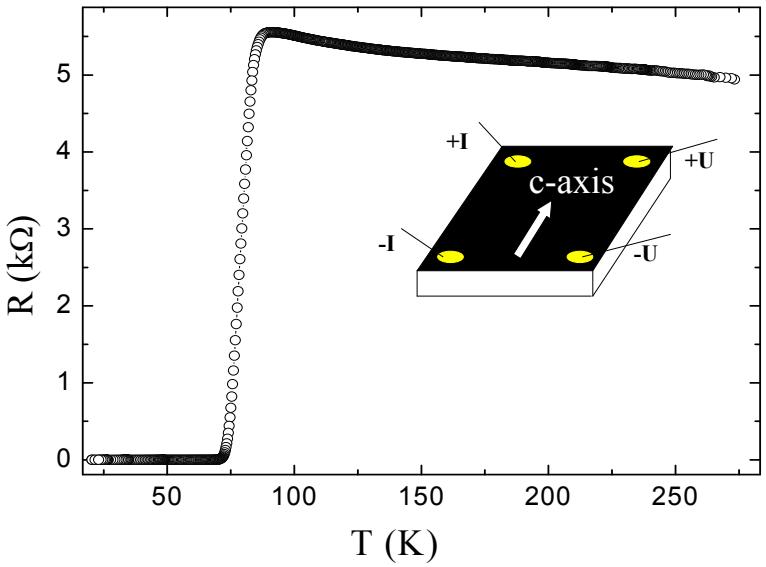

a)

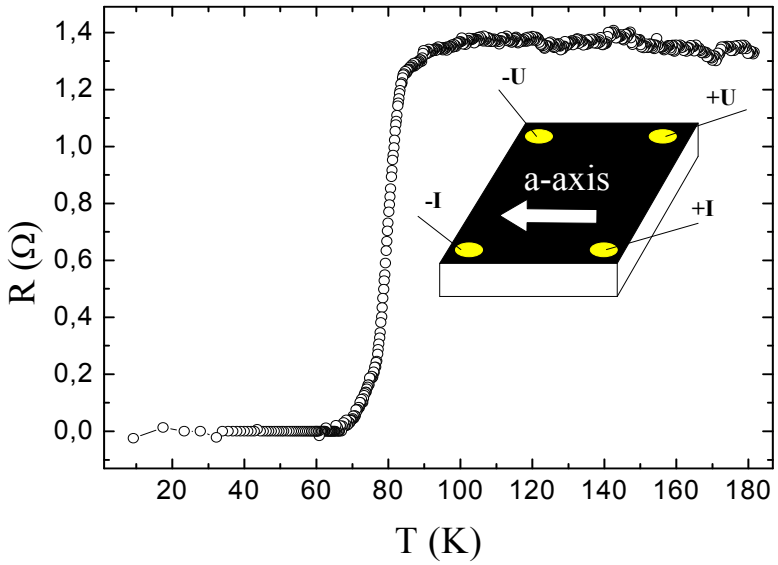

b)

Figure 6.12: In-plane resistance anisotropy for (110) oriented unpatterned films. The resistance versus temperature curves were measured with the current directed mainly along the *c*-axis in a) and along the *ab*-plane in b) film direction by using 4 contacts at the corners of the film.

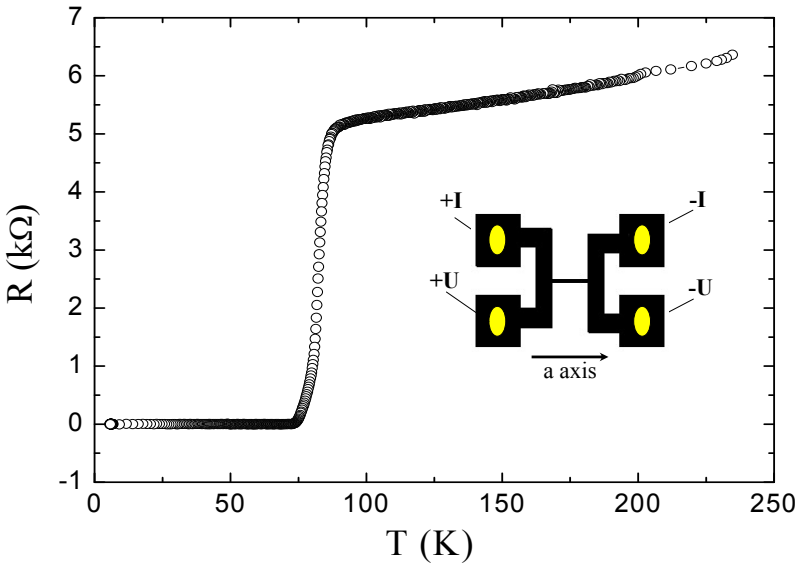

a)

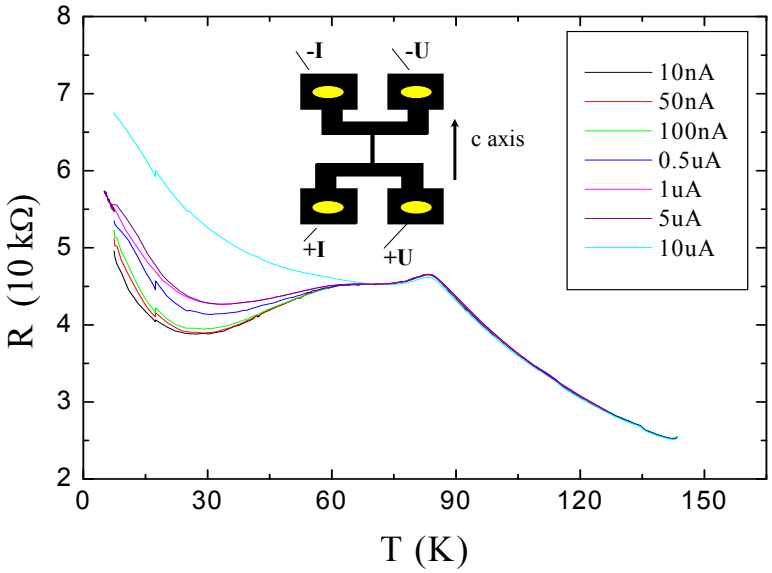

b)

Figure 6.13: The resistance versus temperature curves of a) a bridge of dimension $40 \times 260\,\mu m^2$ directed along the a-axis and b) an identical one directed along the c-axis. In both cases a 4 point measurement was used to eliminate contact resistances. For the bridge along the c-axis different current values were used.

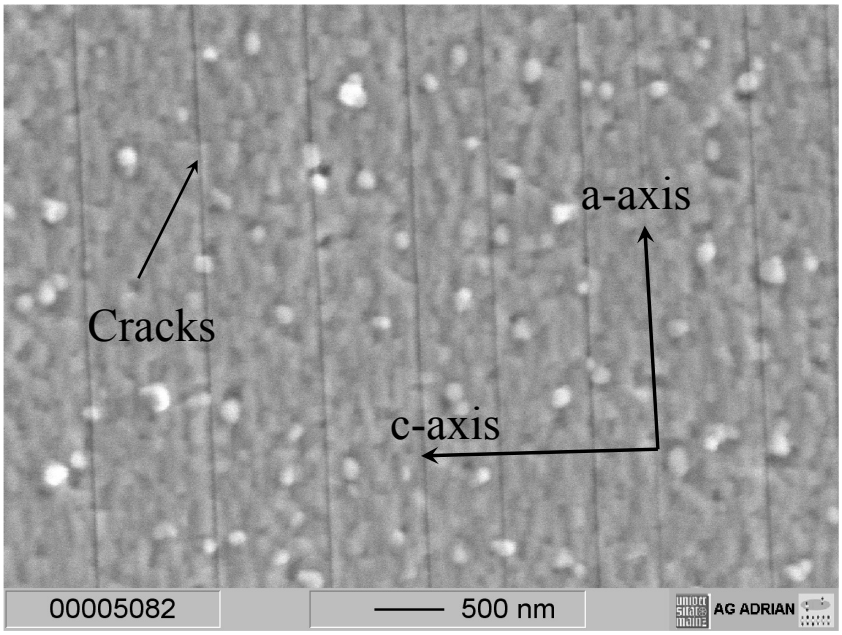

a)

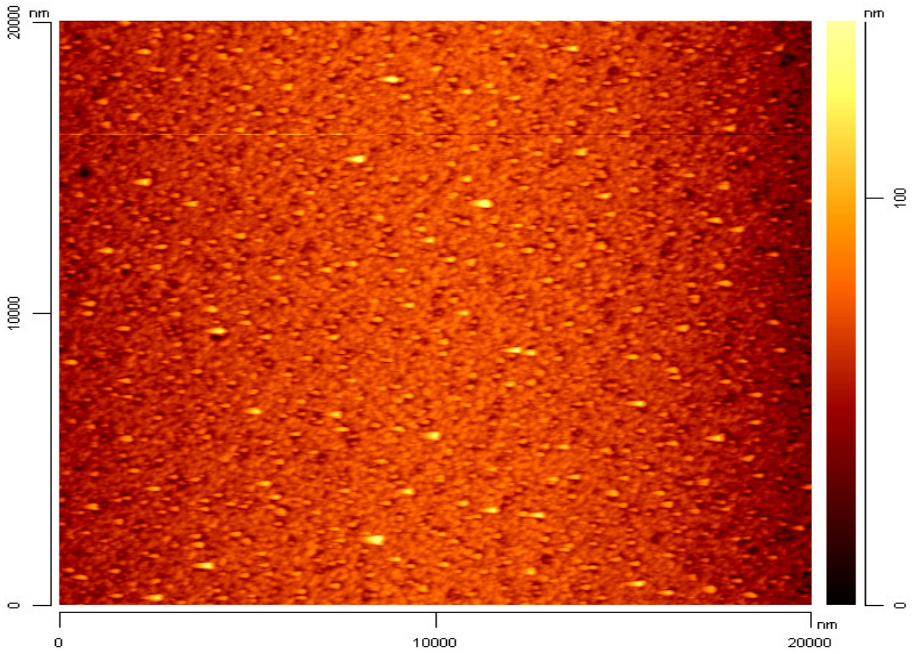

b)

Figure 6.14: Scanning electron microscopy (SEM) image a) and atomic force microscope (AFM) image b) of a-axis oriented YBCO on (110) $SrTiO_3$. In a) the crack alignment is evident while no features were observed by AFM in b).

microscopy image parallel lines perpendicular to the c-axis direction are visible with a typical distance of 400 nm. Due to the results of the transport experiments these lines are evidently cracks in the film. They can be caused by a different thermal expansion of YBCO along the a- or c-axis direction. More probable is that they will be induced by the shrinking of the c-axis direction due to oxygen uptake. The films are prepared fully epitaxial in the tetragonal highly oxygen deficient phase with oxygen content close to O_6. In the oxygen annealing step the O_7 phase is formed. The lattice constants for bulk material are at room temperature 11.85 Å and 11.65 Å for the oxygen deficient and oxygen rich phase, respectively [103, 104]. For the c-axis oriented films this will lead simply to a small thickness reduction. However, if the c-axis is aligned in the plane with the a-axis of the $SrTiO_3$ substrate an epitaxial stress will built up, which obviously leads to the observed coherent formation of cracks.

The cracks lead in case of unpatterned samples to a percolative current path through the sample. While the contacts are placed along the c-axis direction most of the current flow will be meandering along ab-plane directions avoiding if possible the cracks. Thus the resistance anisotropy is induced by a current path different from the macroscopically expected one.

Patterning bridges in the sample cancels the possibility of meandering current paths. For bridges parallel to the ab-plane-direction the current can flow parallel to the cracks and they will not be visible in the transport experiments. For bridges parallel to the c-direction the current must cross the cracks if the lateral sample dimension is smaller the length of a crack. From the observed resistance behavior in Fig. 6.13 it looks as part of the cracks act as tunneling barriers, while others are acting as Josephson junctions or weak links.

Two strategies to avoid the crack formation are possible. One would be to use very thin films. Below a critical thickness the strain energy will not lead to crack formation. However, one would not end up with $YBa_2Cu_3O_7$ comparable to the bulk material. The strain along the c-axis would change the superconducting properties. Another point is that for very thin films oxygen loss at the sample surface can not be neglected and T_c is reduced due to this fact. The other strategy would be to omit the annealing step. But if one omits the annealing step crack formation might be suppressed, but superconductivity is lost.

In this chapter the evolution of a-axis to c-axis oriented growth was studied in $YBa_2Cu_3O_7$ thin films grown by sputtering. The investigations reveal some details of the complex relationship between growth, orientation, morphology

and superconducting properties. It is important to note that post-annealing and template growth can produce different growth effects, influencing with different strength different quality details of the films. Further optimization processes should be investigated in order to improve growth control and finally to improve *a*-axis YBCO thin films on (100)STO. Use of growth conditions as for sample 650-2 led to growth of in-plane aligned top quality thin films of (100)YBCO on (110)STO. By using these optimum condition, a *a*-axis oriented growth with unique *c*-direction aligned in plane on (110) STO with high quality in x-ray diffraction (FWHM 0.09^0) was obtained. Thus it was demonstrated how to achieve good *a*-axis oriented growth on $SrTiO_3$ substrate by optimization of the deposition conditions. On (100)$SrTiO_3$ good superconducting properties are achieved, but the symmetry of the surface prevents a quantitative determination of the anisotropy. For samples grown on (110)$SrTiO_3$ a uniaxial alignment of the *c*-axis direction in the substrate plane was achieved. However, the existence of coherent crack patterns disturb the transport experiments.

CHAPTER 7

SUMMARY

7.1 Conclusion

The understanding of the strength and type of coupling between superconducting $YBa_2Cu_3O_7$ decoupled by non superconducting $PrBa_2Cu_3O_7$ in c-axis oriented $YBa_2Cu_3O_7/PrBa_2Cu_3O_7$ superlattice was the aim of this thesis. For this purpose two conceptually different kind of transport experiments have been performed. In the first type of transport experiments the current is flowing parallel to the layers. Here the coupling is probed indirectly using the vortex lines, which are penetrating the superlattice. Movement of the vortex segments in neighbouring $YBa_2Cu_3O_7$ layers is more or less coherent depending on the thickness of both the superconducting and non superconducting layers. This in-plane transport was measured either by sending an external current through bridges patterned in the superlattice or by an induced internal current. In the latter case the current is inductively induced and the decay of the induced superconducting magnetization is monitored. The decisive physical quantity is in both cases the vortex-creep activation energy. It is measured at 'high' dissipation levels in the transport experiments and at extremely low levels in the magnetic relaxation experiments. The second type of experiments tried to measure directly a possible Josephson coupling between superconducting CuO_2 double planes in the superlattices by investigation of the transport properties perpendicular to the superconducting planes. Here three different routes of access have been tested. The first one was to pattern mesa structures photolithographically as in previous works. The second used threedimensional nanostructures cut by a focused ion

beam. A third idea was to use a-axis and (110) oriented $YBa_2Cu_3O_7$ film, where in-plane patterning can in principle be sufficient to measure transport perpendicular to the superconducting planes. In summary the following results could be achieved and conclusions drawn:

The vortex-creep activation energy U was determined by analyzing the in-plane resistive transition of photolithographically patterned bridges with the external magnetic field B oriented along the c-axis. The activation energies for two series of superlattices were investigated. In one series the thickness of the YBCO layers was constant ($nY = 4$) and the number of the PBCO unit cells was varied, while in the other the number of PBCO layers was constant ($nP = 4$) and nY varied. The correlation length of the vortex system was determined to be 80 nm along the c-axis direction. It was found that even a single PBCO unit cell in a superlattice effectively cuts the flux lines into shorter weakly coupled segments, and the coupling of the vortex systems in neighbouring layers is negligible already for a thickness of four unit cells of the PBCO layers. A characteristic variation of the activation energy for the two series of superlattices was found, where U_0 is proportional to the YBCO thickness. A change in the variation of U_0 with the current I in the specimen was observed, which can be explained in terms of a crossover in the vortex creep process, generated by the transport current. At low I values the dislocations mediated (plastic) vortex creep leads to TAFF behaviour, whereas at high I the dc transport measurements are dominated by elastic (collective) creep.

The analysis of standard dc magnetization relaxation data obtained for a series of 200 nm thick $(YBa_2Cu_3O_7)_{nY}/(PrBa_2Cu_3O_7)_4$ superlattices (nY $\leq$ 20) in the low-T region and with H oriented along the c-axis revealed the occurrence of a crossover elastic (collective) vortex creep at low T-plastic vortex creep at high T, generated by the T dependent macroscopic currents induced in the sample. For thin superlattices (nY $<$ 20) the creep crossover temperature T_{cr} increases linearly with increasing nY, and for a fixed superconducting layer thickness T_{cr} decreases linearly with increasing $ln(H)$. By taking into account the T_{cr} value for the YBCO film ($\approx$ 45 K), it can be concluded that $T_{cr}(n)$ should saturate at large effective thicknesses. This happens when the effective thickness overcomes the vortex correlation length. This crossover represents an alternative to the elastic vortex glass behaviour reported for superlattices, as well as to "quantum vortex creep" at unexpectedly high T inferred for thin films. The existence of this creep crossover suggests that, compared with the well known

Maley technique, the use of the normalized vortex creep activation energy is a better solution for the determination of vortex creep parameters.

In the measurements of perpendicular transport using mesa structures no features of the Josephson effect could be directly determined. As it could be checked that the photolithography process steps were done properly and the smallest possible strucutures have been used, the reason is possibly a too low resistance of the fully oxygenated $PrBa_2Cu_3O_7$ layers. Using the innovative method of FIB cut structures we could achieve nanostructures. Here, however, it is unclear whether oxygen loss at the surface or ion beam damage lead to non superconducting structures.

For transport measurements perpendicular to the superconducting planes also films having the planes perpendicular to the substrate surface are suitable. Therefore the deposition of films with this unusual growth orientation was optimized and investigated. The structural and microstructural evolution of c-axis to a-axis orientation was monitored using x-ray diffraction, scanning electron microscopy and magnetization measurements. Films with full a-axis alignment parallel to the substrate normal could be achieved on (110) $SrTiO_3$. Due to the symmetry of the substrate the c-axis direction in-plane is twofold. Transferring the deposition conditions to films grown on (110)$SrTiO_3$ allowed the growth of (110) oriented $YBa_2Cu_3O_7$ films with a unique in-plane c-axis orientation. While these films were of high quality by crystallographic and macroscopic visual inspection, electron microscopy revealed a coherent crack pattern on a nanoscale. Therefore the actual current path in the sample was not determined by the macroscopic patterning which prohibited investigations of the in-plane anisotropy.

7.2 Future direction

The full range of the transport phenomena with transport current perpendicular to the copper oxide planes in high Tc superconductors is rich and complex. Compared to the body of knowledge in in-plane transport still lot of work needs to be done and my thesis was one step in this way, which should be continued. For the mesa strucutures future investigations should work essentially on two points. One is the smoothness of the c-axis oriented films, which could be improved using argon/oxygen gas mixtures. Only smoother films will allow a smaller scale patterning, possibly by electron beam lithography instead of pho-

tolithography. Also the resistance of the insulating layers needs to be improved. Ways to do this could be the use of Ga doped $PrBa_2Cu_3O_7$ layers or the use of $SrTiO_3$ decoupling layers. In the latter case the process must be transferred to rf-sputtering instead of dc-sputtering, which will involve larger effort.

For the focused ion beam patterned samples a series of nanostructures need to be patterned with different geometries and oxygen treatments. By this method one could to get information on what is the contribution of oxygen loss at the exposed *ab*-plane surface and what is the influence of ion etch damage, separately. Then the experiment shown in this work should be repeated with a properly optimized sample. However, this work will need a large amount of time on the focused ion beam system.

The coherent crack pattern on a nanoscale for (110) oriented $YBa_2Cu_3O_7$ grown on (110)$SrTiO_3$ can possibly not be avoided without degradation of superconductivity. Thus the most promising idea will be to use finer patterning features in the future and to measure the transport anisotropy within a small crack free region. Due to the very small dimensions needed, this could be possibly done with a focused ion beam system as the one available in Frankfurt combined with electron beam lithography.

The measurements of in-plane transport on the decoupling of the vortex lines were very successful. The basic ideas on the vortex system could be confirmed and new aspects could be found. It would be nice, if other groups could confirm the vortex-creep crossover found here independently on different samples with a different method, as e.g. using a torque magnetometer, where no sample movement is involved.

BIBLIOGRAPHY

[1] M. Leskela, H. Molsa, and L. Niinisto, Supercond. Sci. Technol. **6**, 627 (1993).

[2] I. Bozovic, IEEE Trans. Appl. Supercond. **11**, 2686 (2001).

[3] D. Mandrus, L. Forro, D. Koller, and L. Mihaly, Nature **351**, 460 (1991).

[4] K. Ohki, N. Iwashita, K. Kikunaga, T. Okuda, K. Obara, and N. Terada, J. Phys. Conf. Ser. **43**, 1159 (2006).

[5] V. L. Ginzburg and L. D. Landau, Zh. Eksp. Teor. Fiz. **20**, 1064 (1950).

[6] A. Abrikosov, Soviet Phys. JETP **5**, 1174 (1957).

[7] M. Tinkham, *Introduction to Superconductivity* (Krieger, Malabar, Florida) (1980).

[8] J. R. Clem, Phys. Rev. B **43**, 7837 (1991).

[9] J.-M. Triscone, M. G. Karkut, L. Antognazza, O. Brunner, and Ø. Fischer, Phys. Rev. Lett. **63**, 1016 (1989).

[10] J.-M. Triscone, Ø. Fischer, O. Brunner, L. Antognazza, A. D. Kent, and M. G. Karkut, Phys. Rev. Lett. **64**, 804 (1990).

[11] D. K. Christen, C. E. Klabunde, R. Feenstra, D. H. Lowndes, D. Norton, J. D. Budai, H. R. Kerchner, J. R. Thompson, L. A. Boatner, J. Narayan, and R. Singh, Physica B **165&166**, 1415 (1990).

[12] G. Jakob, P. Przyslupski, C. Stölzel, C. TomeRosa, A. Walkenhorst, M. Schmitt, and H. Adrian, Appl. Phys. Lett. **59**, 1626 (1991).

[13] G. Jakob, T. Hahn, C. Stölzel, C. TomeRosa, and H. Adrian, Europhys. Lett. **19**, 135 (1992).

[14] O. Brunner, L. Antognazza, J.-M. Triscone, L. Mieville, and Ø. Fischer, Phys. Rev. Lett. **67**, 1354 (1991).

[15] P. W. Anderson and Y. B. Kim, Rev. Mod. Phys **36**, 39 (1964).

[16] M. R. Beasley, R. Labusch, and W. W. Webb, Phys. Rev. **181**, 682 (1969).

[17] K. Yamafuji, T. Fujiyoshi, K. Toko, and T. Matsushita, Physica C **159**, 743 (1988).

[18] Y. B. Kim, C. F. Hempstead, and A. R. Strnad, Phys. Rev. Lett. **9**, 306 (1962).

[19] C. J. V. der Beek, G. J. Nieuwenhuys, P. H. Kes, H. G. Schnack, and R. Griessen, Physica C **170**, 320 (1992).

[20] J. Bardeen and M. J. Stephen, Phys. Rev. **140**, A1197 (1965).

[21] M. V. Feigel'man, V. B. Geshkenbein, A. I. Larkin, and V. M. Vinokur, Phys. Rev. Lett. **63**, 2303 (1989).

[22] D. S. Fisher, M. P. A. Fisher, and D. A. Huse, Phys. Rev. B **43**, 130 (1991).

[23] E. Brandt, Z. Phys. B **80**, 167 (1990).

[24] H. Feigel'man, V. Geshkenbein, and V. Vinkour, Phys. Rev. B **43**, 6263 (1991).

[25] J. J. Gittleman and B. Rosenblum, Zh. Eksp. Teor. Fiz. **20**, 1064 (1950).

[26] R. Griessen, J. G. Lensink, T. A. M. Schroder, and B. Dam, Cryogenics **30**, 563 (1990).

[27] P. H. Kes, J. VanDerBeek, and J. A. Mydosh, Supercond. Sci. Technol. **1**, 249 (1989).

[28] A. Malozemoff, Y. Yeshurun, L. Krunin, T. Worthington, D. Cronemeyer, T. Dinger, F. Holtzberg, T. McGuire, and P. H. Kes, Proceeding of the First Latin American Conference on High Temperature Superconductivity, Rio de Janeiro, Brazil **4-6**, 239 (1988).

[29] A. I. Larkin and Y. N. Ovchinikov, J. Low Temp. Phys. **34**, 409 (1979).

[30] P. Anderson and Z. Zou, Phys. Rev. Lett. **60**, 132 (1988).

[31] G. Jakob, *Präparation, Charakterisierung der Struktur und Untersuchung der Transporteigenschaften von $YBa_2Cu_3O_7/PrBa_2Cu_3O_7$-Übergittern*, Ph.D. thesis, Technical University Darmstadt (1993).

[32] A. Schattke, *Transport properties perpendicular to the copper oxide planes of high temperature superconductor thin films and superlattices*, Ph.D. thesis, Johannes Gutenberg University, Mainz (1998).

[33] E. E. Fullerton, I. K. Schuller, H. Vanderstraeten, and Y. Bruynseraede, Phys. Rev. B **45**, 9292 (1992).

[34] C. L. Jia, A. Thust, G. Jakob, and K. Urban, Ultramicroscopy **49**, 330 (1992).

[35] H. C. Yang, L. M. Wang, and H. E. Horng, Physica C **321**, 285 (1997).

[36] M. Varela, D. Arias, Z. Sefrioui, C. Léon, C. Ballesteros, and J. Santamaria, Phys. Rev. B **62**, 12509 (2000).

[37] B. Holzapfel, G. Kreiselmeyer, M. Kraus, G. Saemann-Ischenko, S. Bouffard, S. Klaumünzer, and L. Schultz, Phys. Rev. B **48**, 600 (1993).

[38] Q. Li, X. X. Xi, X. D. Wu, A. Inam, S. Vadlamannati, W. L. McLean, T. Venkatesan, R. Ramesh, D. M. Hwang, J. A. Martinez, and L. Nazar, Phys. Rev. Lett. **64**, 3086 (1990).

[39] M. K. Wu, J. R. Ashburn, and C. J. Torng, Phys. Rev. Lett. **58**, 908 (1987).

[40] J.-M. Triscone and Ø. Fischer, Rep. Prog. Phys. **60**, 1673 (1997).

[41] G. Jakob, P. Przyslupski, C. Stölzel, C. TomeRosa, A. Walkenhorst, M. Schmitt, and H. Adrian, Physica C **185-189**, 2087 (1991).

[42] T. T. M. Palstra, B. Batlogg, R. B. van Dover, L. F. Schneemeyer, and J. V. Waszczak, Phys. Rev. B **41**, 6621 (1990).

[43] S. N. Artemenko and A. N. Kruglov, Phys. Lett. A **143**, 485 (1990).

[44] D. H. Lowndes, D. P. Norton, and J. D. Budai, Phys. Rev. Lett. **65**, 1160 (1990).

[45] J. T. Kucera, T. P. Orlando, G. Virshup, and J. N. Eckstein, Phys. Rev. B **46**, 11004 (1992).

[46] V. B. Geshkenbein, A. I. Larkin, M. V. Feigel'man, and V. M. Vinokur, Physica C **162-164**, 239 (1989).

[47] V. M. Vinokur, M. V. Feigel'man, V. B. Geshkenbein, and A. I. Larkin, Phys. Rev. Lett. **65**, 259 (1990).

[48] T. Matsushita, M. Kiuchi, T. Yasuda, H. Wada, T. Uchiyama, and I. Iguchi, Supercond. Sci. Technol. **18**, 1348 (2005).

[49] N. Ihara and T. Matsushita, Physica C **257**, 223 (1996).

[50] A. I. Larkin, JETP Letters **31**, 219 (1980).

[51] A. Malozemoff, Physica C **185-189**, 264 (1991).

[52] L. Miu, Phys. Rev. B **72**, 132502 (2005).

[53] L. Miu, D. Miu, T. Petrisor, A. E. Tahan, G. Jakob, and H. Adrian, Phys. Rev. B **78**, 212508 (2008).

[54] T. Giamarchi and P. L. Doussal, Phys. Rev. B **52**, 1242 (1995).

[55] J. Kierfeld, H. Nordborg, and V. M. Vinokur, Phys. Rev. Lett. **85**, 4948 (2000).

[56] T. Giamarchi and P. L. Doussal, Phys. Rev. B **55**, 6577 (1997).

[57] D. R. Nelson and V. M. Vinokur, Phys. Rev. B **48**, 13060 (1993).

[58] Q. Li, C. Kwon, X. X. Xi, S. Bhattacharya, A. Walkenhorst, T. Venkatesan, S. J. Hagen, W. Jiang, and R. L. Greene, Phys. Rev. Lett. **69**, 2713 (1992).

[59] G. Jakob, M. Schmitt, T. Kluge, C. Tome-Rosa, P. Wagner, T. Hahn, and H. Adrian, Phys. Rev. B **47**, 12099 (1993).

[60] J. E. Villegas, Z. Sefrioui, M. Varela, E. Gonzalez, J. Santamaria, and J. L. Vicent, Phys. Rev. B **69**, 134505 (2004).

[61] X. Zhang, S. J. Wang, and C. K. Ong, Physica C **329**, 297 (2000).

[62] X. G. Qiu, G. X. Chen, and B. R. Zhao, Phys. Rev. B **68**, 024519 (2003).

[63] C. P. Bean, Phys. Rev. Lett. **8**, 250 (1962).

[64] E. M. Gyorgy, R. B. V. Dover, K. A. Jackson, L. E. Schneemeyer, and J. V. Waszczak, Appl. Phys. Lett. **55**, 283 (1989).

[65] Y. Yeshurun, A. P. Malozemoff, and A. Shaulov, Rev. Mod. Phys **68**, 911 (1996).

[66] G. Blatter, M. V. Feigel'man, V. B. Geshkenbein, A. I. Larkin, and V. M. Vinokur, Rev. Mod. Phys. **66**, 1125 (1994).

[67] M. P. Maley, O. J. Willis, H. Lessure, and M. E. McHenry, Phys. Rev. B **42**, 2639 (1990).

[68] M. E. McHenry, S. Simizu, H. Lessure, M. P. Maley, J. Y. Coulter, I. Tanaka, and H. Kojima, Phys. Rev. B **44**, 7614 (1991).

[69] Y. G. Xiao, B. Yin, J. W. Li, Z. X. Zhao, H. T. Ren, L. Xiao, X. K. Hu, and J. A. Xia, Supercond. Sci. Technol. **7**, 623 (1994).

[70] M. D. Sumption, T. J. Haugan, P. N. Barnes, T. A. Campbell, N. A. Pierce, and C. Varanasi, Phys. Rev. B **77**, 094506 (2008).

[71] J. T. Manson, J. Giapintzakis, and D. M. Ginsberg, Phys. Rev. B **54**, 12517 (1996).

[72] J. R. Thompson, L. Krusin-Elbaum, L. Civale, G. Blatter, and C. Field, Phys. Rev. Lett. **78**, 3181 (1997).

[73] P. J. Kung, M. P. Maley, M. E. McHenry, J. O. Willis, M. Murakami, and S. Tanaka, Phys. Rev. B **48**, 13992 (1993).

[74] M. Abulafia, A. Shaulov, Y. Wolfus, R. Prozorov, L. Burlachkov, Y. Yeshurun, D. Majer, E. Zeldov, H. Wühl, V. B. Geshkenbein, and V. H. Vinokur, Phys. Rev. Lett. **77**, 1596 (1996).

[75] V. B. Geshkenbein and A. I. Larkin, Sov. Phys. JETP **60**, 369 (1989).

[76] H. H. Wen, A. F. T. Hoekstra, R. Griessen, S. L. Yan, L. Fang, and M. S. Si, Phys. Rev. Lett. **79**, 1559 (1997).

[77] F. C. Klaassen, G. Doornbos, J. M. Huijbregtse, R. C. F. van der Geest, B. Dam, and R. Griessen, Phys. Rev. B **64**, 184523 (2001).

[78] V. Vinokur, B. Khaykovich, E. Zeldov, M. Konczykowski, R. A. Doyle, and P. Kes, Physica C **295**, 209 (1998).

[79] I. Giaever, Phys. Rev. Lett. **5**, 147 (1960).

[80] J. G. Simmons, J. Appl. Phys. **34**, 238 (1963).

[81] H. Rodriguez, *Electronic transport properties of* $YBa_2Cu_3O_{7-x}/PrBa_2Cu_{2.9}Ga_{0.1}O_{7-y}$ *trilayers and superlattices perpendicular to the layer structure*, Ph.D. thesis, Johannes Gutenberg University, Mainz (2004).

[82] N. Homma, S. Okayama, H. Takahashi, I. Yoshida, T. Morishita, and S. Tanaka, Appl. Phys. Lett. **59**, 1383 (1991).

[83] C. B. Eom, A. F. Marshall, S. S. Laderman, R. D. Jacowitz, and T. H. Geballe, Science **249**, 1549 (1991).

[84] H. Asano, M. Asahi, and O. Michikami, Jap J Appl Phys **28**, L981 (1989).

[85] J. B. Barner, C. T. Rogers, A. Inam, R. Ramesh, and S. Bersey, Appl. Phys. Lett. **59**, 742 (1991).

[86] A. Inam, C. T. Rogers, R. Ramesh, K. Remschnig, L. Farrow, D. Hart, and T. Venkatesan, Appl. Phys. Lett. **57**, 2484 (1990).

[87] C. B. Eom, A. F. Marshall, J. M. Triscone, B. Wilkens, S. S. Laderman, and T. H. Geballe, Science **251**, 780 (1991).

[88] W. C. Tsai and T. Y. Tseng, Jpn J Appl Phys **36**, 76 (1997).

[89] R. G. Wichern, E. M. C. M. Reuvekamp, G. J. Gerritsma, and H. Rogalla, IEEE Trans. Appl. Supercond. **5**, 2361 (1995).

[90] M. S. Hegde, K. M. Satyalakshmi, S. S. Manoharan, and D. Kumar, Materials Science and Engineering B **32**, 239 (1995).

[91] W. Ito, S. Mahajan, Y. Yoshida, N. Watanable, and T. Morishita, J. Mater. Res. **9**, 1625 (1994).

[92] W. Ito, A. Oishi, S. Okayama, Y. Yoshida, N. Homma, and T. Morishita, Physica C **204**, 295 (1993).

[93] J. G. Wen, S. Mahajan, W. Ito, T. Morishta, and N. Koshizuka, Appl. Phys. Lett. **64**, 3334 (1994).

[94] E. Sodtke and H. Munder, Appl. Phys. Lett. **60**, 1630 (1992).

[95] T. Hashimoto, M. Sagoi, Y. Mizutani, J. Yoshida, and K. Mizushima, Appl. Phys. Lett. **60**, 1766 (1992).

[96] K. Young and J. Sun, Appl. Phys. Lett. **59**, 2448 (1991).

[97] L. Luo, X. D. Wu, R. C. Dye, R. E. Muenchausen, S. R. Foltyn, Y. Coulter, C. J. Maggiore, and T. Inoue, Appl. Phys. Lett. **59**, 2043 (1991).

[98] B. Oh, K. Char, A. Kent, M. Naito, M. Beasley, T. GebaUe, R. Hammond, A. Kapitulnik, and J. Graybeal, Phys. Rev. B **37**, 7861 (1988).

[99] R. Auer, E. Brecht, and R. S. K. Herrmann, Physica C **299**, 177 (1998).

[100] J. Z. Wu and W. K. Chu, Phys. Rev. B **49**, 1381 (1994).

[101] J. F. Hamet, B. Mercy, M. Hervieu, and B. Raveau, Physica C **193**, 465 (1992).

[102] K. Higashiyama, I. Hirabayashi, and S. Tanaka, Jpn. J. Appl. Phys. **31**, 1835 (1992).

[103] J. D. Jorgensen, B. W. Veal, A. P. Paulikas, L. J. Nowicki, G. W. Crabtree, H. Claus, and W. K. Kwok, Phys. Rev. B **41**, 1863 (1990).

[104] Y. Ishizawa, Physica B **148**, 315 (1987).

LIST OF PUBLICATIONS

- A. El Tahan, G. Jakob, H. Adrian, and L. Miu. *Vortex-creep activation energy in $YBa_2Cu_3O_7/PrBa_2Cu_3O_7$ superlattices* Physica C **470** 1 (2010).
- L. Miu, D. Miu, T. Petrisor, A. El Tahan, G. Jakob, and H. Adrian. *Origin of the plateau in the temperature dependence of the normalized magnetization relaxation rate in disordered high temperature superconductors* Phys. Rev. B **78** 212508 (2008).
- A. El Tahan, G. Jakob, D. Miu, I. Ivan, P. Badica, and L. Miu. *Vortex-creep crossover in $YBa_2Cu_3O_7/PrBa_2Cu_3O_7$ superlattices during standard magnetization relaxation measurements* Supercond. Sci. Technol. **24** (2011) 045014
- A. El Tahan, P. Badica, and G. Jakob. *Evolution from a-axis to c-axis orientation in $YBa_2Cu_3O_7$ thin films on(001) $SrTiO_3$ grown by dc sputtering vs. grown temperature, post-annealing or two-temperatures template growth.* The Papers of Technical Meeting on Physical Sensors, IEE Japan, p. **55-61** (Tokyo, June 17-18, 2010, Technical Meeting on Sensors and Micromachines 2010)